A DISSERTATION
ON

SOLID IONIC CONDUCTOR FOR ADVANCED LITHIUM-ION BATTERY

Submitted in the Partial Fulfilment of the requirements for the Degree of
Master of Technology in Solid State Electronics and Materials

Submitted by

ANANT AGRAWAL
Enrolment No.-16550002

Under the Supervision of
Dr. YOGESH KUMAR SHARMA
Assistant Professor
Department of Physics
IIT Roorkee

DEPARTMENT OF PHYSICS
INDIAN INSTITUTE OF TECHNOLOGY
ROORKEE – 247667 (INDIA)

DECLARATION

I hereby declare that the project entitled **"SOLID IONIC CONDUCTOR FOR ADVANCED LI-ION BATTERY"** submitted by me to the Department of Physics, IIT Roorkee in partial fulfilment of the requirement for the award of the degree of **Master of Technology in Solid State Electronics and Materials** is a record of my own work carried out during the period June 2017 to May 2018 under the supervision of **Dr. Yogesh Kumar Sharma.**

Date:

Place: Roorkee

Anant Agrawal

M.Tech (SSEM)

IIT Roorkee

Certification

This is to certify that the above statement made by the candidate is correct to the best of my knowledge.

Date:

Place: Roorkee

Dr. Yogesh Kumar Sharma

Department of Physics

IIT Roorkee

ACKNOWLEDGEMENT

It is a matter of great pleasure to express my gratitude and veneration **to Dr. Yogesh Kumar Sharma** for his valuable supervision, convincing discussions, his constant inspiration throughout this work and for his valuable time he gave to me.

I would like to mention my gratitude the HOD of physics department **Prof. K.L Yadav** for his help and also for provided critical facilities available in his laboratory that were indispensible for completing my work. I would withal relish to thank all the edifiers in Department of Physics for their fortification.

I am grateful to **Mr. Asit Sahoo** (Research Scholar, Energy Storage Lab Department of Physics IIT Roorkee) for his constant support encouragement and offered many suggestions throughout this project work. I convey my heartfelt thanks to **Mr. Amit Kumar** and **Mr. Sandeep Sundriyal** (Research Scholar Energy Storage Lab Department of Applied Science Saharanpur Campus IIT Roorkee) for providing me characterization facilities like XRD, FESEM etc. I would like to say thanks **Mr. Brahma Prakash Dubey, Mr. Meetesh,** and **Mr. Atul Kumar** (Research Scholar Department of Physics, IIT Roorkee) for their persistent help and discussions they made with me. Without their supports I can't possibly able to complete my project work timely. I would like to express my thanks to my friends Sayantan Das, Monica and all my **labmates**.

I express my gratitude my parents for their grace love and affection and for giving me determination to overcome my problems.

Anant Agrawal

M.Tech (SSEM)

IIT Roorkee

ABSTRACT

Lithium ion batteries are the most promising energy storage system on the market today; however, safety issues associated with the use of flammable organic polymer-based electrolytes with poor electrochemical and chemical stabilities prevent this technology from using these storage devices in high end applications. In this regard, solid electrolyte is a key component for the practical application of rechargeable all-solid-state Li-ion batteries. Generally, solid electrolytes for all-solid state batteries should possess the properties such as high ionic conductivity and negligible electronic conductivity, wide voltage window of 5.5 V and chemical compatibility with the electrodes. Among all solid electrolyte materials ranging from sulphides to oxides and oxynitrides, cubic garnet–type $Li_7La_3Zr_2O_{12}$ (LLZO) ceramic electrolytes are superior candidates because of their high ionic Conductivity (10^{-3} to 10^{-4} S/cm) and good stability against Li metal. The goal of this M.Tech Dissertation is to develop the garnet structured ionic conductor and to generate fundamental understandings with the doping effect of the Fe and Al on frame of $Li_7La_3Zr_2O_{12}$ (LLZO) which has been successfully achieved through solid state (ceramic) method. Further, we have made an attempt to understand the structural properties and morphological studies, thermal and chemical stability as well as conductivity measurement of the synthesized samples.

Table of Contents

List of Figures

List of Tables

List of Abbreviations

EV	Electric Vehicle
HEV	Hybrid Electric Vehicle
LIB	Li-Ion Battery
LLZO	$Li_7La_3Zr_2O_{12}$
t-LLZO	Tetragonal LLZO
c-LLZO	Cubic LLZO
Fe-LLZO	$Li_{7-3x}Fe_xLa_3Zr_2O_{12}$
Fe:Al-LLZO	$Li_{7-3x-3y}Fe_xAl_yLa_3Zr_2O_{12}$
XRD	X-Ray Diffraction
RT	Room Temperature
TGA	Thermo gravimetric Analysis
DTA	Differential Thermal Analysis
DTG	Derivative Thermo-Gravimetric
FESEM	Field Emission Scanning Electron Microscope
EDX	Energy Dispersive X-Ray Spectroscopy
TEM	Transmission Electron Microscope
SAED	Selected Area Electron Diffraction
ICP-OES	Inductively Coupled Plasma-Optical Emission Spectrometry
VSM	Vibrational Sample Magnetometer
LCR	Inductance-Capacitance-Resistance
EIS	Electrochemical Impedance Spectroscopy

CHAPTER 1
INTRODUCTION

1.1 Need for Energy Storage:

In light of the rapidly increasing global energy needs, the associated CO_2 emission, and the global warming trend as a result efficient, clean, and sustainable energy sources are needed. Renewable energy such as solar and wind power are intermittent and are not consistently synchronized with the energy demand, which motivates the development of efficient energy storage devices. Batteries are the most versatile and economically viable devices, whose application can be from small electronic devices, to electric vehicles, and large scale energy storage.

1.2 Energy Storage Devices:

Energy storage devices play a crucial role in the field of engineering, research and development. Different type of electrical energy storage systems are classified in figure 1.1. Many of energy storage systems have its own advantages and limitations. Mechanical energy conversion system cannot be installed in small devices, but among these different energy storage systems, the Li-ion battery and supercapacitor are good option for energy storage. So battery energy storage has more energy density as compared to supercapacitor.

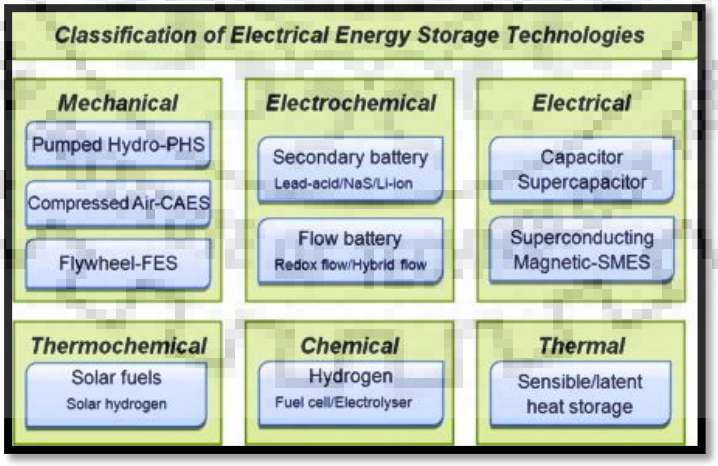

Figure 1.1 Classification of Electrical Energy Storage System[1]

Primary batteries are non-rechargeable because their electrochemical reaction is not reversible while in Secondary batteries are rechargeable, because their electrochemical reaction is reversible via applying certain voltage to the battery in the opposite direction of the discharge.

1.3 Li-ion Battery:

Li-ion battery is the dominant member of energy storage for different electronic devices such as portable devices; laptops, mobiles, equipment etc. first commercial Li-ion battery was developed in 1991 by Sony Japan. Latest technologies are attributed to advance safe Li-ion batteries along with fast charging as well as good storage capacity. The storage calibre of battery is defined by energy density ($Whkg^{-1}$or Whl^{-1}) and power density (Wkg^{-1} or Wl^{-1})[2]. The evaluation of energy storage capacities for different commercial batteries is shown in Figure 1.2. Both the weight and size decreases with increase in gravimetric and volumetric energy density, respectively. LIBs provide high working voltage (~ 3.6 V), and have longer charge retention (> 5 years) in spite of being light weight of battery.

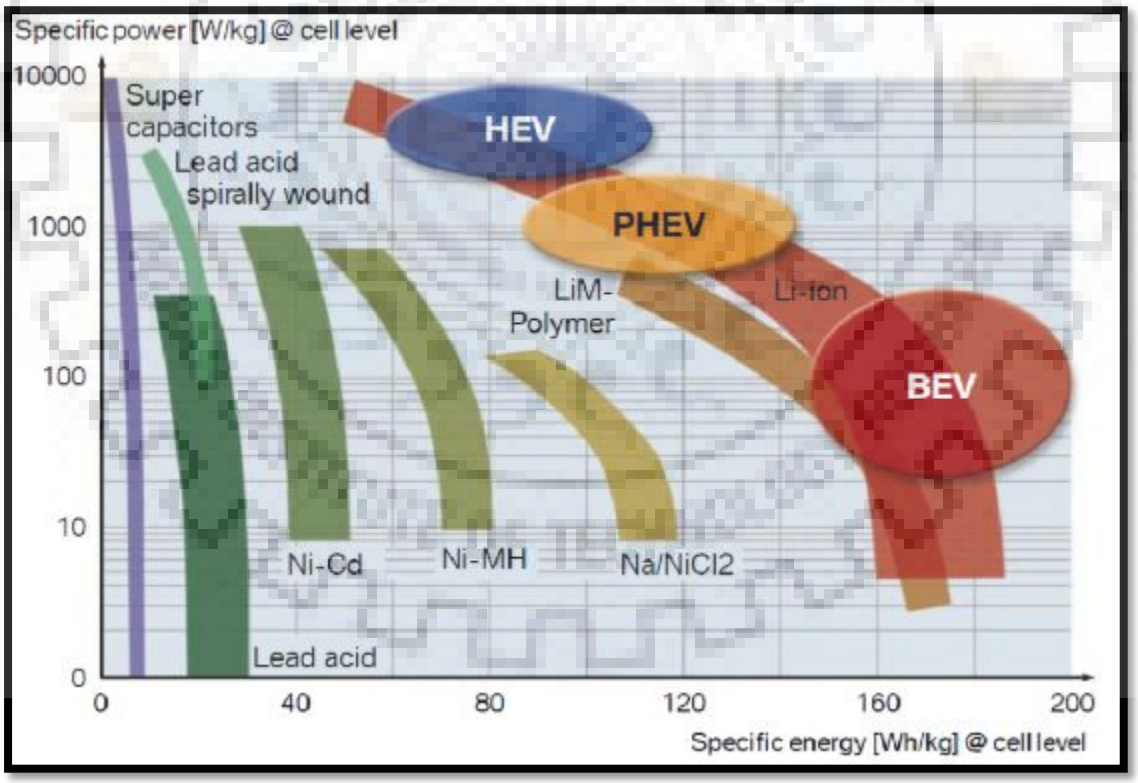

Figure 1.2 Specific energy density Vs. specific power density[3]

1.3.1 Basics of Li-ion Battery:

A battery is the energy storage device that converts the chemical energy into electrical energy through the electrochemical redox-reaction occurs on both the anode and cathode inside the battery. Actually, battery is a parallel combinations or series combination of cells to increase the current output or voltage output through the battery. So the smallest unit of battery storage is cell. The elementary components of battery cell are cathode, anode, and electrolyte and others constituents remain in the battery like separator, current collector etc. which maintain and enhance the device capacity.

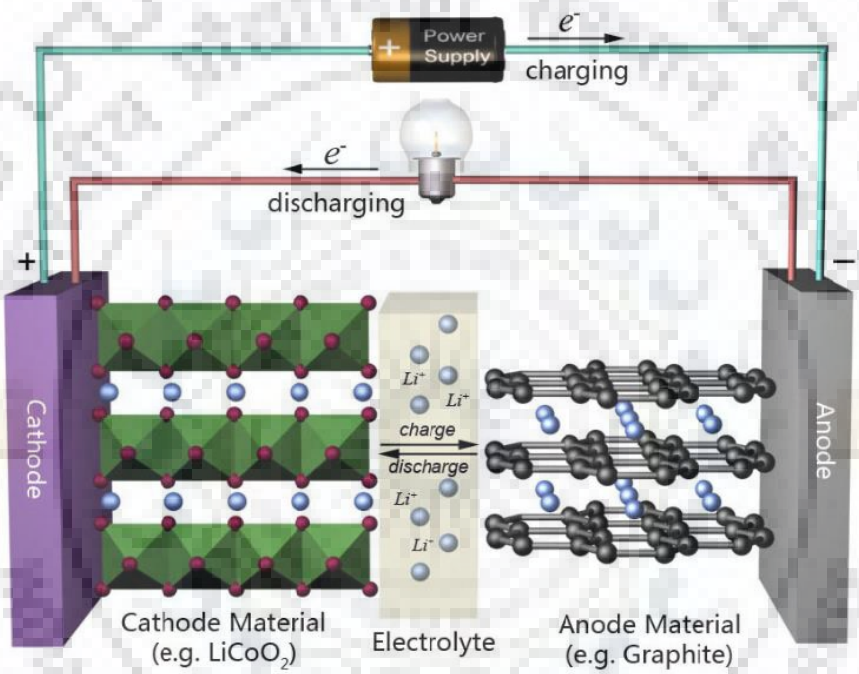

Figure 1.3 Working diagram of Li-ion battery[4]

The working principle of Li-ion battery is shown in Figure 1.3. During charging and discharging process, Li-ion shuttles back and forth through the electrolyte between the two electrodes named as cathode and anode. Hence, Li-ion battery technology are also known as ' rocking-chair' battery technology [9]. Generally, Li-ions intercalate (insert) or de-intercalate (extract) from the interstitial space in the atomic layers within the electrode components during charging-discharging process. The ideal electrolyte($LiPF_6$) would reveal high ionic conductivity (> 10^{-2} Scm^{-1} at room temperature). The ionic and electronic conductivities of electrolyte system govern the Li-ion transport and null electronic conduction furthermore other

factors like interfacial resistances and polarisation effects between the solid electrolyte interface(SEI) would be also accountable for conduction in Li ion battery.

During the charging process the Li-ions are released from the cathode(oxidation) and move to the anode(reduction) graphite negative electrode to create an intercalated Li_xC_6 (reduction). Electrons from cathode travel through the external circuit and reach at the anode side, and overall chemical reaction would be

Positive electrode : $LiCoO_2 \longrightarrow Li_{1-x}CoO_2 + xLi^+ + xe^-$

Negative electrode : $xLi^+ + xe^- + C_6 \longrightarrow Li_xC_6$

Overall (charging) : $LiCoO_2 + C_6 \longrightarrow Li_{1-x}CoO_2 + Li_xC_6$

During the discharging process Li ions starts de-intercalated through the anode and again move to cathode. And electricty is provided by the electrons which also travel through anode to cathode via external circuit. In reaction form it would be

Negative electrode : $Li_xC_6 \longrightarrow xLi^+ + xe^- + C_6$

Positive electrode : $Li_{1-x}CoO_2 + xLi^+ + xe^- \longrightarrow LiCoO_2$

Overall (discharging) : $Li_{1-x}CoO_2 + LixC_6 \longrightarrow LiCoO_2 + C_6$

Advantages of the present Li-ion battery technology

- **High voltage:** Li-ion batteries exhibit voltages up to 4 V.
- **High specific energy density and power density:** The energy output is two to four or more times better in lithium battery than that of zinc negative electrode batteries
- **Wide operation temperature range:** Most of the lithium batteries will operates over a temperature range from about 70 °C to -40 °C
- High Columbic and energy efficiency
- High rate and rapid charge capability
- Long cycle life and light weight compared to that of other rechargeable battery
- Better shelf life: Li-ion batteries can be stored for long periods, even at high temperatures, with no memory effect

Challenges associated with the present Li-ion battery technology

- Insufficient or moderate capacity at higher cycling rates.

- The power density is inadequate for the future applications.
- Self-discharging process and capacity loss after a certain time
- Due to the capacity loss, the cycling life is limited.
- Leakage problem due to liquid electrolyte which is used in Li ion battery.
- Due to dendrite formation caused explosion and it might be risky.

Table 1.1: Material Information about Li-ion Battery

Cathode material	**Electrolyte system**	**Anode material**
$LiCoO_2$ (Specific energy (capacity)150-200Wh/kg. Specialty cells provide up to 240Wh/kg $LiFePO_4$, LMS	**Liquid electrolytes:** salt based; $LiPF_6$ $LiClO_4$, $LiAsF_6$, $LiPF_6$, $LiSO_3CF_3$, and $LiN(SO_2CF_3)_2$ dissolved in propylene carbonate (PC), diethyl carbonate (DEC), ethylene carbonate (EC), dimethyl carbonate (DMC), or ethyl methyl carbonate (EMC). These solvents have optimized electrochemical Stability over highly oxidation reduction phenomena at the electrodes. Shows the ionic conductivity of order 10^{-2}S/cm	LiC_6 Graphite And Li metallic anode is also used as anode
	Solid electrolytes: LLZO and others LGPS, LLTO, LiPON, NASICON, LISICON are used due to good ionic conductivity of order 10^{-3}S/cm **Polymer electrolytes** based on PEO	

1.4 Electrolyte System:

Electrolyte is the key component of Li-ion battery. Electrolyte plays an important role in Li-ion battery as chemical medium between cathode and anode inside the Li-ion battery during the charging and discharging process. Since the Li-ion conduction through electrolyte depends on many things like Li-ion concentration of electrolyte, types of electrolyte e.g. liquid electrolyte, solid electrolyte etc.

Electrolyte can be classified in three categories

- Liquid Electrolyte
- Polymer Electrolyte
- Inorganic Solid Electrolyte

1.4.1 Liquid Electrolyte:

Liquid electrolyte possesses the good ionic conductivity 10^{-2} S/cm. It is used at commercial level due to some expedient features like fast ionic conductor, low interfacial resistance between electrode electrolyte surface, low weight but some issues with liquid electrolyte remain always associated like safety concern, thermal stability at high temperature, leakage problem, dendrite formation which caused the short circuit of electrodes etc. some common electrolytes are tabulated.

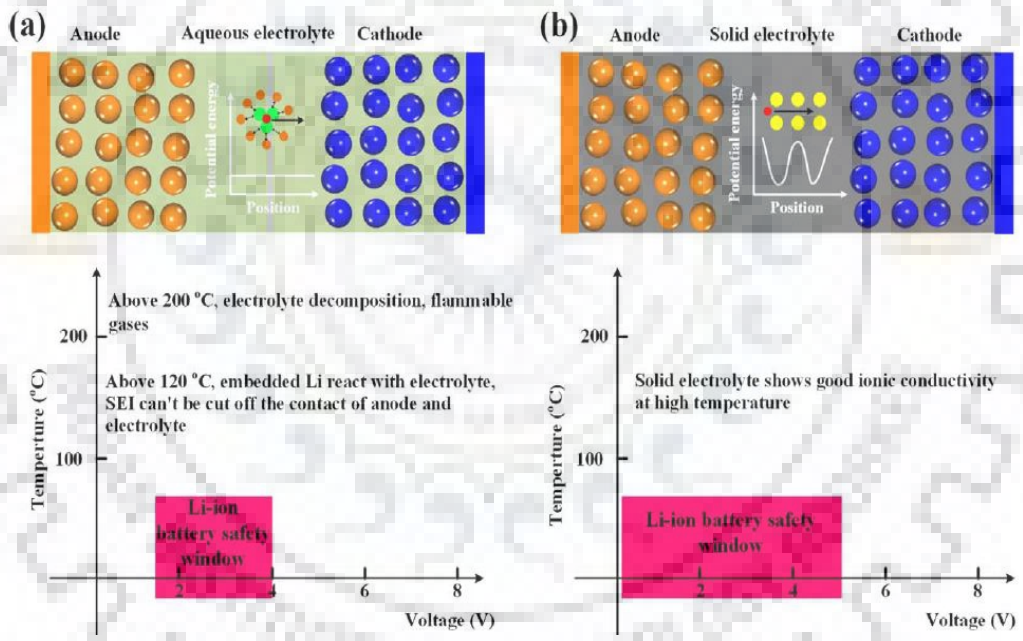

Figure 1.4 Comparison of aqueous and solid electrolyte[5]

1.4.2 Solid Polymer Electrolyte:

Solid polymer based electrolyte is also attractive candidate for thin film Li-ion batteries. The polyethylene oxide based electrolyte was investigated by Wright et al in 1973, and this technology has been useful for the application part of thin film Li-ion batteries by armed et al.[6]

The high ionic conductivity $\simeq 10^{-4}\,S/cm$ is observed at temperature 60-80^{o} C and phase is also being changed crystalline to amorphous. To remove this drawback several efforts has

been done. Add liquid plasticizer but problem is also associated with this patent such as deterioration of mechanical stability and risk of reaction is also sustained which may happen with lithium metal oxide at anode. Croce et al discovered in 1998 that Nanostructure based ceramic material such as TiO_2 & Al_2O_3 could be added with solid plasticizers applicable on lower temperature operation and ionic conductivity was recorded of order 10^{-5} at room temperature which was three times more than from plasticizers free PEO.[6]

Solid polymer based electrolyte can be used as conductor and as well as separator in Li-ion batteries, but problematic issue is poor conductivity of order 10^{-8}. Many efforts was came to bringing to light to improve the conductivity in which one was adding the polymer matrix consisted of ceramic filter such as SiO_2 , TiO_2 etc.

1.4.3 Solid Electrolyte:

Solid electrolyte used as ionic conductor for Li ion battery, and these solid electrolytes contain Li ions and kinetics of Li ions in solid conductor is different from liquid electrolyte. The advantages of solid electrolytes over liquid electrolytes are their wide electrochemical window (up to about 6V/Li), high chemical and physical stability, and long shelf life. The prerequisites are shown here below

- High thermal stability at high temperature (up to 800^oC) so that device can be used at in high temperature atmospheres.
- Possesses total lithium ion conductivity of order 10^{-4} Scm^-1-10^{-3} Scm^{-1} at operating temperatures.
- Negligible electronic conductivity i.e. electronic insulator
- High chemical stability with Li electrodes during the long-term operation
- Thermal expansion coefficient match with Li electrodes
- High electrochemical decomposition voltage (up to 5.5V vs. Li)
- Low cost, easy transportation and environmental benignity

The solid electrolytes would be classified into two categories, namely Amorphous and crystalline electrolytes.[7]

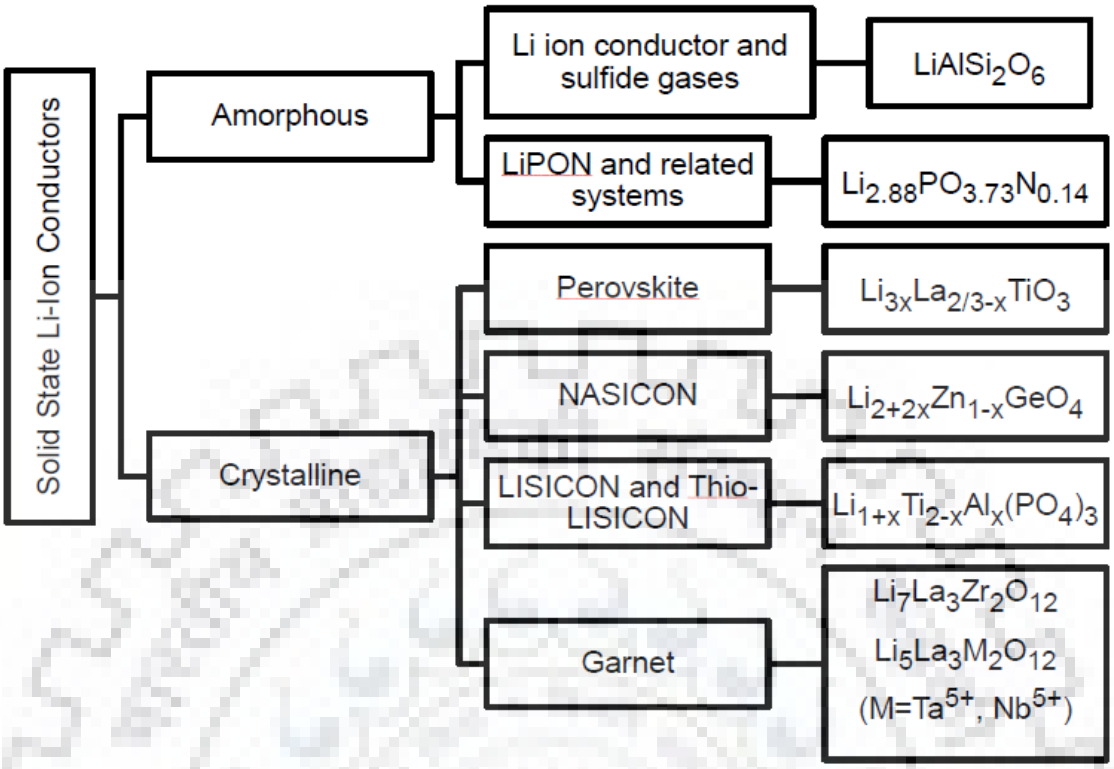

Table 1.2: Comparison of the key aspects of solid state electrolytes with regard to their application in Li-S and Li-O_2 cells.

Electrolyte	Stability with Metallic lithium	Stability to Li Dendrite growth	Stability With O_2	σ (S/cm) $>10^{-4}$
Li-ion Sulphide Glasses	Yes	N/A	No	Yes
LiPON	Yes	Yes	Yes	No
NaSICON	No	Yes	Yes	Yes
LiSICON	Yes	N/A	Yes	No
Perovskite	No	Yes	Yes	Yes
Garnet	Yes	yes	Yes	Yes

N/A not available

1.4.3.1 Amorphous Li-Ion Conductor:

1.4.3.2 Sulphide Glass:

Earliest reported solid conductor for Li-ion battery was sulphide glassy (1980 by levasseur et al [23]). The nominal formula of sulphide glassy conductor is given by B_2S_3-Li_2S-LiY (Y=F, Cl, Br, I) and halogen elements also affect the conductivity of it's due to polarisibility. Maximum conductivity of order 10^{-3}S/cm was achieved in sulphide glasses. Sulphide glasses exhibit hygroscopic tendencies and reacting behaviour was also observed with O_2..

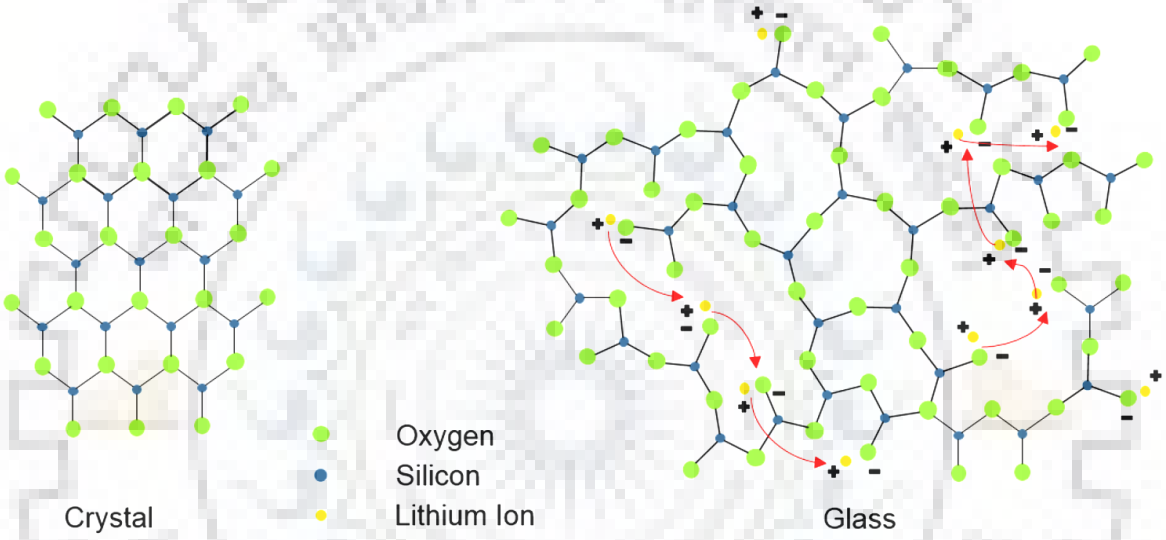

Figure 1.5 Crystal structure of glassy sulphide solid

Hopping of Li-ion in glassy material is much more due to its free volume available in it as compared to crystal structure.

1.4.3.3 LiPON:

Amorphous Li-ion conductor does not have a crystalline structure. The electrochemical window of LIPON is 5.5 V±0.2V vs. Li/Li-ion (between 0V and 5.5V) and conductivity is 2.3×10^{-6} [21] and also activation energy shows order of 0.55±0.2eV. The advantage of Amorphous conductor reveals excellent cyclability (>10,000 cycles).

1.5 Crystalline Electrolytes

1.5.1 Perovskite-type Li-ion Conductors:

The perovskite type Li-ion conductor belongs to the ABO3 structure. Where A is the 12 co-ordinated cations and B is the 6-fold coordinated. Prominent formula of perovskite Li ion conductor is $Li_5La_3Ti_2O_3$ (LLTO). This is presented in the figure 1.6(b). Li-ion resides in the voids of the structure.

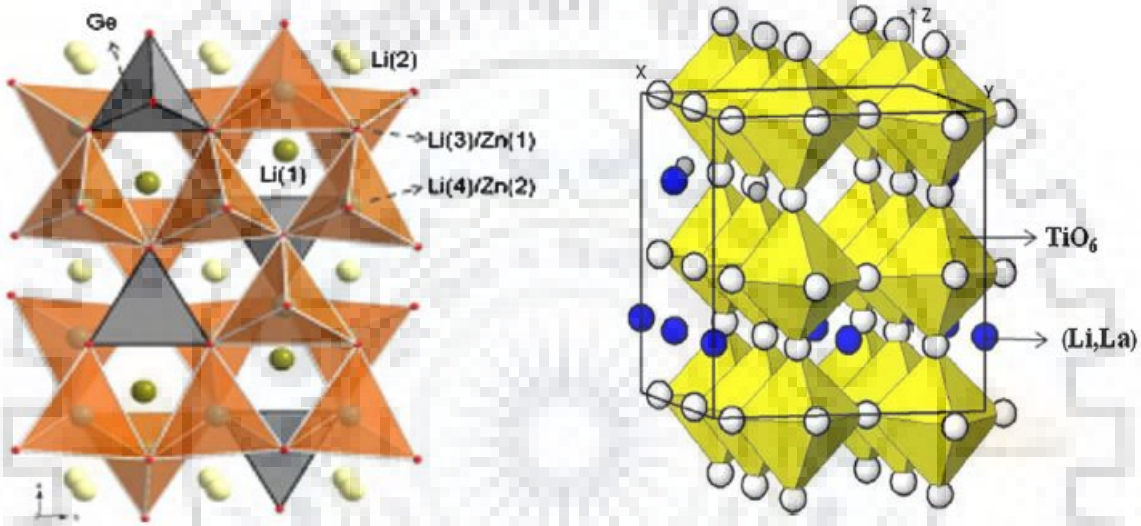

Figure 1.6 Crystal structure of Perovskite type ionic conductor[5]

BO_6 octahedra is enclosed by 12 coordinated A-site ions. Perovskite structure is stable at high temperature. Prior LLTO has been virtuous candidate among the other solid ionic conductors due to its good bulk Li-ion conductivity up to order of 10^{-3}S/cm. Later on the many work carried out on perovskite family of Li-ion conductor, and attained Li-ion conductivity of the LLTO is 7×10^{-5}S/cm. and the reason of high conductivity of this family is rational vacancy available for conduction of Li-ions so activation energy becomes low, but main delinquent factors of this perovskite family observed as in battery applications was reducibility of Ti+4 in direct contact with metallic lithium. So, further this product is not viable for battery application.

1.5.2 NASICON-type Li-ion Conductors:

Na super ionic conductor (NASICON) is phosphate type conductor which belongs to rhombohedral structure (R_3C) with general formula A_xB_2 $(PO_4)_3$, where A belongs to monovalent ion and B belongs to multivalent state (up to pentavalent). $A_2P_3O_{12}$ can also show the NASICON. AO_6 resembles to octahedral and PO_4 resembles to tetrahedral, which is three dimensionally (3D) linked to form two interstitial sites (M1 and M2) which make the conduction pathways. The bottleneck provides the path to the Na-ions as for transportability, and this framework of NASICON is applicable to the Li ion conductors. Only ions, which reside in the voids, could be altered so Li-ion fits into the frame of NASICON.

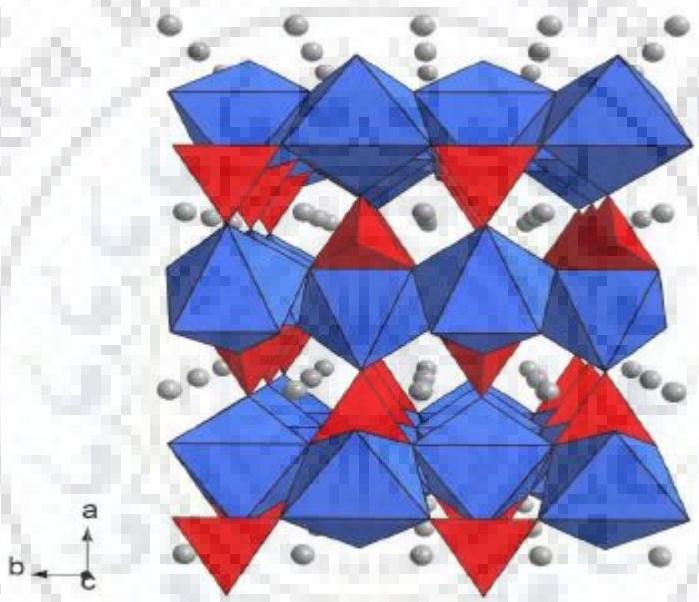

Fig1.7 Crystal structure of NASICON. The red octahedra, grey tetrahedra and blue spheres represent AO6, PO4, and lithium, respectively.[8]

The NASICON type Li-ion conductors belong to the family of $LiMe_2^{IV}$ $(PO_4)_3$ (M^{IV} = Ge, Ti and Zr). This family of electrolytes, Ti comprising $LiTi(PO_4)_3$ has been found to possess the maximum conductivity due the ionic radius of Ti^{4+} [33]. It has also been shown that trivalent substitution for Ti^{4+}, as in $Li_{1+x}Ti_{2-x}M_x^{III}(PO_4)_3$ (M=Al, Cr, Ga, Fe, Sc, In, or La), results in increased conductivity. For example, Al doping results in a bulk conductivity of 3×10^{-3} S/cm at room temperature [34]. However, Ti^{4+} is reduced when in contact with lithium (2.5 V vs. Li/Li^+) to form a mixed conductor.

1.5.3 LISICON type Li-Ion Conductor:

This is the Li super ionic conductor (LISICON). The candidate of this family was $Li_{1.4}ZnGeO_4$ and the general formula of this candidate was given $Li_{2+2x}Zn_{1-x}GeO_4$ ($-0.34<x<0.87$). This candidate belongs to the space group Pnma orthorhombic [6-7, 8-10]. The structure is shown in figure 1.8. The LISICON structure is made of cation that have occupancy half of the tetrahedral site with hcp oxygen ion array. The Li-ion diffusion is followed from tetrahedral to interstitial octahedral sites [11-12]. The role Li-ion distribution is also important in point of view Li-ion conduction phenomena throughout the electrolyte which affects the conductivity [32]. The conductivity of $Li_3.5Zno_{.25}GeO_4$ was observed of order 10^{-7}S/cm.

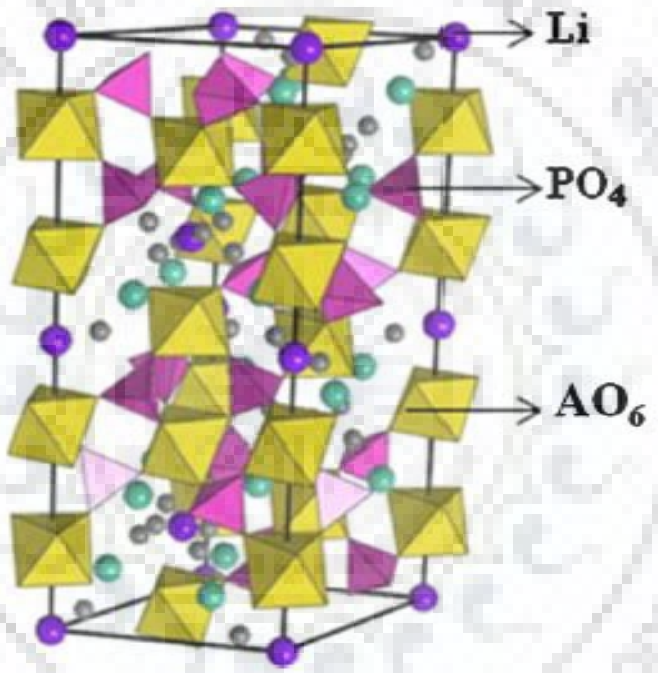

Figure 1.8 LISICON cystal arrangement.

Due to low conductivity, reseacher established thio-LISICON(Li conducting sulphide compounds) family.The formula is given by $Li_{4-x}M1\text{-}yNyS_4$ where (M=Si,Ge) and (N=P,Al,Zn,Ga). The fast ionic conductor of thio-LISICON family $LiGe_{0.25}P_{0.75}S_4$ has been developed with high ionic conductivity of order 10^{-3}S/cm.but, this candidate LGPS have many issues stability with Li metal and others.

Table 1.3: Critical issues are associated with solid electrolytes system[9]

Currently used solid Li electrolyte material	Structure	Problems encountering for the Li ion battery application
Li_3N	2D (layered)	Poor electrochemical stability at room temperature (0.445 V)
$Li_{1.4}ZnGe_4O_{16}$ (LISICON)	3D	Reactive towards Li metal and atmospheric CO_2, and conductivity decreases with time
$Li_{1.3}Ti_{1.7}Al_{0.3}(PO_4)_3$ (NASICON)	3D	Unstable with Li metal
$(Li,La,\square)TiO_3$	3D	Unstable with Li metal, difficult to control the lithium content, and large grain boundary resistance
$Li_{2.88}PO_{3.86}N_{0.14}$ (LiPON)	3D	Moderate conductivity, which varies with sputtering conditions.

1.5.4 Garnet Solid Electrolyte:

Different types of solid electrolytes were reported for Li-ion battery as solid conductor. In which some oxide conductors was superior due to its ease of synthesis, thermal properties, and others like mechanical properties etc. Most of the inorganic oxides Li-ion conductor had merits and demerits such like some oxide material revealed either high ionic conductivity or high electrochemical stability but both properties was difficult to shown at a one time and due to this limitations like electrochemical stability and other low ionic conductivity etc. Then some researches experienced the lack of criteria which had to be fulfilled by in prior solid electrolyte. So, there was done strong research on such type's material solid ionic conductor for Li-ion battery in which the one was $LiLaTiO_3$ (LLTO). But, attempt was remained unsuccessful due to formation of pyrochlore during the synthesis of LLTO. The first novel solid electrolyte contained Li and oxide metals were reported by Prof. Werner wepnner's Laboratory.

The garnets possess a general chemical formula of $A_3B_2(XO_4)_3$ (A= Mg,Ca Y, La or rare earth metals and B = Al, Fe, Ga, Ge, or V; X = Si, Ge, Al) where A, B and X are 8-, 6- and 4-fold coordinated cation sites. Garnet belongs to space group Ia-3d. In garnet-type in general types solid electrolytes, $Li_3Ln_3M_2O_{12}$ (Ln = lanthanides; M = Te, W), $Li_5La_3M_2O_{12}$ (M = Nb, Ta, Sb), $Li_6ALa_2M_2O_{12}$ (A = Ca, Sr, Ba, Mg; M = Zr, Sn, Ta, Nb), and $Li_7La_3M_2O_{12}$ (M = Zr, Sn) has been studied in detailed. Among them, the first reported Li-stuffed garnet electrolyte was $Li_5La_3M_2O_{12}$. Figure 1.9 represents the crystal structure of $Li_5La_3M_2O_{12}$. In $Li_5La_3M_2O_{12}$, Li-ions are distributed at both tetrahedral (24d) and distorted. octahedral (48g/96h) sites, which had been confirmed by Cussen et al. using NPD method.$Li_7La_3Zr_2O_{12}$ remains in two phases: high-temperature (more than $1000^{O}C$) cubic phase (space group Ia-3d)

and low-temperature tetragonal phase (900^{o}C) belongs to space group I41/acd). The cubic-LLZO (c-LLZO) exhibited higher ionic conductivity than tetragonal-LLZO (t-LLZO). In c-LLZO, there are three occupied sites is found for Li-ions, tetrahedral sites(24d),octahedral sites (48g), and off-centered octahedral sites (96h), respectively.

Li-ion sub lattice remain in ordered manner (all Li sites either full or empty occupied) in t-LLZO, while the Li sub lattice remain in disordered state (all Li sites partially occupied or empty) in c-LLZO. The 3D framework c-LLZO is comprises of face-shared tetrahedral and octahedral.

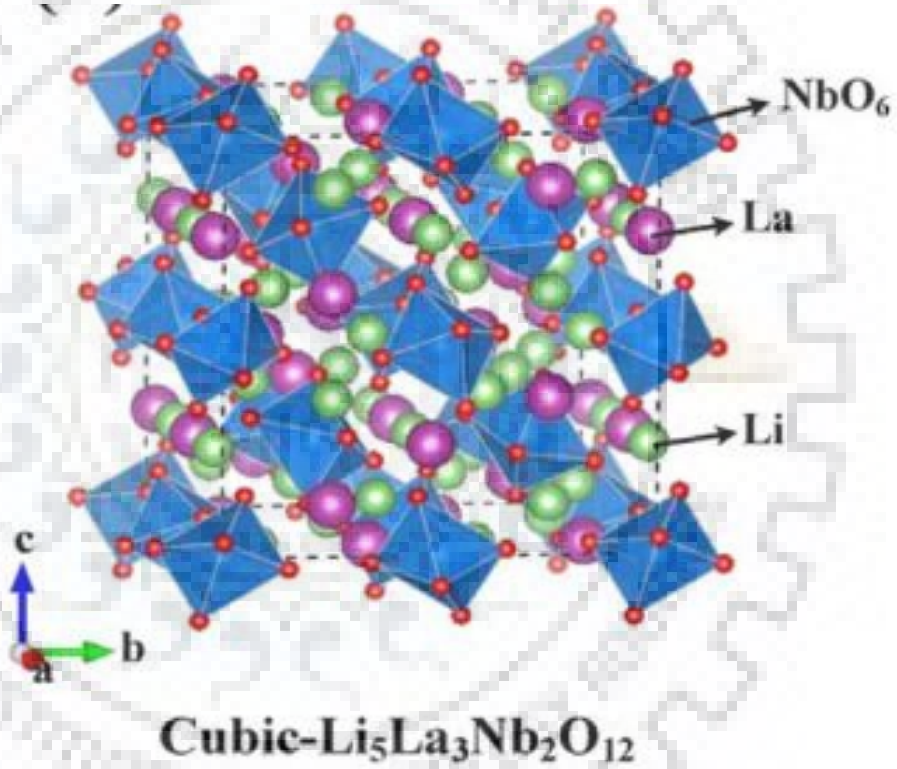

Figure 1.9 $Li_5La_3Nb_2O_{12}$ garnet cubic crystal structure.

For better understanding of both phases of LLZO t-LLZO and c-LLZO there are some chief information can be described as

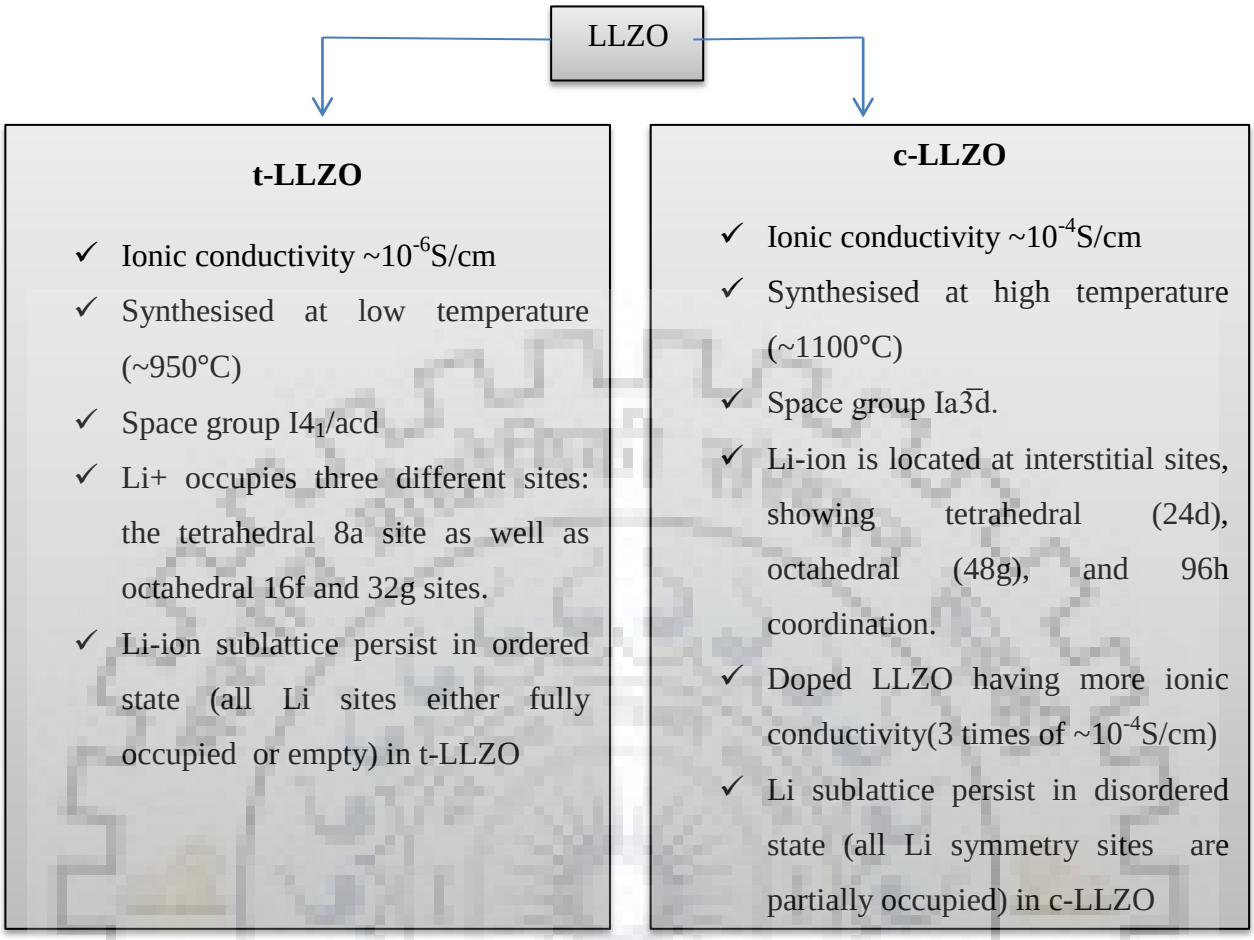

In figure 1.10, 2D diagram are shown for explaining both phase t-LLZO and c-LLZO. In t-LLZO all Li sites are occupied while in c-LLZO all Li sites partially filled. The active movable Li-ions are more in c-LLZO as comparison to t-LLZO. Here in this figure 1.10 the c-LLZO picture (simulated NPD image) is shown without doping so here is less vacant space for conduction of Li-ions. When c-LLZO synthesised by doping method supposed to doing element is Fe^{+++} then one Fe^{+++} will replace three Li-ion according to charge neutrality. So, there will be more vacant space for hoping of Li-ion during the diffusion and conduction process and this situation indicates more ionic conductivity than t-LLZO.

The cubic phase LLZO have high ionic conductivity ($\approx 10^{-4}$ S/cm) in comparison to tetragonal ($\approx 10^{-6}$ S/cm) because of cubic LLZO belongs to space group Ia-3d in which Li distributed in disordered state i.e. all the Li sites with the same symmetry are only the partially occupied, however the space group of tetragonal LLZO is $I4_1/acd$. In which Li distributed in ordered state i.e. all the Li sites with same symmetry are either fully occupied or completely.

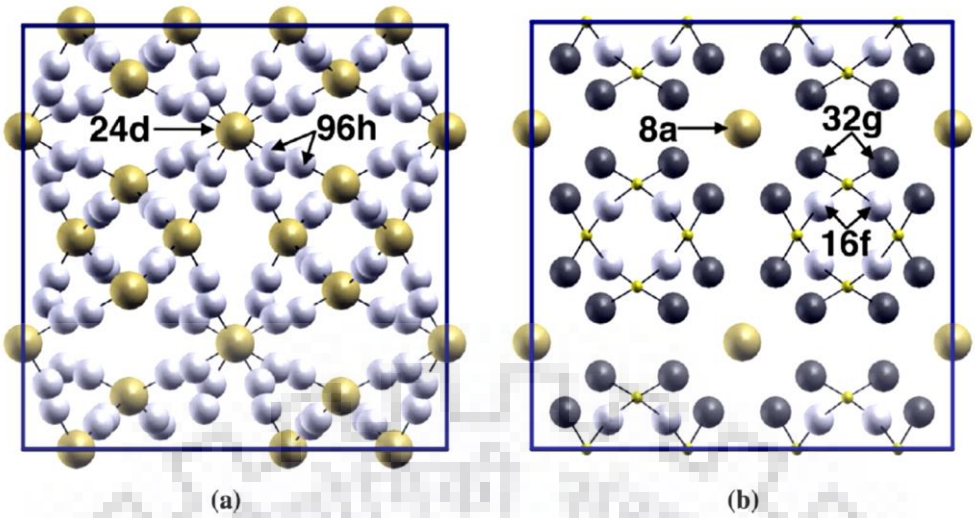

Figure 1.10 Interstitial sites inside c-LLZO and t-LLZO respectively [10]

The LGPS possesses highest ion conductivity but regarding safety and stability concern LLZO is the best option in present era.

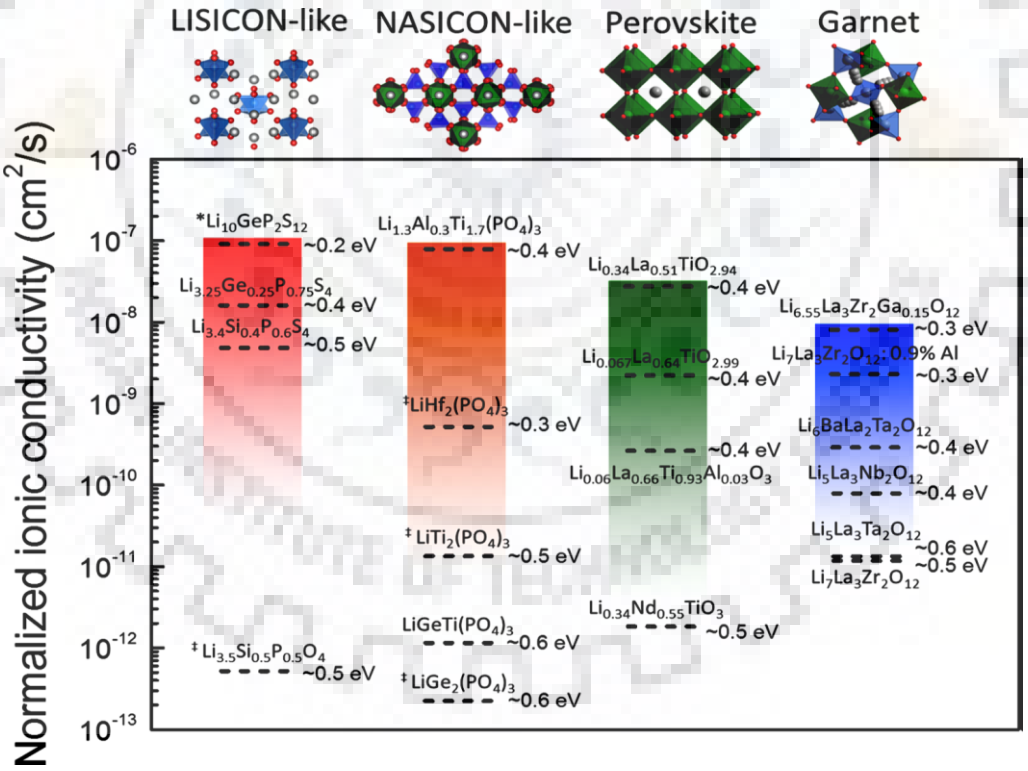

Figure 1.11 Comparison of different solid ionic conductors.

1.6 Effects of Doping:

The garnet $Li_7La_3Zr_2O_{12}$ (LLZO) exists in two polymorph of tetragonal structure which having space group I41/acd (no. =142) and cubic structure with space group Ia-3d (No. =230).

In the structure of LLZO one unit cell $Li_{56}La_{24}Zr_{16}O_{96}$ containing 8 formula units $Li_7La_3Zr_2O_{12}$. Zr and La are situated in the centre of ZrO_6 and LaO_8 respectively (elaborated for cubic phase in fig1.11) the peculiar properties of t-LLZO and c-LLZO are associated by occupancy of Li sites. Li sites are partially occupied in case of cubic structure, while fully occupied in case of t-LLZO. t-LLZO phase only can be synthesised without doping through solid state routes and combustion method etc.

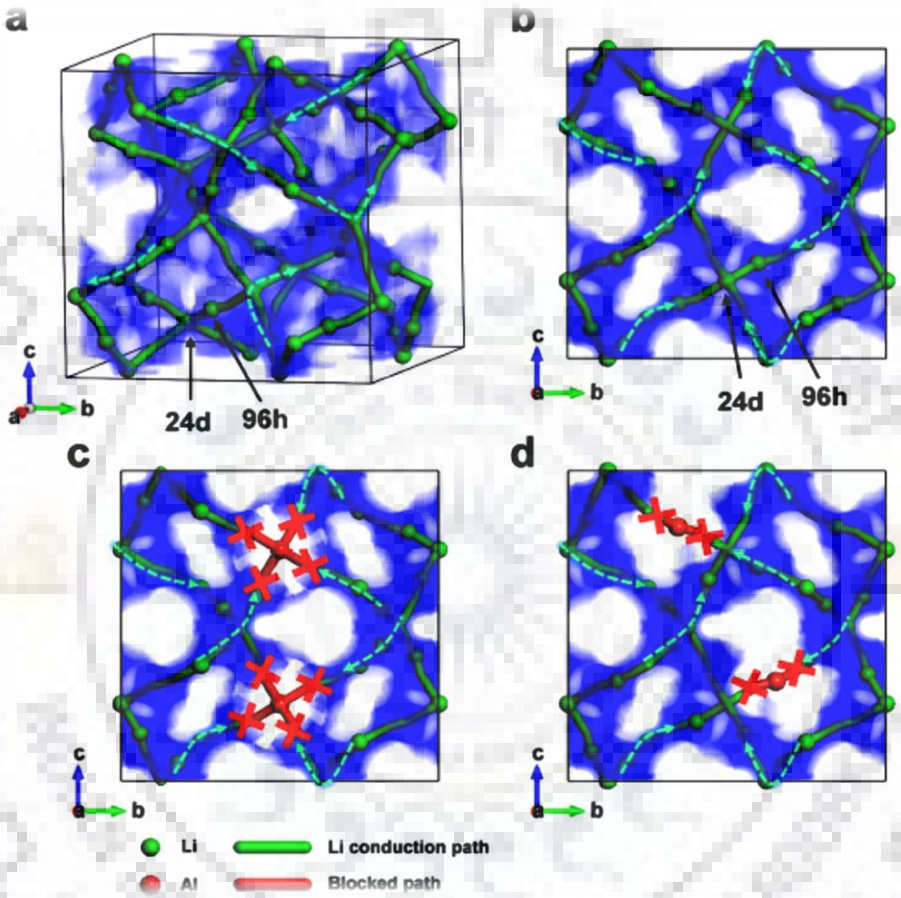

Figure 1.12: The blocking effect of dopant(e.g. Al) in cubic LLZO structure.[11] **(a) 3D illustration of un-doped cubic LLZO. Projected view from along the [100] direction of (b) un-doped cubic LLZO, (c) Al-doped LLZO with Al in 24 d site, (d) Al-doped LLZO with Al in 96 h site. The blocked path by Al is marked as red "X" in (c) and (d). The green arrows are depicted to represent diffusive motion of Li. A certain region (0.5 < a < 1.0) is selected exclusively in (b), (c) and (d), to avoid overlapped data.**

because all Li sites are already occupied so there is no need of doping in case of t-LLZO[11]. Without doping element the tetragonal phase was prepared in agreement of previous reported [34-38].So tetragonal phase can be synthesised at low temperature range (600C-950C) which is reported in so research publications.

1.7 Diffusion of Li-ion in the LLZO

The general structural formula of Garnet is $A_xB_3C_2O_{12}$, where $x \geq 3$ and A, B, C are 8 coordinated, 4 coordinated and 6 coordinated cation sites respectively. LLZO have two different phase structure on the basis of synthesis, one is tetragonal phase structure is synthesized at lower temperature around 900^{o}C and second is cubic phase structure which is synthesized at corresponding higher temp, nearly 1120^{o}C.

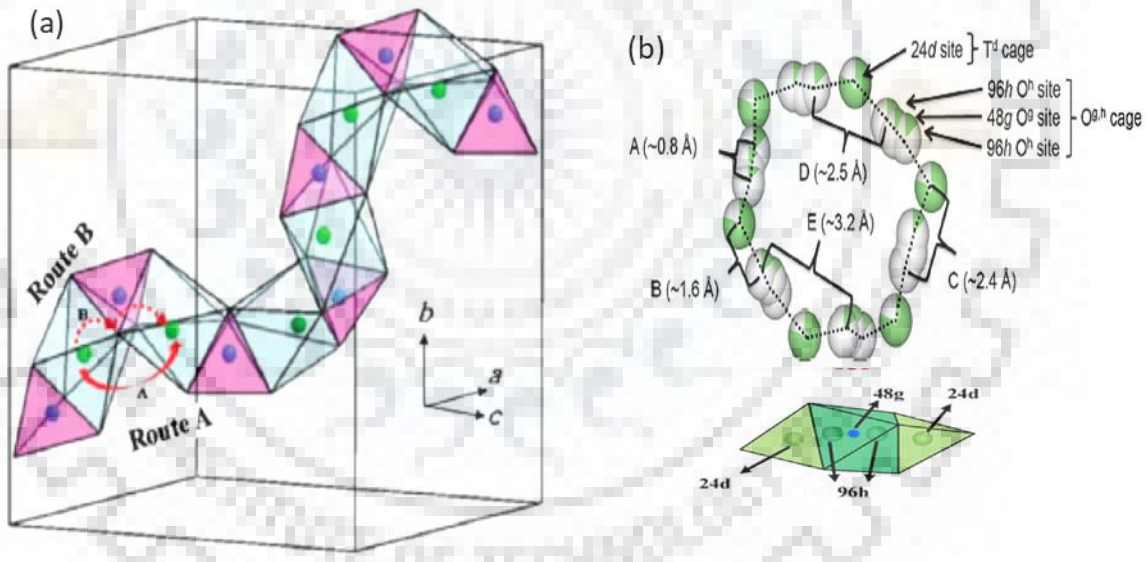

Figure 1.13 Hopping mechanics of Li through Li sites[5]

Li-ion transport mechanism in garnet-type conductors was studied by experimental and theoretical methods. Cussen et al[5]. observed Li…Li dimers with short distance of 2.44 Å in LBLTO by NPD method. The high displacement parameters of Li-ions at 24d sites and the short distances suggested a complex cooperative mechanism in LBLTO. For migration pathway, two potential pathways are proposed by Baral et al. [5], as shown in Fig. 1.13. In

route A, Li-ions migrate between two octahedral Li sites via interstice by passing their common tetrahedral neighbour, i.e., the tetrahedral Li sites do not participate in the migration process. In route B, Li-ions move through shared triangular faces that separate the octahedral and tetrahedral polyhedral, i.e., Li ions at tetrahedral sites participate in the migration process. The route A was suggested by Li NMR studies. A Li-ion migration path of 24d-96h-48g-96h-24d and found Li-ion migration at 24d sites is the rate-determining step (Fig. 1.13). Li-ion 3D diffusion pathway consisting of interlocking Li(24d)- Li(96h)-Li(48g)-Li(96h)-Li(24d) chain segments. Using DFT calculations, Xu et al. [5] found that Li-ion migration through tetrahedral sites had lower energy barrier, suggesting tetrahedral sites participated in the diffusion process. High bulk conductivity was attributed to the cooperative diffusion of Li-ions at adjacent tetrahedral and octahedral sites, in which the cooperative diffusion occurs under two conditions: (i) Li arrangement with the 48g/ 96h-24d-48g/96d, (ii) unstable residence of Li-ion at the 24d.

One another thing is noted that the accommodation of Li-ions in the lattice is closely depends on the Li-ion concentration and it is correspond to conductivity as well. There are two possible sites of accommodation of Li-ion –tetrahedral 24d (Li1) which is 56% occupied and octahedral 48g (Li2) which is 88% occupied. In standard $A_3B_3C_2O_{12}$ garnet, the $B_3C_2O_{12}$ framework contains 3D connected tetrahedral interstitial space (24d) that are bridges by empty face sharing octahedral sites (48g). For $Li_xB_3C_2O_{12}$ compound with $x>3$, the tetrahedral 24d sites are not sufficient enough for accommodation of all Li-ion cation so extra Li-ion cation must enter the octahedral sites that are fully empty for the standard garnet structure ($x=3$).

Overall path of Li ion conduction in the LLZO lattice cell is not necessary straight forward as shown in the figure 1.13.

CHAPTER 2

EXPERIMENTAL TECHNIQUES

2.1 X-Ray Diffraction:

X-ray diffraction is a technique by which we investigate the fine structure of material. This technique begun from von Laue's discovery in 1912 that crystal diffracts x-rays, the manner of the diffraction revealing the structure of the crystal. At first, x-ray diffraction was done only for the determination of crystal structure. Later on, however, other applications of x rays were developed, and today the method is applied, not only to structure determination, but to such diverse problems as chemical analysis and stress measurement, to the study of phase equilibriums and the measurement of particle size, to the determination of the orientation of one crystal or the ensemble of orientations in a polycrystalline aggregate.[12]

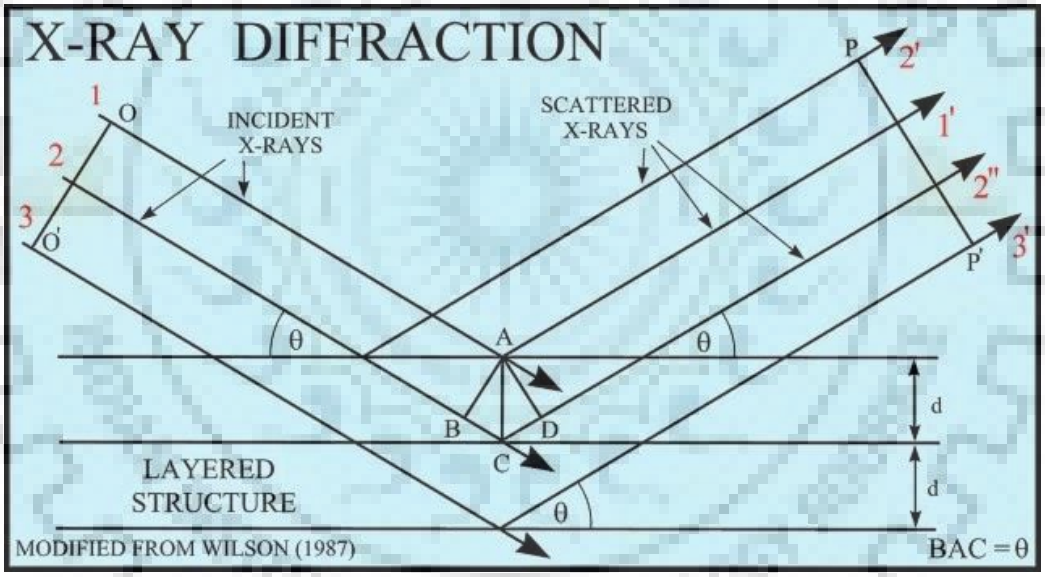

Figure 2.1 Schematic diagram of X-ray diffraction

When an atomic electron is irradiated by a beam of monochromatic x-rays, it starts vibrating with a frequency equal to that of incident beam. Since an accelerating charge emits radiation, the vibrating electrons present inside a crystal become source of secondary radiations having the same frequency as the incident x-rays. The secondary x-rays spread out in all possible directions. The phenomenon may also be regarded as scattering of x-rays by atomic electrons. If the wavelength of incident radiations is quite large compared with atomic dimensions, all the radiations emitted by electron shall be in phase with one another. The

incident x-rays, however, the same order of wavelength as that of atomic dimensions; hence the radiations emitted by electron are, in general, out of phase with one another. These radiations may, therefore, undergo constructive or destructive interference producing maxima or minima in certain direction. Schematic diagram of x-ray diffraction is shown in the figure 2.1.

Diffraction in general occurs only when the wavelength of the wave motion is of the same order of magnitude as the repeat distance between scattering centres. This requirement follows from the Bragg law.

$$\lambda = 2d \sin \theta$$

Experimentally, the Bragg law would be applied in two ways. The first one is if the wavelength of x-ray and measuring θ are known. Then d spacing can be calculated. Second one method is used to finding out the wavelength of x-ray by using known d spacing and θ.

Unknown structure analysis can be done in two ways.

1. Write the (hkl) corresponds to every peak arises in the XRD pattern named as "indexing the pattern". This technique confirms the structure of sample like bcc,sc or fcc and lattice parameter etc. further for the sample identification we match the XRD pattern with JCPDS card no. so this analysis confirms the chemical formula of sample.
2. The number of atoms per unit cell can be computed by shape and size of unit cell.
3. Position of atoms in the crystal structure would be analysed by relative intensity of diffraction lines.

2.2 Thermal Analysis:

2.2.1 Differential Scanning Calorimetry (DSC)

Differential scanning calorimetry (DSC) is a technique to investigate the various factors under the thermal conditions.

A DSC analyser measures the energy changes that occur as a sample is placed in the heating, cooling or isothermal atmosphere, together with the temperature at which these changes occur. The energy changes gives the many information shown below and in the figure 2.2 quantitatively.

Quantities measured by DSC are:-

1. Specific heat

2. Heat flow

3. Enthalpy

As well as phenomena, namely:-

1. Melting

2. The glass transition

3. Reactions

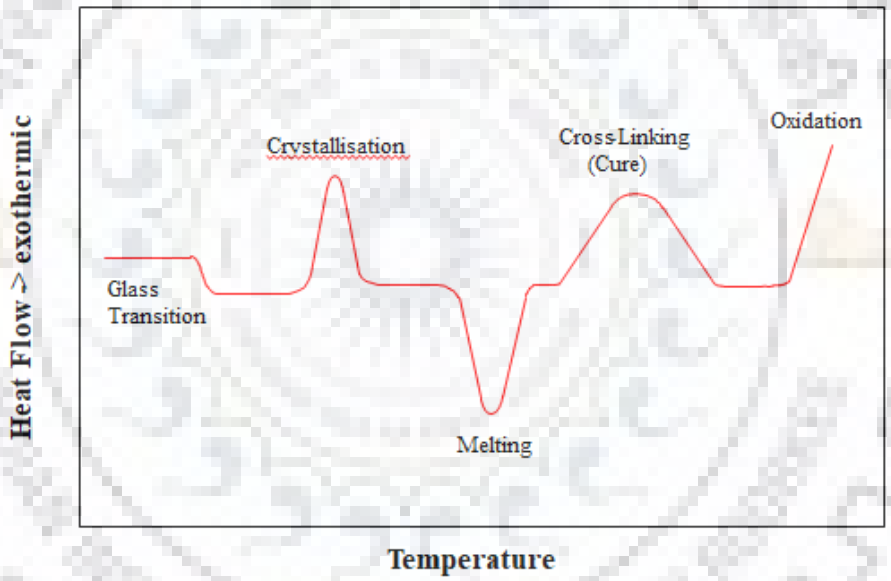

Figure 2.2 DSC curve heat flow vs. Temperature

2.2.2 Thermo Gravimetric Analysis (TGA)

Thermo-gravimetric Analysis (TGA) is a technique in which we measure the mass of a substance as a function of temperature with respect to time. In other words, we monitor mass loss/gain vs. temperature. When the sample specimen is subjected to a controlled temperature program in a controlled atmosphere. Thermo Gravimetric Analysis (TGA) evaluates the weight/mass change (loss or gain) and the rate of mass change with the temperature, time as well as atmosphere. In this measurement we determine the elemental composition of materials with respect of their thermal stability. By this technique one can characterize materials that

exhibit weight loss or gain because of sorption/desorption of volatiles, oxidation/reduction and decomposition. There is sample pan which is supported by a precision balance in TGA system which resides in a furnace and is cooled or heated during the analysis. The mass of the sample is simultaneously monitored. A sample purge gas controls the sample environment. This gas may be reactive or inert that flows over the sample and exits through an exhaust.

From the TGA analysis we can investigate the following factors.

- Thermal Stability of substance at high temperature and check the decompositions if any occurs at high temperature.
- Oxidative Stability of Materials
- Composition of Multi-component Systems as well as Lifetime of a Product
- The Atmospheres Effect (Reactive or Corrosive) on Materials
- Volatiles and Moisture content of Materials

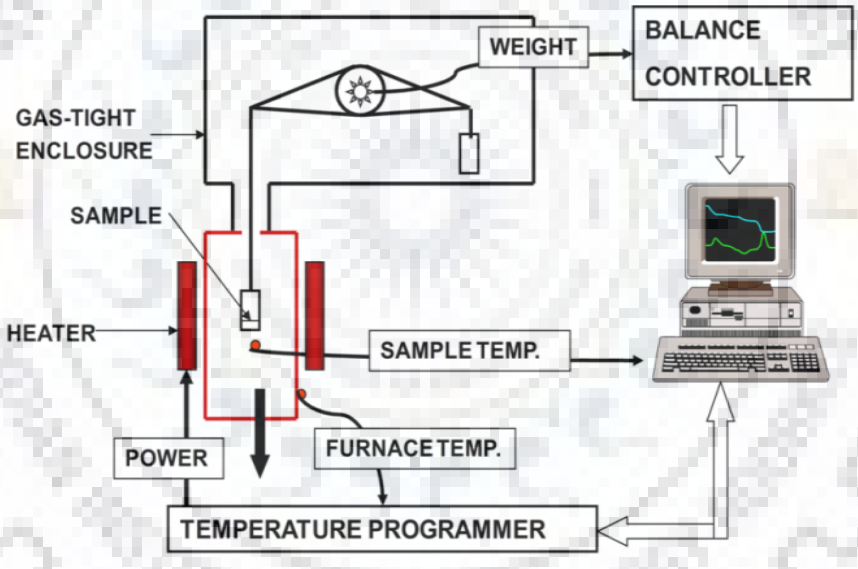

Figure 2.3 Schematic diagram for working principle of TGA

2.3 Field Emission Scanning Electron Microscope (FE-SEM):

Field emission scanning electron microscope (FE-SEM) is technique to investigate the surface morphology, microstructure, particle size, porosity and phase formation of samples. Either powders or polished pellets were used in the present study.

In this technique, a high energy electron beam (20 kV) is used to bombard the sample surface. When high energy electron beam scan the surface (strikes to the surface) then different types of radiations is generated by the specimen named as secondary electrons, backscattered

electrons (BSE),auger electrons(AE), characteristic X-ray ,cathodoluminescence (CL) and these radiations are detected by different detectors that produce the images. A FE-SEM provides an image of resolution between 1nm-10nm which is superior to light microscopy. Further for better resolution of images of specimen is seen by TEM. Components of SEM are shown in figure 2.4.. Moreover types of radiation are shown in table 1.4.

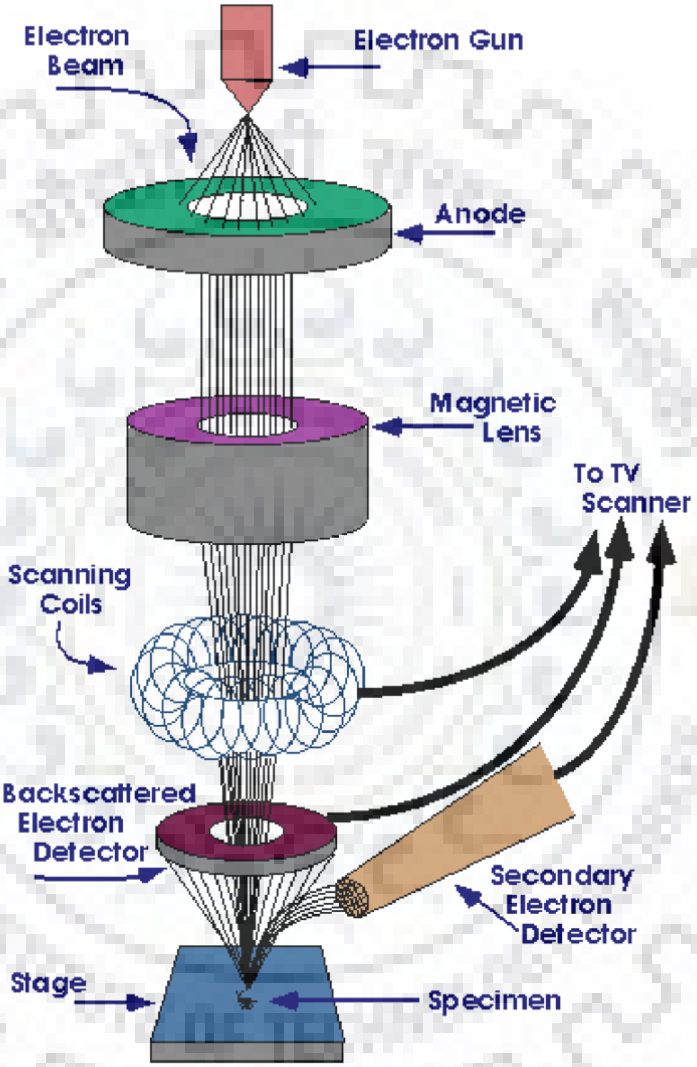

Figure 2.4 Working diagram of FE-SEM

Table1.4: List of radiations involved through the FE-SEM

Type of radition	Provide Concerned Information
Secondary electrons	Topographical information
Backscattered Electrons(SE)	Atomic numbers and phase differences
Auger electrons	Surface atomic compositions
Characteristic X-ray(EDX)	Thickness atomic composition
Cathodoluminescence	Electronic state information

If the electrostatic field at a tip of a cathode is increased sufficiently, the width of the potential barrier becomes small enough to allow electrons to escape through the surface potential barrier by quantum-mechanical tunnelling, a process known as field emission. The high acceleration gives greater resolution and allows for better observation of smaller objects than other emission methods.

2.4 EDX/EDS Energy Dispersive X-ray Spectroscopy:

Energy-dispersive X-ray Spectroscopy (EDX or EDS) is powerful, yet easy to use, technique that is ideal for revealing what elements and by inference chemical compounds are present in a particular specimen. Basically, EDS consists of detecting the characteristic X-rays produced by each element after bombarding a sample with high energy electrons in an electron microscope. Using a process known as X-ray mapping, information about the elemental composition of a sample can then be overlaid on top of the magnified image of the sample.

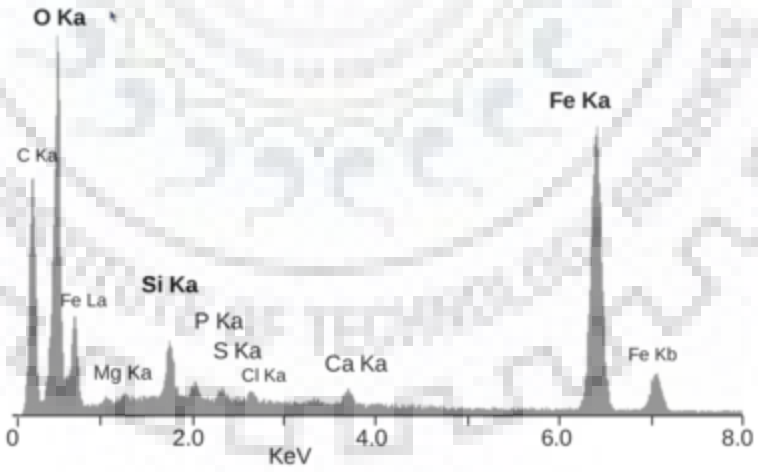

Figure 2.5 An energy-dispersive X-ray spectrum showing the main elemental peaks superimposed on the background

2.5 Inductively Coupled Plasma-Optical Emission Spectrometry (ICP-OES):

ICP-OES (Inductively coupled plasma - optical emission spectrometry) is a technique in which the composition of elements in (mostly water-dissolved or acid dissolved) samples can be determined using plasma and a spectrometer. The technique has been commercially available since 1974 and it reliable and multi-elements options.it has become a widely applied in both routine research as in more specific analysis purposes.

Principle:

The solution to analyse is conducted by a peristaltic pump though a nebulizer into a spray chamber. The produced aerosol is lead into argon plasma. Plasma is the fourth state of matter, next to the solid, liquid and gaseous state. In the ICP-OES the plasma is generated at the end of a quarts torch by a cooled induction coil through which a high frequency alternate current flows.

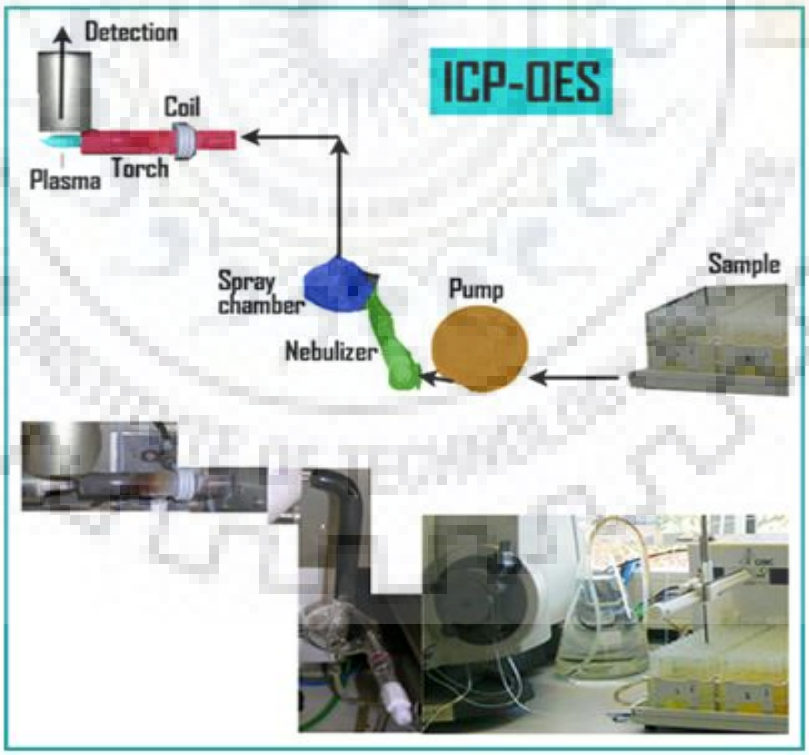

Figure 2.6: Schematic diagram of ICP-OES instrument

As a consequence, an alternate magnetic field is induced which accelerated electrons into a circular trajectory. Due to collision between the argon atom and the electrons ionization occurs, giving rise to stable plasma. The plasma is extremely hot, 6000-7000 K. In the induction zone it can even reach 10000 K. In the torch desolvation, atomization and ionizations of the sample takes place. Due to the thermic energy taken up by the electrons, they reach a higher "excited" state. When the electrons drop back to ground level energy is liberated as light (photons). Each element has an own characteristic emission spectrum that is measured with a spectrometer. The light intensity on the wavelength is measured and with the calibration calculated into a concentration.

2.6 Transmission Electron Microscope (TEM):

Transmission Electron Microscope (TEM) is influential technique to investigate the features of very small specimen. In this technique electrons penetrate a thin specimen and two types of phenomena occurs named as elastic electrons, incoherent elastic electrons and inelastic electrons are then imaged by appropriate lenses. Transmission electron microscopes (TEM) achieve high resolutions down to 0.1 nm while scanning electron microscopes (SEM) achieve resolutions up to a range of 1 nm, and are thus considerably better than optical methods.

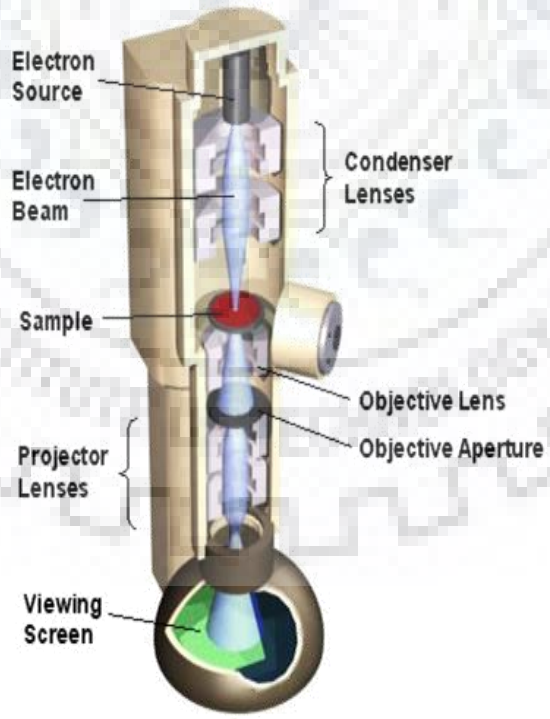

Figure 2.7 Schematic diagram of component of TEM

In the TEM there are electrons are accelerated from thermionic emission guns anywhere on the range 40–200 kV potential. For obtaining higher resolutions from TEM, it is required to developed with >1000 kV acceleration potentials. The field emission guns are becoming more popular as the electron guns due to their high brightness and very fine electron beams.

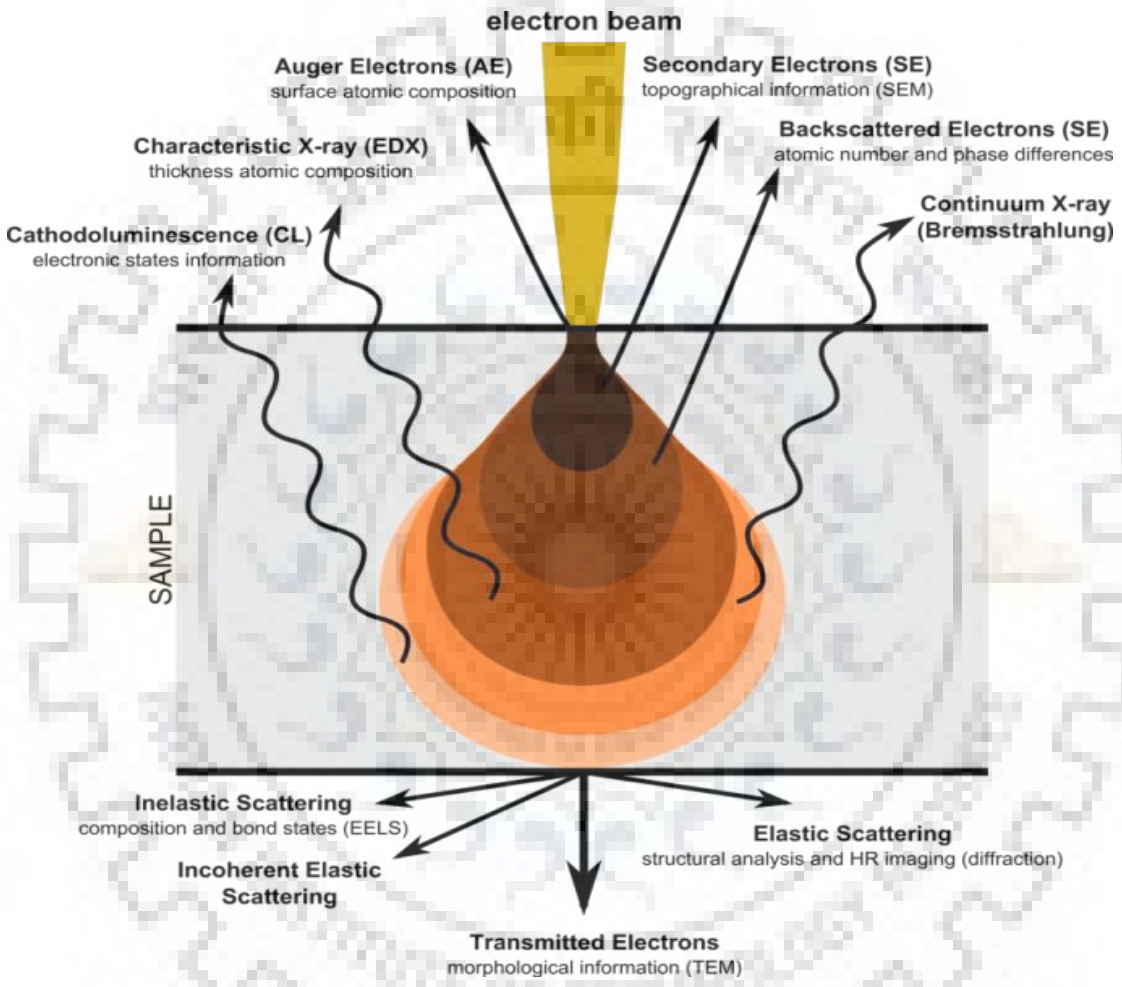

Figure 2.8 Schematic diagram of TEM and working principle

Diffraction pattern:

The planar section of the reciprocal lattice perpendicular to beam direction.

Also the zone of planes appearing as spots in the pattern.

Different types:

1. Kikuchi Patterns

2. Convergent-Beam Electron Diffraction (CBED)

3. Ring Patterns

4. Spot Patterns

2.7 **Fourier Transform Infrared (FTIR) Spectroscopy**:

Fourier transform infrared (FTIR) spectroscopy is an analytical tool used to understand the microscopic properties of a material by deducing the nature of bonds present. It provides qualitative information about the compound in mixture. The data collection is commonly done in the range of 4000-400 cm-1 for a specific number of scans (>100 scans). The working principle of FTIR spectroscopy is represented in figure 2.9.

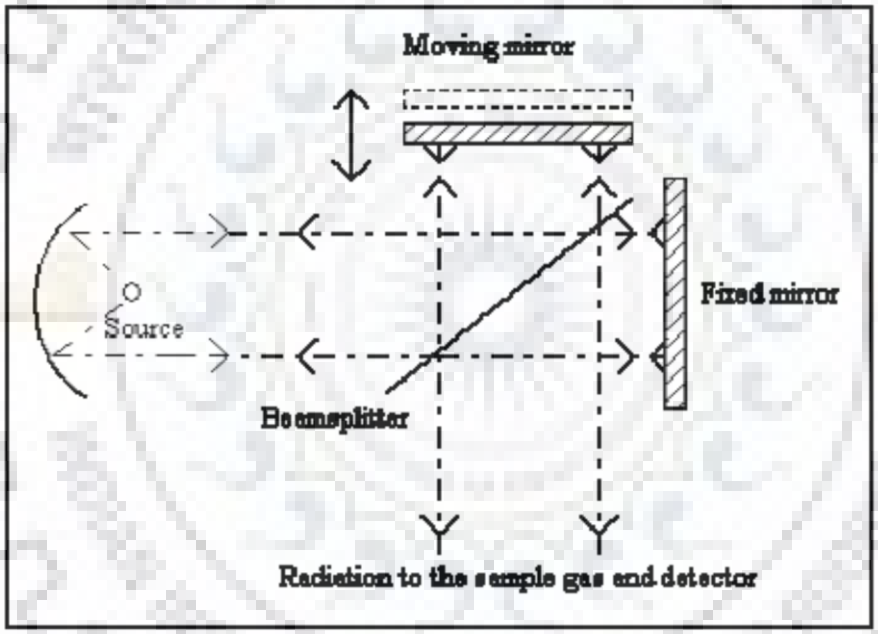

Figure 2.9 Michelson interferometer

When IR radiation is passed through the material, certain frequency is absorbed by the material when it matches with the natural vibrations of the bond. A unique frequency is absorbed by different bonds. The resultant transmittance is measured through the range of 4000-400 cm^{-1}. The focus of interest for us was checking the bands for carbonyl, O-H and Li-O bonds.

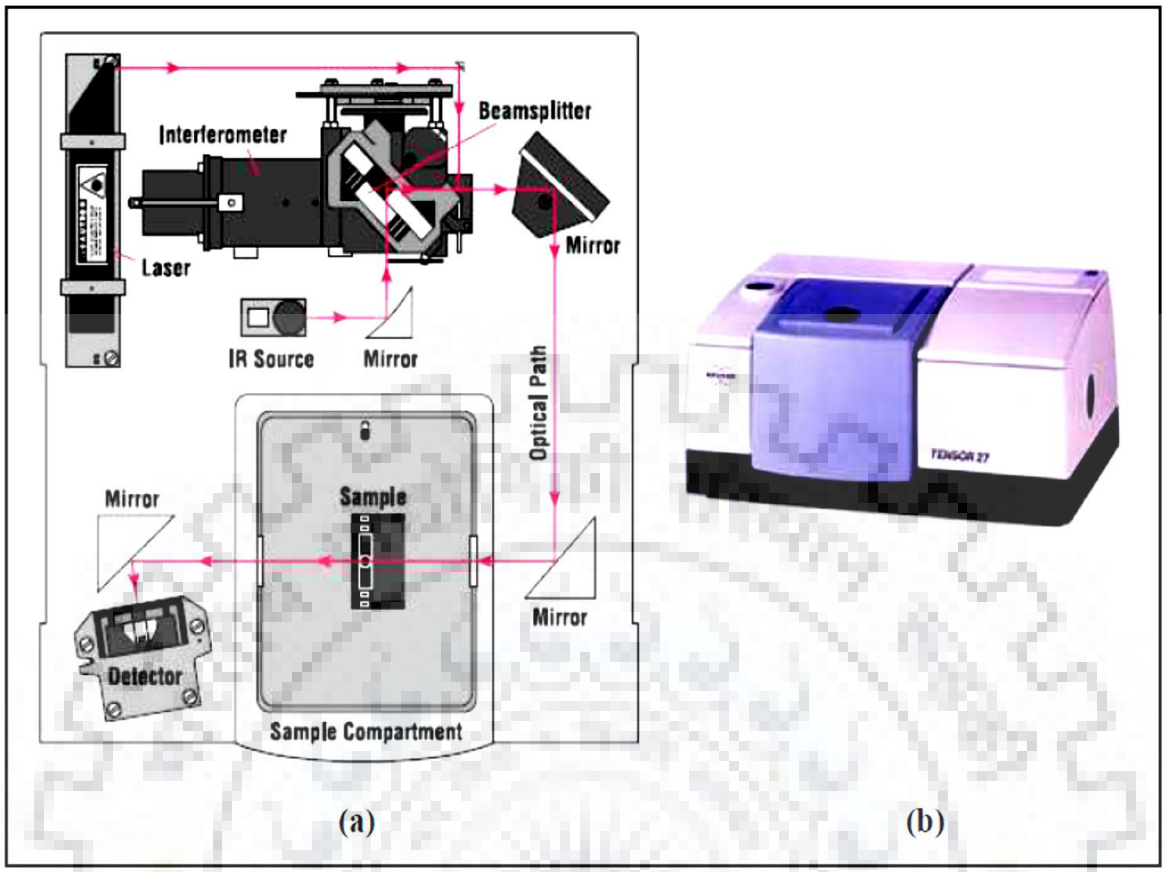

Figure 2.10 (a) Schematic diagram of FTIR and (b) FTIR instrument

Figure 2.10 shows Michelson interferometer divides radiant beams, and path differences take place. Further ray diagram can be understood.

2.8 Vibrational Sample Magnetometer (VSM):

The magnetism in the solid is an important property.in the modern concept, all materials, viz., metals, semiconductors and insulators are said to exhibit magnetism, through of different nature. The VSM is the apparatus used to measure the magnetic moment, the most fundamental quantity in magnetism, of solid samples.

When a sample material is placed in uniform magnetic field, it gets magnetised. The magnetic moment per unit volume developed inside a solid is called magnetization (**M**). there is another parameter called the magnetic susceptibility, **χ,** which is the measure of the quantity of magnetic material and is defined as the magnetization produced per unit applied magnetic field, i.e.,

$$\chi = M/H$$

Where **H** is the strength of applied magnetic field.

The magnetic induction or magnetic flux density **B** produced inside the medium as a consequence of the applied magnetic field H is given by

$$B = \mu_o (H+M)$$

Where μ_o is the permeability of free space or vacuum.

Ferromagnetic material exhibits a magnetic moment in the absence of a magnetic field. The magnetization existing in a ferromagnetic material in the absence of an applied magnetic field is called the *spontaneous magnetization*. The variation of magnetization with magnetic field is not linear for such type materials but forms the close loop called hysteresis loop. Some basic information about hysteresis loop is given below.

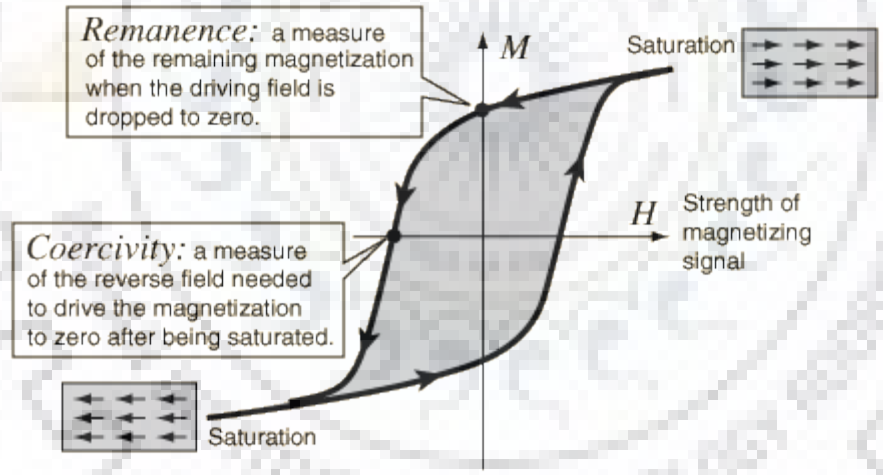

Figure 2.11 Magnetic hysteresis loop

A dipole moment is proportional to the product of sample susceptibility and applied field is induced in the sample. If the sample is made to undergo sinusoidal motion as well, an electrical signal will be induced in suitable located stationary pick-coils. This signal, which is at the vibration frequency, is proportional to the magnetic moment, vibration amplitude and

vibration frequency. The instrument displays the magnetic moment in e.m.u. units. The basic principle of operation for a vibrating sample magnetometer is that a changing magnetic flux will induce a voltage in a pickup coil.

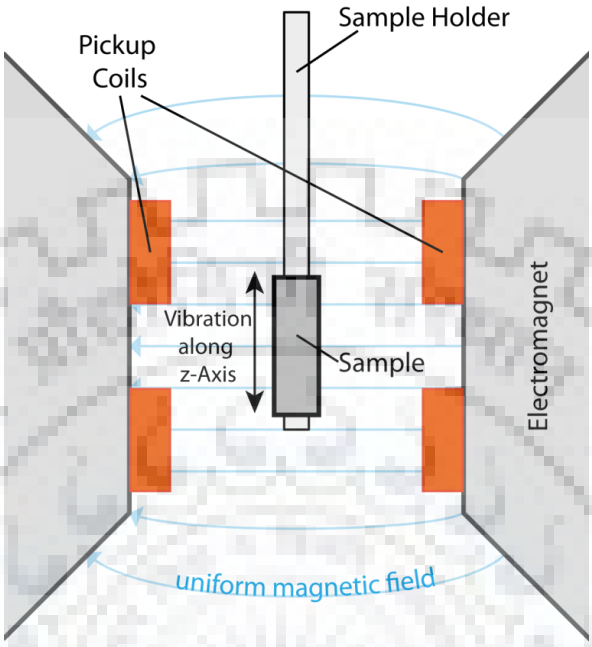

Figure 2.12 Working diagram of VSM

The sample is attached to the end of a sample rod that is driven sinusoidally. The center of oscillation is positioned at the vertical centre of a gradiometer pickup coil. The precise position and amplitude of oscillation is controlled from the VSM motor module using an optical linear encoder signal read back from the VSM linear motor transport. The voltage induced in the pickup coil is amplified and lock-in detected in the VSM detection module. The VSM detection module uses the position encoder signal as a reference for the synchronous detection. This encoder signal is obtained from the VSM motor module, which interprets the raw encoder signals from the VSM linear motor transport. The VSM detection module detects the in-phase and quadrature-phase signals from the encoder and from the amplified voltage from the pickup coil. These signals are averaged and sent over the CAN bus to the VSM application running on the PC.

2.9 Two Probe Method (Current-Voltage I-V measurement):

To measure the DC conductivity, make the pellet of the sample at a pressure 750 M Pasc. and then sintered it at a temperature 1000^0 C. Further to make the electrical contacts, the silver coating has been done on both the flat surfaces of pellet and heated at 80 ^{0} C for 45 min.[14]

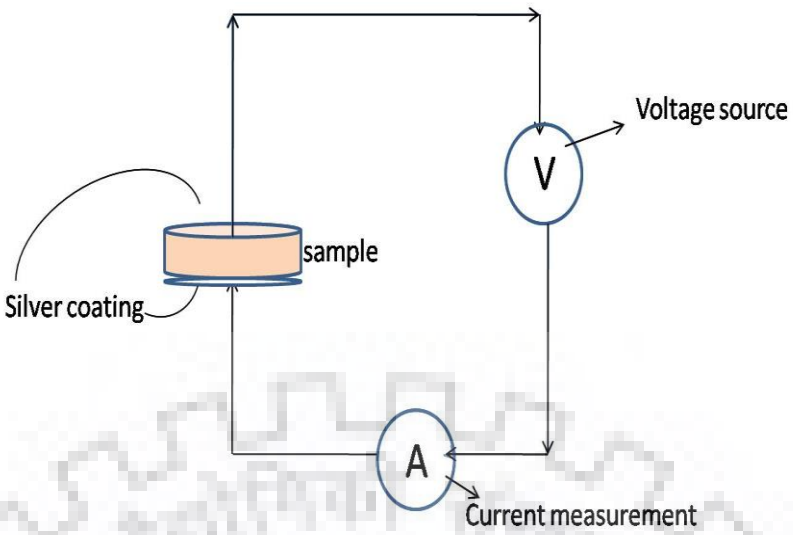

Figure 2.13 Schematic diagram of two prob mechasims

DC conductivity of the sintered LLZO pellet has been determined by using I-V characteristics at room temp with two probe method. The DC conductivity is given by the following equations

$$\sigma = \frac{1}{R} * \frac{t}{A}$$

Where R = V/I is the resistance, t and A ($= \pi r^2$) are the thickness and cross sectional area of the pellet respectively[15]. Further the current was measured by changing the voltage to measure the DC conductivity.

2.10 AC Conductivity Measurement:

2.10.1 LCR Meter:

LCR meter is an instrument which is used to measure resistance, capacitance and inductance of an electronic circuit. In LCR meter a silver pasted pellet is subjected to measure the impedance, phase angle, capacitance and inductance using AC signal. In complex representation, impedance is written as

$$\boldsymbol{Z = \frac{E}{I} = Z_0 \exp(i\theta) = Z_0(cos\theta + isin\theta)}$$

It may be shown as **Z=Z'+iZ"**

Above equation is composed of real and imaginary part of impedance. To construct Nyquist plot (Z´ and Z´´), real part of impedance is taken on X-axis and imaginary part of impedance on Y-axis. The AC impedance measurement of Fe-doped LLZO has also been performed using

LCR meter (WAYNE KERR 6500-P) in the frequency range of 1Mhz to 100 Hz at different temperatures (298-473 K).

2.10.2 Electrochemical Impedance Spectroscopy (EIS)*:*

EIS is a non-destructive technique to evaluate the kinetics of electrode material. For EIS measurement of a battery, the cell was kept at a certain voltage and then impedance was measured in the form of Nyquist plot at constant potential amplitude for a frequency range. AC impedance spectra provide detailed information about electrochemical system. Electrochemical reactions like charge transfer at the electrode surface is a high rate process and occurs at high frequency region whereas mass transfer from the bulk solution to the electrode surface is low rate process, and observe at low frequency region. These processes can be represented by electric circuit.

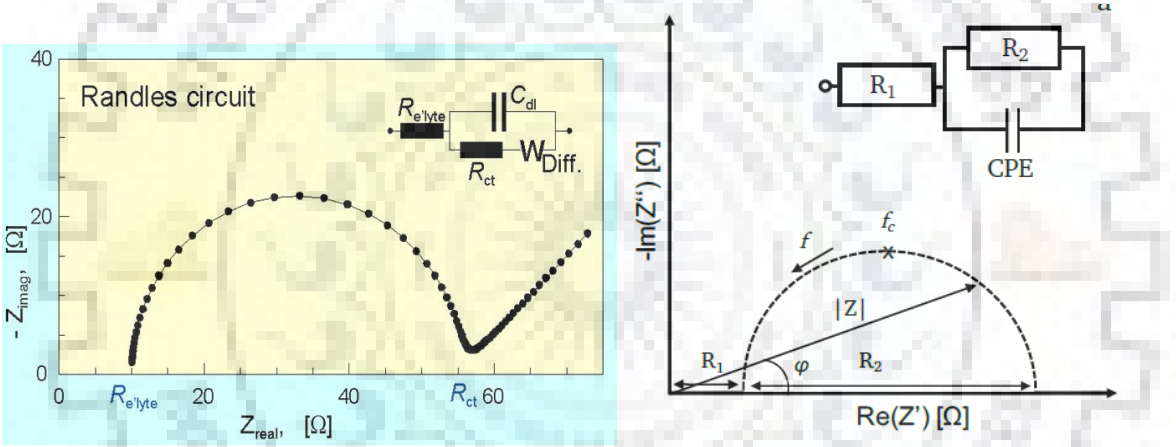

Figure 2.14 Nyquist Plot and eqivalent circuit obtain from EIS

An electric circuit may consist of resistance, capacitors, or constant phase elements combined in parallel or in series. The quantitative analysis was done from fitting an equivalent circuit to the obtained Nyquist plot. Figure 2.14 is an example of impedance plot of the simple circuit with a capacitor and a resistor in parallel.

Given Capacitance values

Table 1.5 Overview of the capacitance values and their corresponding phenomenon

Capacitance [F]	Phenomenon Responsible
10^{-12}	bulk
10^{-11}	minor, second phase
$10^{-11} – 10^{-8}$	grain boundary
$10^{-10} – 10^{-9}$	bulk ferroelectric
$10^{-9} – 10^{-7}$	surface layer
$10^{-7} – 10^{-5}$	sample-electrode interface
10^{-4}	electrochemical reactions

CHAPTER 3

SYNTHESIS AND CHARECTERIZATION OF $Li_7La_3Zr_2O_{12}$ AND $Li_{7-3x}Fe_xLa_3Zr_2O_{12}$

3.1 Introduction:

For safe energy storage, solid electrolyte plays a major role in Solid state batteries. Among the all inorganic(ceramic) electrolytes garnet is the more dominant due to its high stability with cathode and anode material and also other properties are encountered like high ionic conductivity (10^{-4} S/cm) as well as good thermal and chemical stability which has been discussed in chapter. Cubic phase reveals more ionic conductivity over tetragonal phase which has been discussed. In this chapter different synthesis route and characterization techniques like **XRD, TGA/DTA, FESEM, TEM, EDX, ICP-OES,VSM, FTIR** and electrical measurement **like IV, EIS** for both phases of nanostructured LLZO also reported in this chapter. For the synthesis of cubic phase LLZO first we tried sol gel method. Then after the conventional Solid state method at high temperature 900-1100^{0}C is used to synthesis tetragonal and cubic phase of LLZO. The doping is essential part of synthesis to stabilizing of cubic phase at lower temperature 1050^{o}C[11]. The formation of both phases is confirmed by XRD and refinement is also reported in this chapter. In addition the thermal stability of both phases of LLZO at high temperature is also confirmed by TGA analysis.

3.2 Experimental Section:

3.2.1 Bare LLZO (t-LLZO):

Solid state route is followed for synthesis of t-LLZO in which all precursors Li_2CO_3, La_2O_3, ZrO_2 are taken in stoichiometry ratio. Since Li exhibits volatile nature at higher temperature hence 10% excess of Li_2CO_3 is also taken to compensate the Li loss during high temperature. These precursors are mixed by hand mortar pestle for 12 hours. This mixing is done without much interval to avoid the moisture and H ion exchanging mechanism with Li. Then after calcinations has done in tube furnace at 600^{o}C for 6 hours. After this the powder was mixed for entirely phase mixing. The pellet of powder was prepared at the pressure 780M Pascale and sintered at 900^{o}C for 12 hours for densification which increase inter-particle contact. Then structural, morphological and thermal characterization of prepared powder

sample was done. The schematic flow diagram for synthesis steps which are taken during the formation is also shown here in figure 3.1.

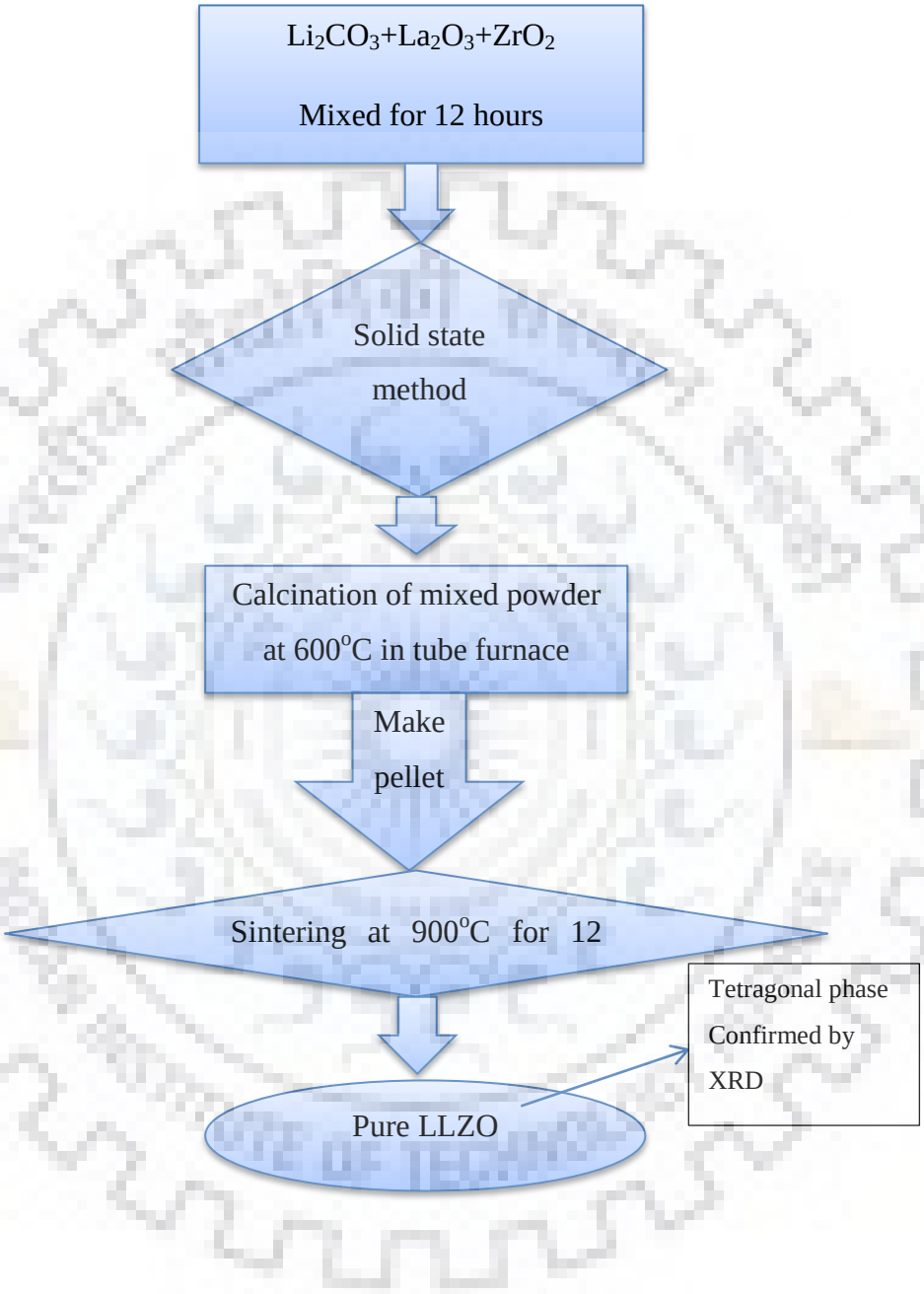

Figure 3.1 Flow chart of synthesis of LLZO

The Structural characterization of tetragonal LLZO has been confirmed by X-Ray diffraction, which was done by CuK_α equipped X-ray diffractometer (XRD- RIGAKU ULTIMA IV) operated on voltage 40 kV and current of 40 mA. The morphological

characterization has done by FE-SEM (FESEM- MIRA 3 TESCAN) and the elemental composition analysis has been investigated by Energy Dispersive X-Ray Spectroscopy (EDX). The TGA-DTA and DTG reveals the thermal stability of material up to 1000 ^{0}C. For Electrical measurement of LLZO pellet (with electrical contact on upper and lower surface by silver) is also investigated by DC conductivity by using two probe set up (KEITHLEY 6571AP). Moreover the Electrochemical Impedance Spectroscopy (EIS) measurement has been investigated by AUTOLAB-MAC 80039 in the high frequency region to low frequency region (1Mz to 0.001 KHz) from which Nyquist plot obtained (between real Z and Imaginary Z). The total resistance of pellet is calculated by Nyquist plot and further ionic conductivity is calculated by formula $\sigma = \left(\frac{t}{ZA}\right)$ where t is thickness of pellet and A is the cross sectional area of pallet.

3.2.2 Fe-doped LLZO (c-LLZO):

Syntheses of cubic phase of LLZO are by tried two methods conventional solid state method and sol-gel process.

The **solid-state reaction route** is the most widely used method for the preparation of polycrystalline solids from a mixture of solid starting materials. Solids do not react together at room temperature over normal time scales and it is necessary to heat them to much higher temperatures, often to 1000 to 1500 °C in order for the reaction to occur at an appreciable rate.

In Solid state method all precursors Li_2CO_3, La_2O_3, ZrO_2 and0.2 mole of Fe_2O_3 are taken in stoichiometry ratio with 10% excess of Li_2CO_3 to compensate the Li loss during high temperature[13]. These precursors are mixed by hand mortar pestle method for 10 hours without any interval because Fe_2O_3 could react with air atmosphere. The mixed powder was kept in furnace at 900^{o}C for 6 hours and after room temperature sample was checked by XRD to determinate impure phases. Again powder was mixed at room temperature for entirely phase mixing and increase surface area. The prepared powder was pressed at 750M Pascale and this pellet reheated at 1050^{o}C for 15 hours for densification and sintering. This pellet again crushed and XRD of prepared sample was done. The schematic flow diagram is shown in figure 3.2.

Li_2CO_3+La_2O_3+ZrO_2+Fe_2O_3

Mixed for12 hours

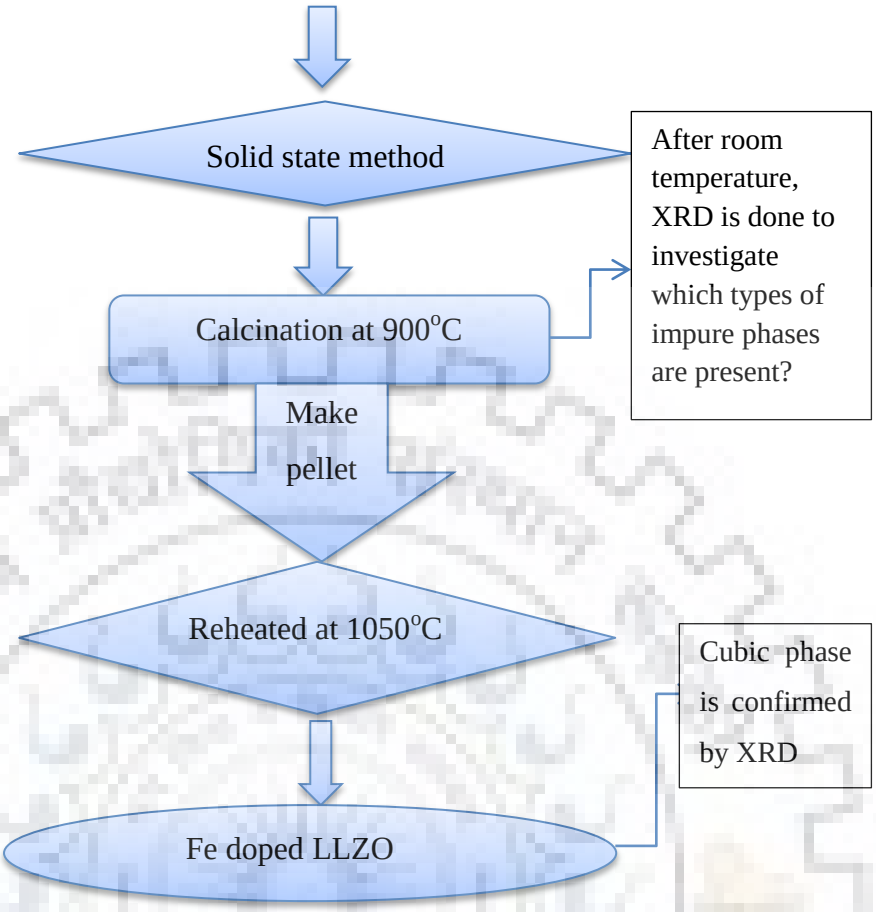

Figure 3.2 Flow chart of Synthesis of Fe-LLZO

3.3 Fe-doped LLZO by Sol-gel method:

This method has been tried to achieve Fe-doped LLZO. In several literatures t-LLZO phases are reported by this synthesis route sol-gel method without any foreign element doping, but here the procedure are focused on stabilizing the cubic phase of LLZO because the cubic phase of LLZO shows 100 times more ionic conductivity than tetragonal phase of LLZO[14]. The nitrate precursor of Li, La, and Zr are used for synthesis in this method because nitrate precursors may be easily dissolved in water.

$LiNO_3$, $La(NO_3).6H_2O$, $ZrO(NO_3).6H_2O$ and Fe_2O_3 all these precursor are taken in stoichiometric ratio and dissolved in distilled water, and then ethylene glycol and citric acid (2:1) were added to solution. The whole solution was stirred for 12 hours at 40°C. Transparent gel form (viscous solution) of solution took place after crossing the temperature 60°C. Again

further heat treatment was followed to obtain thick yellow gel from colourless solution. Finally brown colour gel was placed at 200^{o}C in furnace for 6 h under the air atmosphere. The heated precursor was grinded by hand mortar pestle. In the last step the powder was placed in furnace 500^{o}C in the air atmosphere for 5 hours. Finally obtained sample characterized by XRD. The flow diagram is shown below

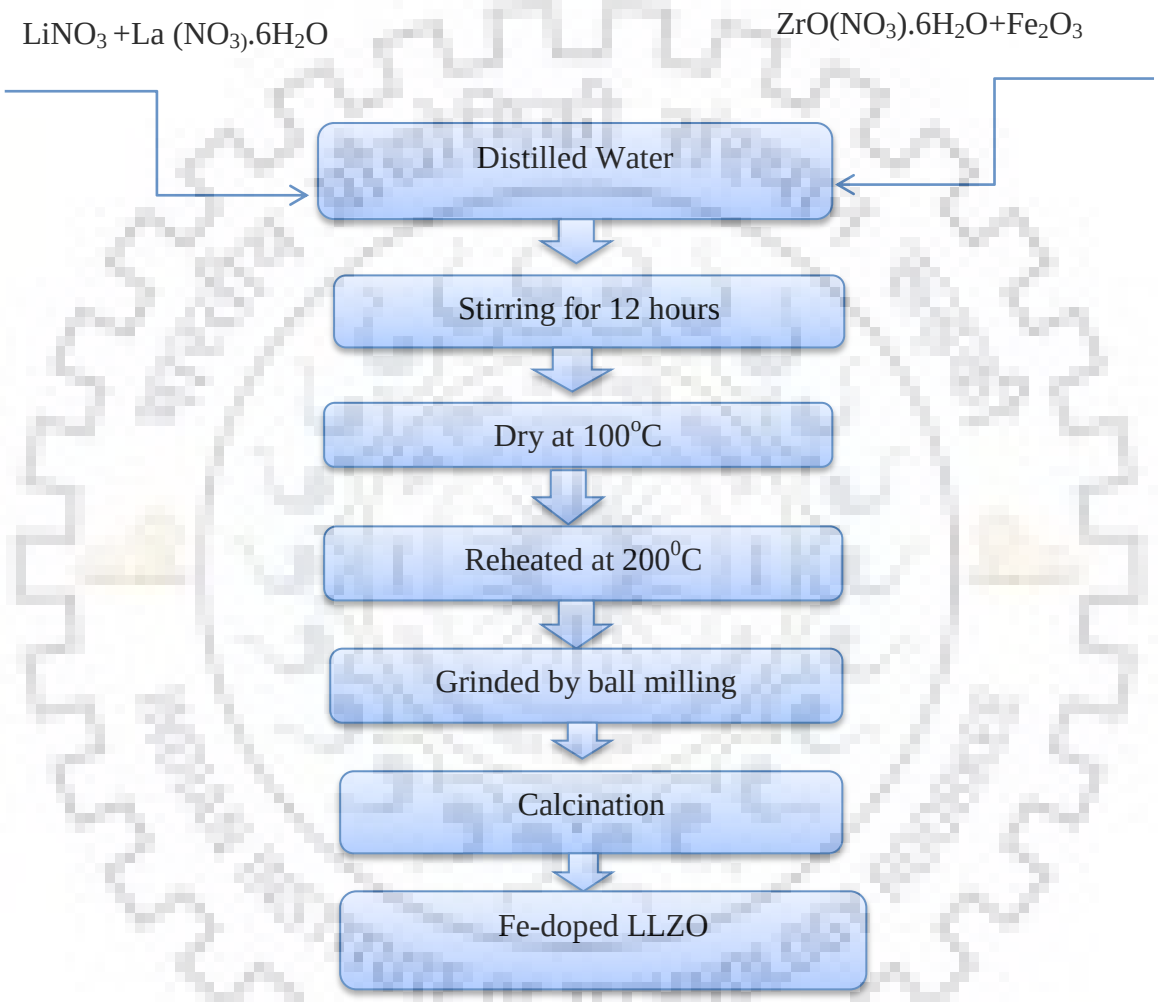

Figure 3.3 Flow chart of Synthesis of Fe-LLZO by sol-gel method.

3.4 Results and Discussions:

3.4.1 Phase Characterization (XRD):

The XRD pattern of bare LLZO ($Li_7La_3Zr_2O_{12}$) is shown in figure 3.4(b) which synthesized without any foreign element doping at 950^oC temperature by solid state reaction. The XRD pattern attributed to the formation of LLZO having tetragonal structure with $I4_1/acd$ space group identified by JCPDS card no. 45-0109 with two minor impurities of $La_2Zr_2O_7$ and La_2O_3. The Cubic phase is stabilized by doping of Fe at 24d tetrahedral Li sites at temperature 1050^oC for 26 hours with step heating treatment which confirmed by XRD shown in figure 3.4(a). The loss of Li at high temperature and improper phase formation also can be seen from XRD.

The tetragonal phase formation without any sintering aid could possible only due to proper step heating treatment in appropriate temperature range and trade of mixing and grinding time during synthesis. In the case of doping of Fe on Li sites, the cubic phase formation of LLZO at lower temperature due to Li distribution in Li(1) and Li(2) sites which confirmed by Rietveld refinement (PDXL-2) having Ia3-d space group. The densification of sample by making pellet is also helpful for formation of pure tetragonal and cubic phase.

By sol-gel method cubic phase of Fe-doped LLZO is achieved. But this method is not good for synthesis of garnets (LLZO) because garnets are a oxide material. If we look at internal mechanism of synthesis of LLZO all precursors of nitrate which are taken in sol-gel method transforms in oxides through the evolution of nitrates. So some impurities of nitrate precursors and oxides take place during the synthesis of LLZO. XRD of Fe-doped LLZO by this method is shown in figure 3.5. So at last the results from sol-gel method are not fruitful and this method is not best in economical manner due to cost of nitrate precursors are high as comparison to oxide precursors of Li, La, Zr etc.

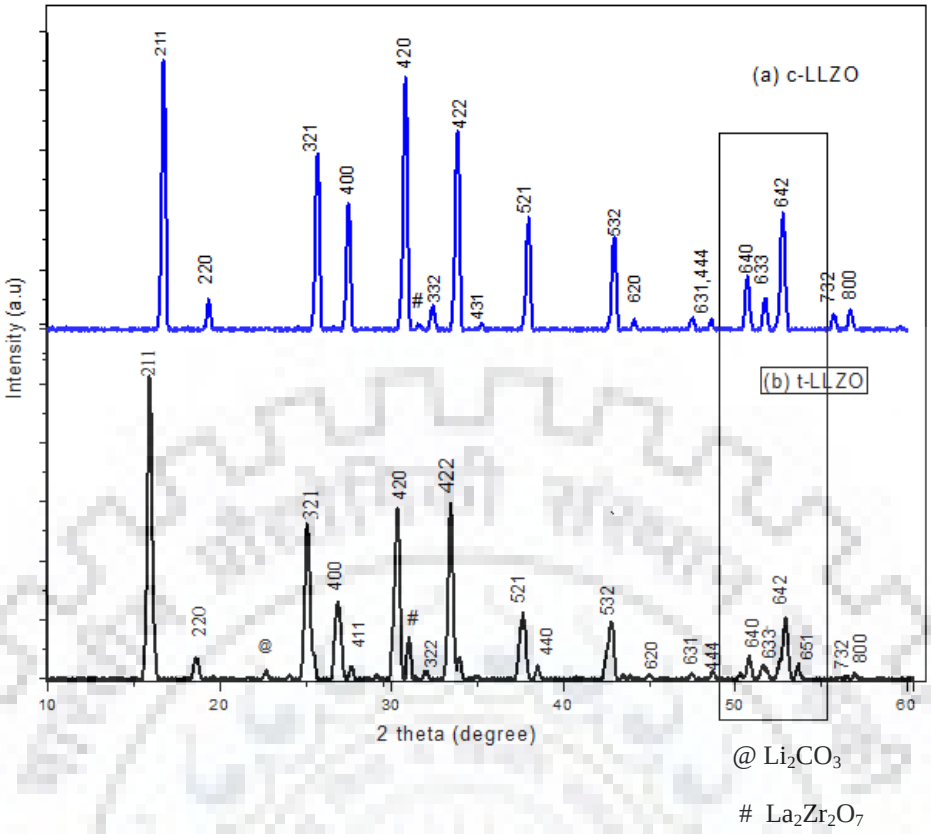

Figure 3.4 XRD pattern of (a) tetragonal-LLZO and (b) cubic Fe-LLZO.

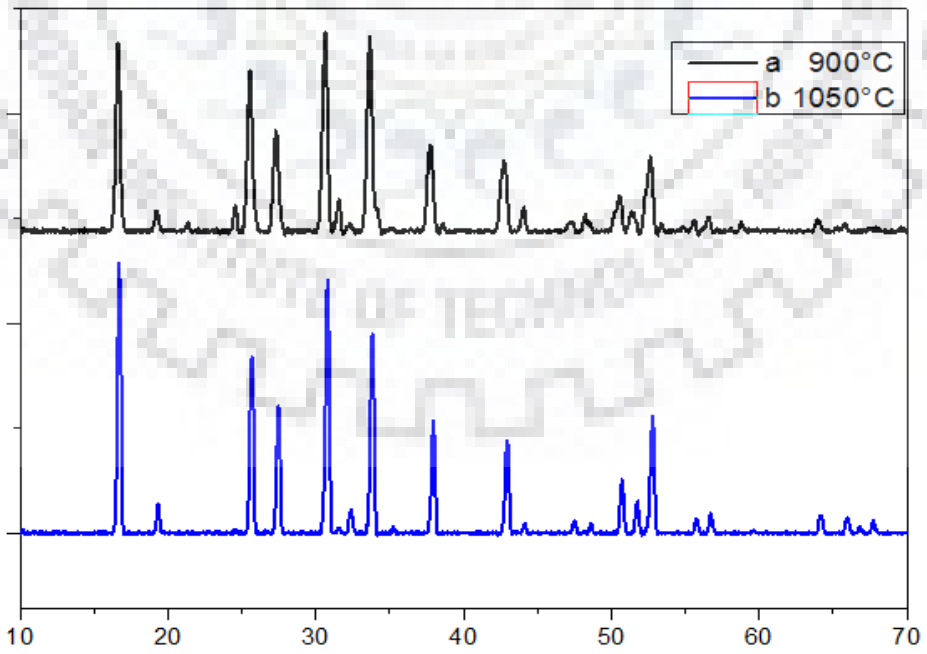

Figure 3.5 XRD pattern of cubic Fe-LLZO at different temperature 900°C &1050°C.

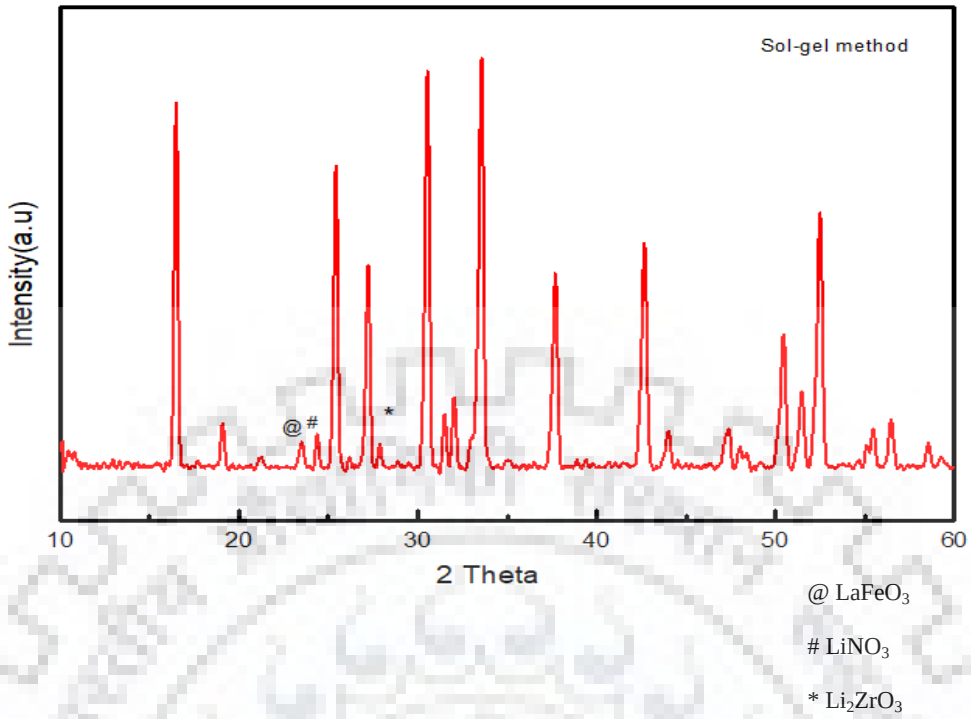

Figure 3.6 XRD pattern of Fe-LLZO by sol gel synthesis with assigned impurity peaks.

Fe-doped LLZO by Sol-gel method having more impurities as compared to solid state route synthesis.

3.4.2 Rietveld Refinement of t-LLZO and Fe-LLZO:

At lower temperature 950^{o}C there are some impurity of Li_2CO_3, $La_2Zr_2O_7$.[13]and La2O3 is observed in XRD pattern which is not appeared at higher temperature about 1050 ^{0}C. The refinement of above XRD shows good agreement with reported literature with high goodness of fitting t-LLZO and c-LLZO (Chi^{2}=2.45, 2.26). From refinement the calculated lattice parameter for tetragonal and cubic phase is a=b=12.994 A^{0}and c=13.027Å and 12.991Å respectively, which confirmed the lattice parameter decreases by doping of Fe at Li sites.

Table 1.6: Rietveld refined results of t-LLZO and Fe-LLZO

Electrolyte / Parameteres	t-LLZO (Tetragonal structure)	Fe-LLZO (Cubic structure)
Chi^2	2.45	2.26
Lattice parametre	a =b =12.994Å c =13.027Å	a = b = c = 12.991Å

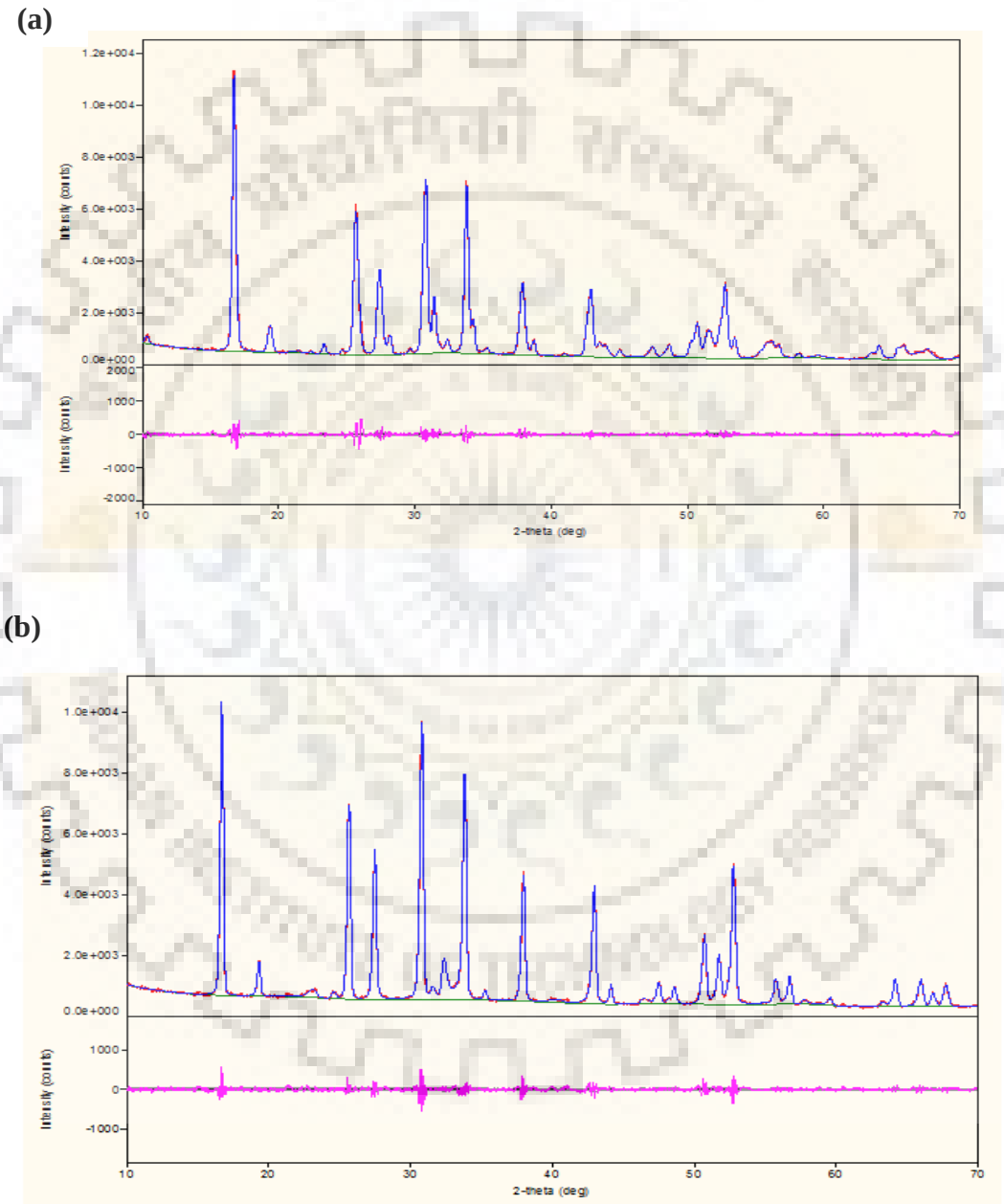

Fig3.7: Rietveld refinement of (a) t-LLZO and (b) Fe-LLZO (where red line shows goodness of fitting).

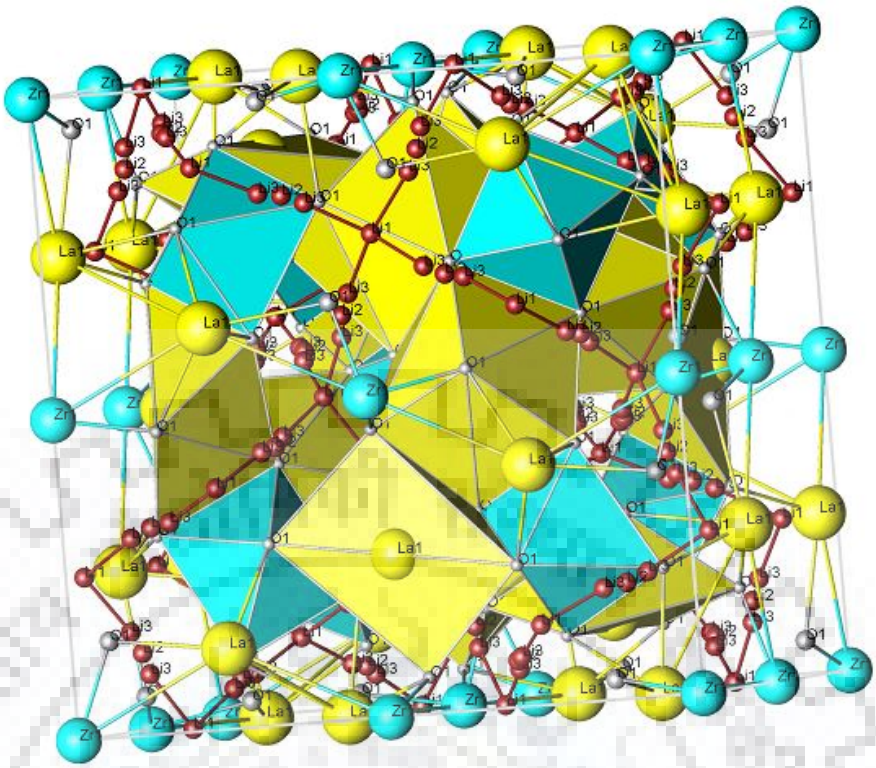

Figure 3.8 Structure of t-LLZO obtain after refinement of XRD.

The three dimensional arrangement of atoms in garnet system is shown in figure 3.8 which is obtained as result of refinement of tetragonal LLZO. This shows the occupancy of Li in different sites, that distribution decides the phase of LLZO and its conductivity as well. From the XRD, the particle size calculated by using Scherrer formula is order of 50-60 nm which have also good correspondence with FESEM results.

3.4.3 Morphological and Elemental Analysis (FESEM, EDX and TEM):

The morphology of t-LLZO and Fe-doped c-LLZO is shown in fig 3.9 and 3.10 respectively. Here in the homogeneous particle size of order of 20-50 nm which has good agreement with XRD results (Scherer's formula). From this fig it is clearly seen that there is poor densification in t-LLZO as compared to c-LLZO[15]. The size of particle plays a critical role in material sintering. In general smaller size corresponds to greater incentive for sintering due to higher surface area. At same time reduction in particle size leads to poor necking which create problems to make full densification.

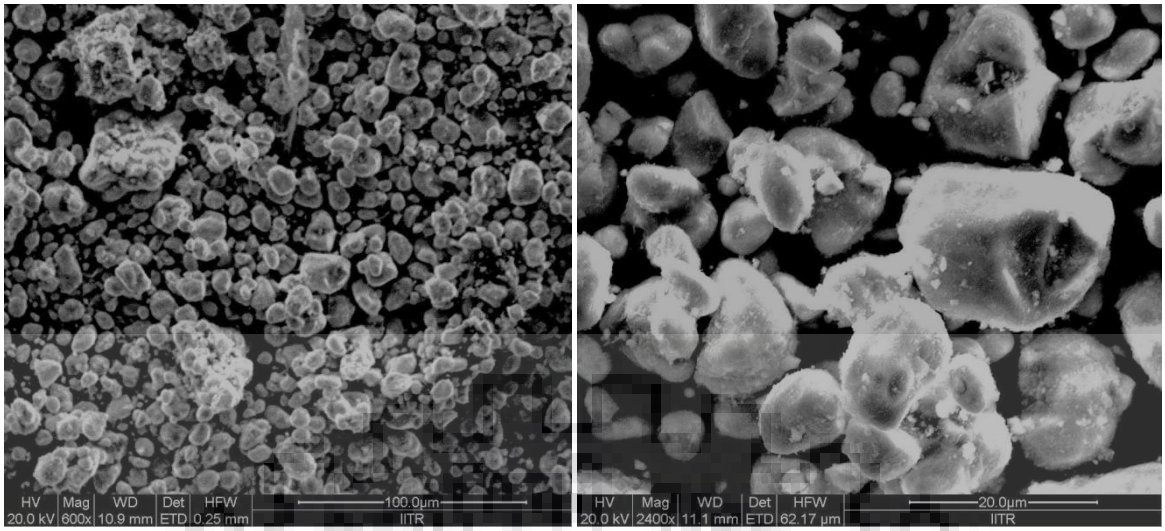

Figure 3.9 FE-SEM image of t-LLZO with different resolution

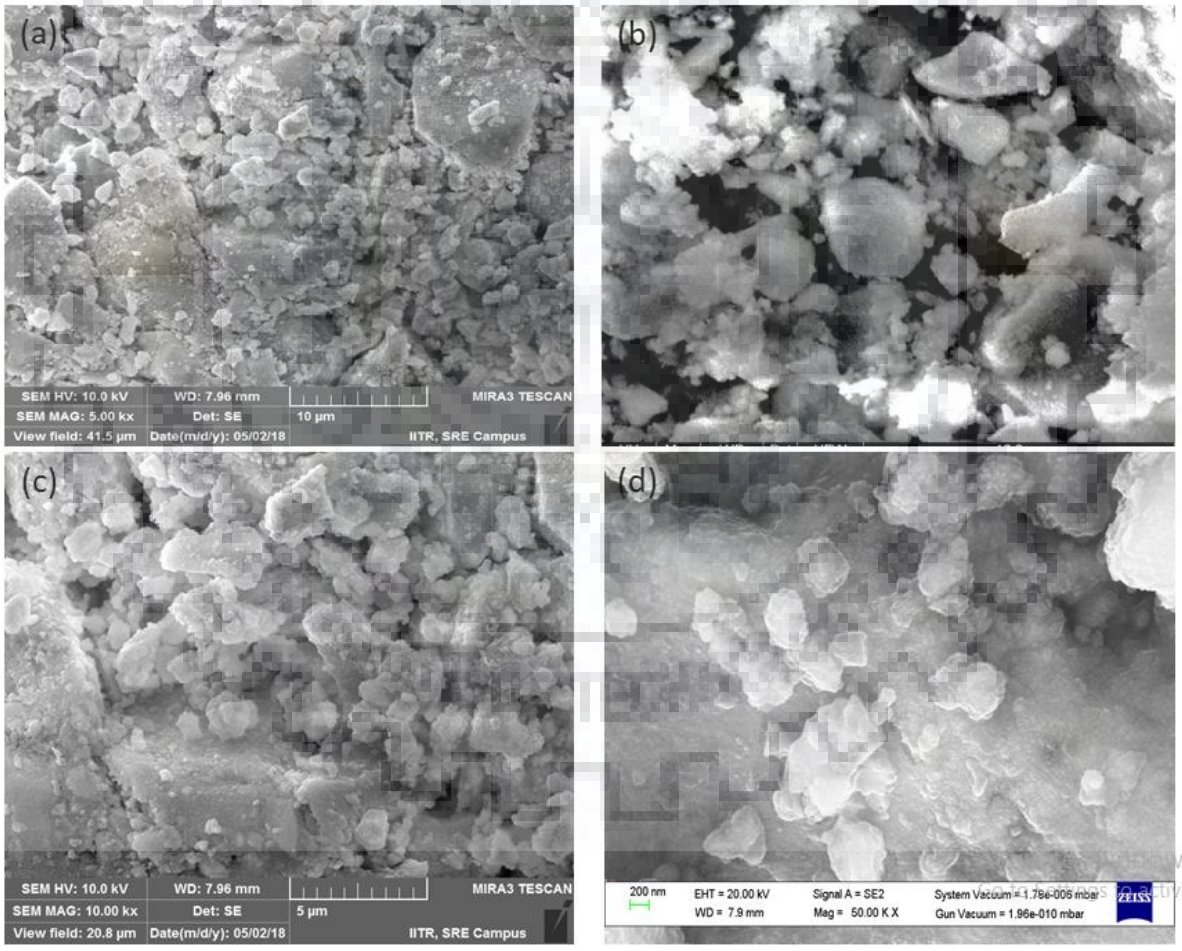

Figure 3.10 FE-SEM image of Fe-LLZO with different resolution

The elemental analysis is confirmed the occupancy of La, Zr, O inside the material with similar ratio which have taken during synthesis. The amount of Li inside the material cannot be confirmed by EDX, hence for this we plan for ICP-MS or XPS in future.

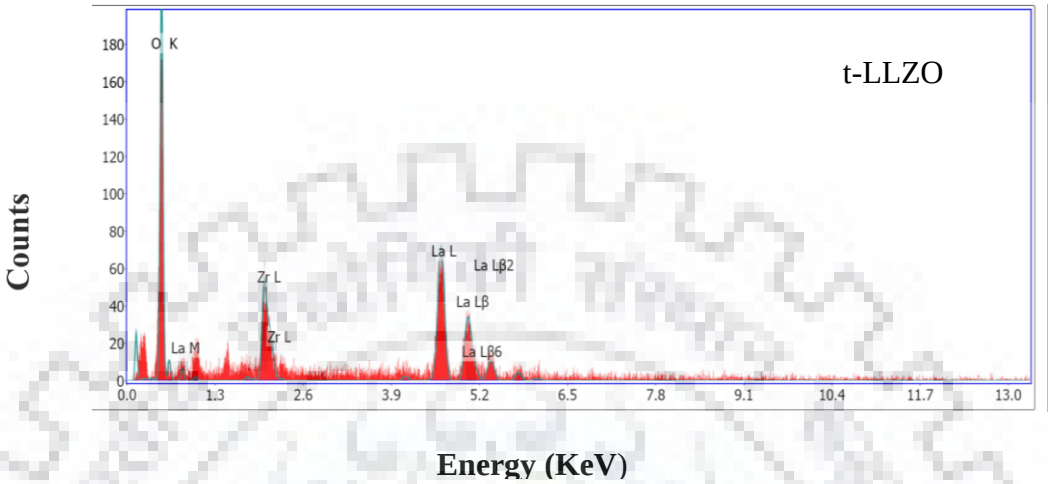

Element	Weight %	Atomic %	Net Int.	Error %
O K	38.77	83.15	75.08	9.42
ZrL	13.35	5.02	29.47	6.15
LaL	47.88	11.83	58.73	3.34

Figure 3.11 Elemental analysis of t-LLZO by EDX

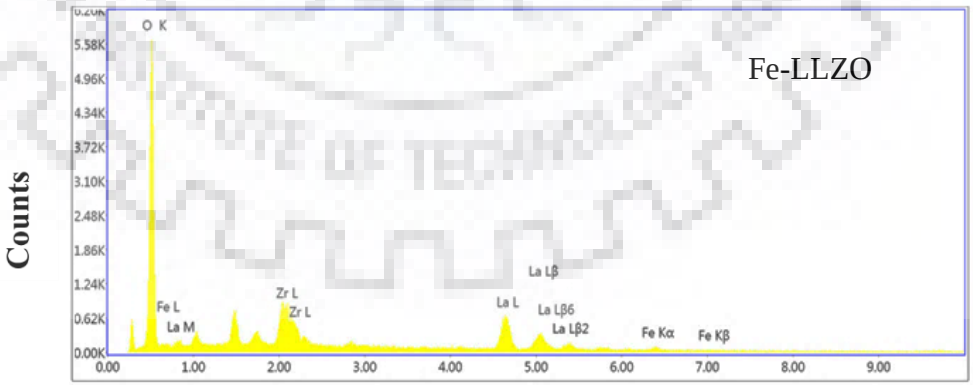

Figure 3.12 Elemental analysis of Fe-LLZO by EDX

Element	Weight %	Atomic %	Net Int.	Net Int. Error
O K	47.71	86.82	1087.3	0.01
ZrL	12.11	3.86	214.8	0.02
LaL	37.29	7.82	239.6	0.04
FeK	2.88	1.5	22.9	0.22

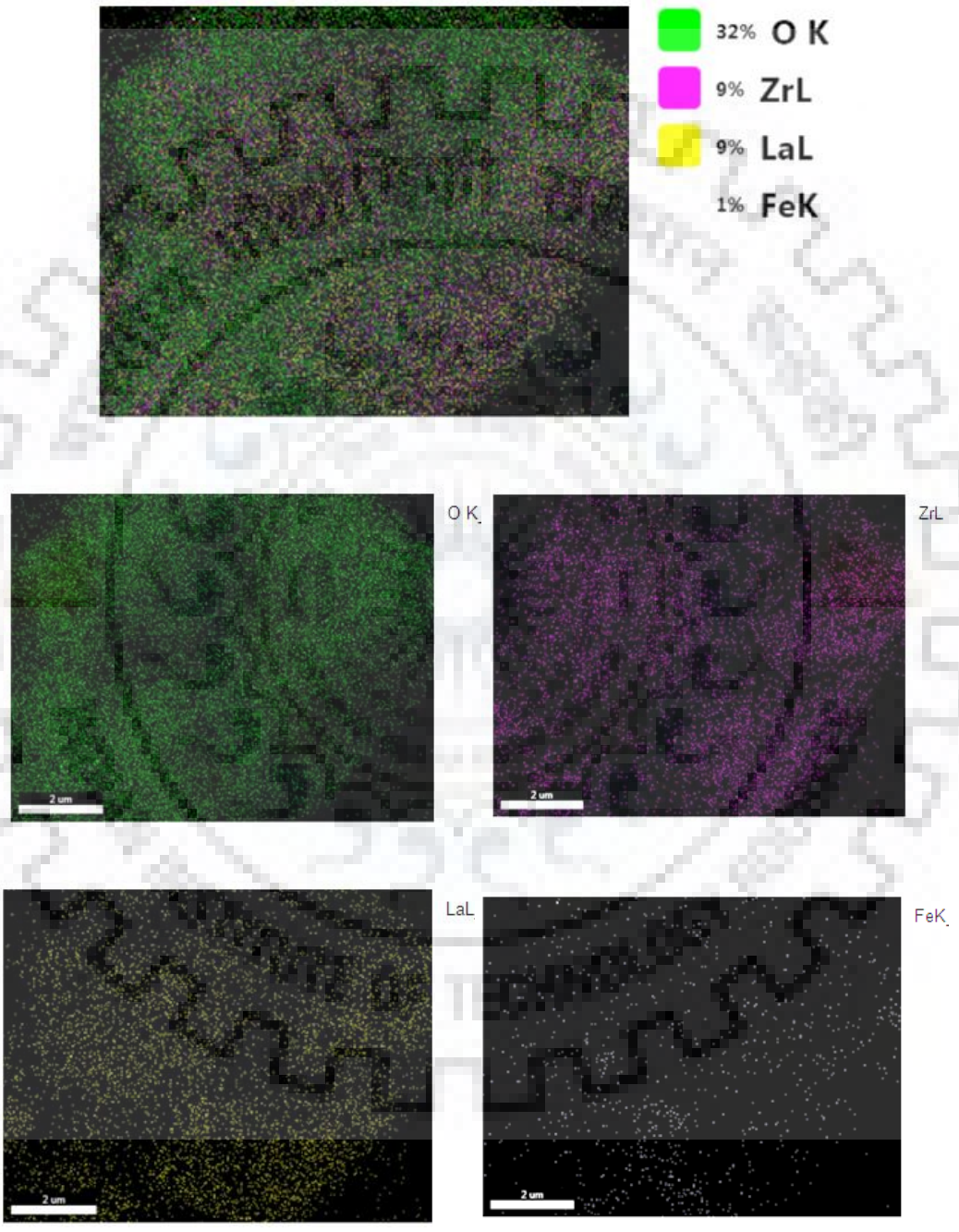

Figure 3.13 Elemental analysis of Fe-LLZO by EDX and Atomic % of element

The TEM results are shown in figure 3.14,3.15, which have similar conclusion to XRD. The SAED pattern shows good crystallinity of t-LLZO and Fe-doped c-LLZO system with large grains and interplaner separation is order of 6-6.5Å.

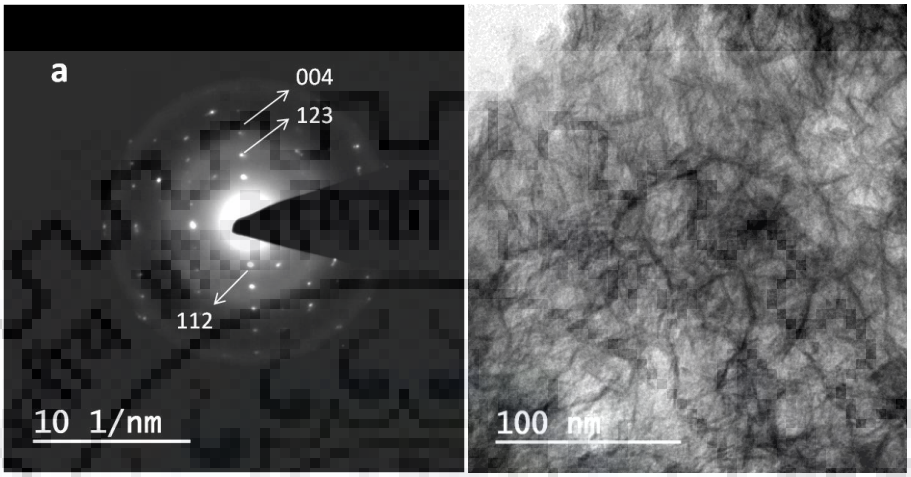

Figure 3.14 TEM image of t-LLZO

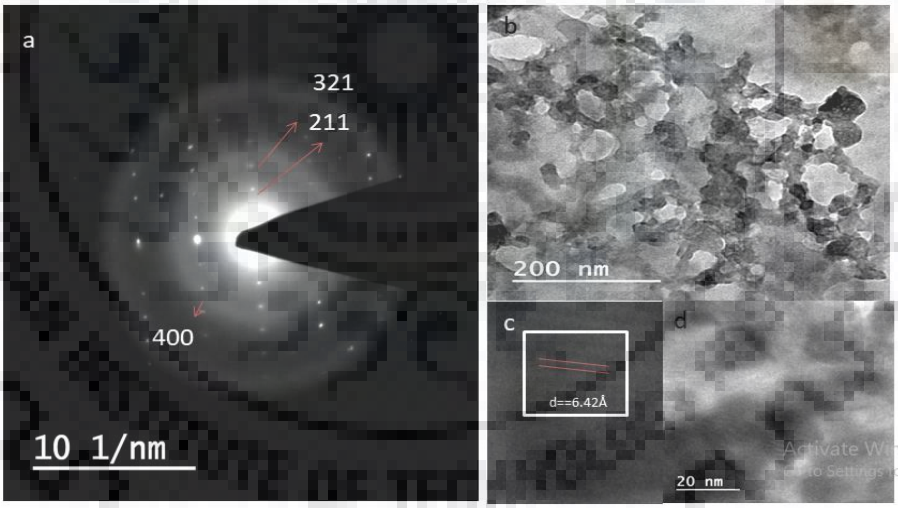

Figure 3.15 TEM image (a) SAED pattern of Fe-LLZO (b,d) high resolution TEM image (c) Interlayer spacing and grains (inset).

3.4.4 Inductively Coupled Plasma-Optical Emission Spectrometry (ICP-OES):

Because Li cannot be detected by EDX spectrum due to its low atomic number (Z=3). When LLZO is synthesized the probability of Li loss could be taken and undesired phase formation through the air atmosphere like Li_2O, Li_2CO_3 etc.

Li is detected by ICP-OES method successfully. The processor is typical as comparison to EDX. The experimental steps are shown through the flow chart.

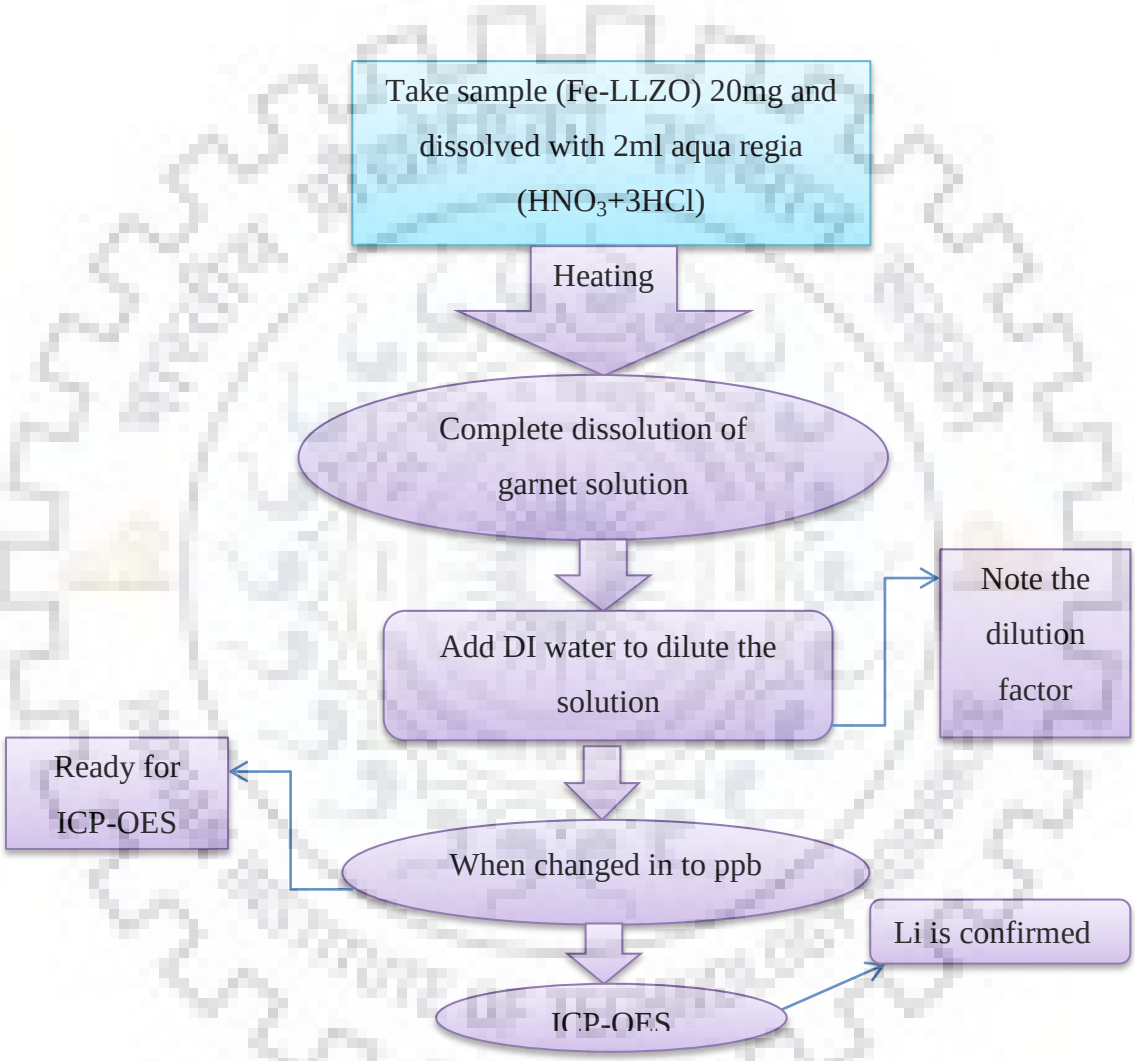

Figure 3.16 Flow chart for ICP-OES process

The ICP-OES result is shown as

Analyte	Mass	Conc. Mean (ppb)
Li	7	530.887

ICP-OES confirmed the Li in Fe-LLZO. Minor Li loss takes place during the synthesis of Fe-LLZO which is supported by Li concentration by result as comparison to experimentally Li concentration in Fe-LLZO.

3.4.5 Thermal Stability Analysis (TGA-DTA-DTG):

The TGA curves reveals the different steps during formation of LLZO as shown in Figure 3.17, which is result of different weight loss during heat treatment of sample in particular temperature range. There are various steps in which the weight loss may occur, first step is about 50-80 ^{0}C, step 2 in the range of 200-300 ^{0}C in which weight loss mainly due to evaporation of moisture and water molecule present in LLZO[16]. Then in step 3 at temperature range of 400-450 ^{0}C weight loss due to H_2O and CO_2 release from sample , and after temperature 600 ^{0}C material is stable up to 900 ^{0}C. Similar result is obtained for Fe-doped c-LLZO which shown in figure 3.19. The DTG and DTA results also give the similar reflection of TGA pattern.

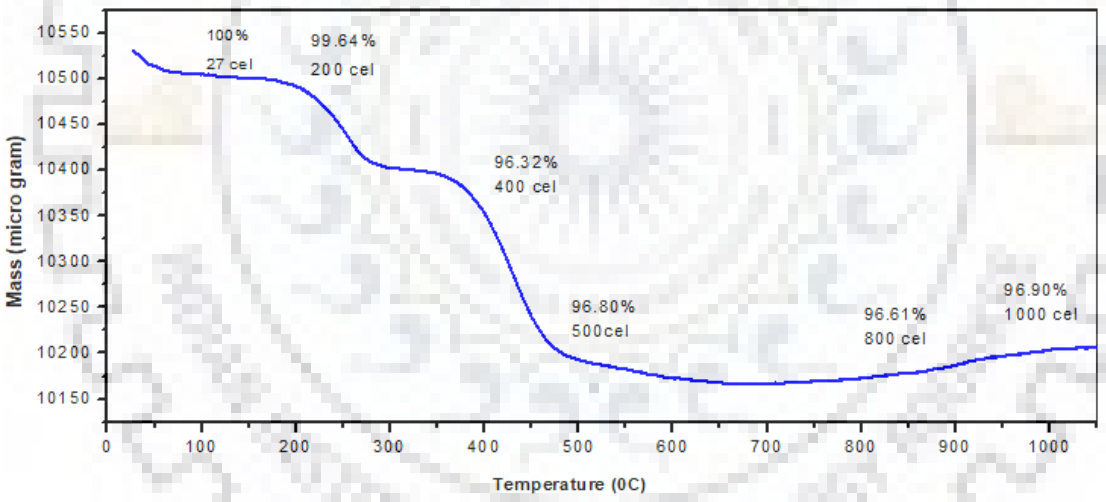

Figure 3.17 TGA image and weight loss of t-LLZO

DTA and DTG of t-LLZO:

DTA fig 3.18 confirms the at the high temperature there is no phase transformation in t-LLZO system. And DTG shows there in no sharp change mass during high temperature.

The chemical reaction at different temperature is described as follows:

At 200-250 ^{0}C

$$Li_{6.86}H_{0.14}La_3Zr_2O_{12}.\ (0.2H_2O) \longrightarrow Li_{6.86}H_{0.14}La_3Zr_2O_{12} + 0.2H_2O$$

At 400-450 ^{0}C

$$Li_{6.86}H_{0.14}La_3Zr_2O_{12} \longrightarrow Li_{6.86}H_{0.14}La_3Zr_2O_{11.93} + 0.07H_2O$$

At 650-700 ^{0}C

$$Li_{6.86}H_{0.14}La_3Zr_2O_{11.93} + Li_2CO_3 \longrightarrow Li_7La_3Zr_2O_{12} + 0.07\ CO_2$$

At 800-950^{0}C

Mass gain possibly will take place due to minor oxidation of substance.

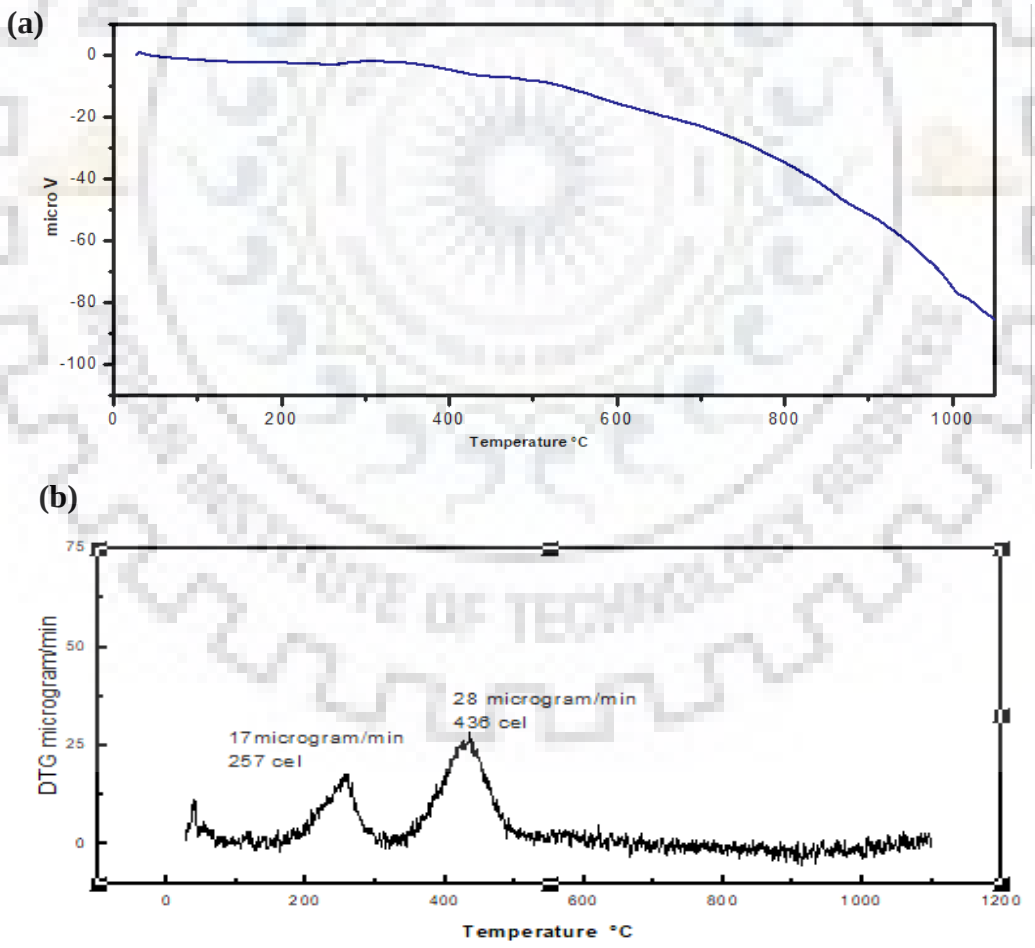

Figure 3.18 (a) DTA and (b) DTG image of t-LLZO

TGA of Fe-doped LLZO:

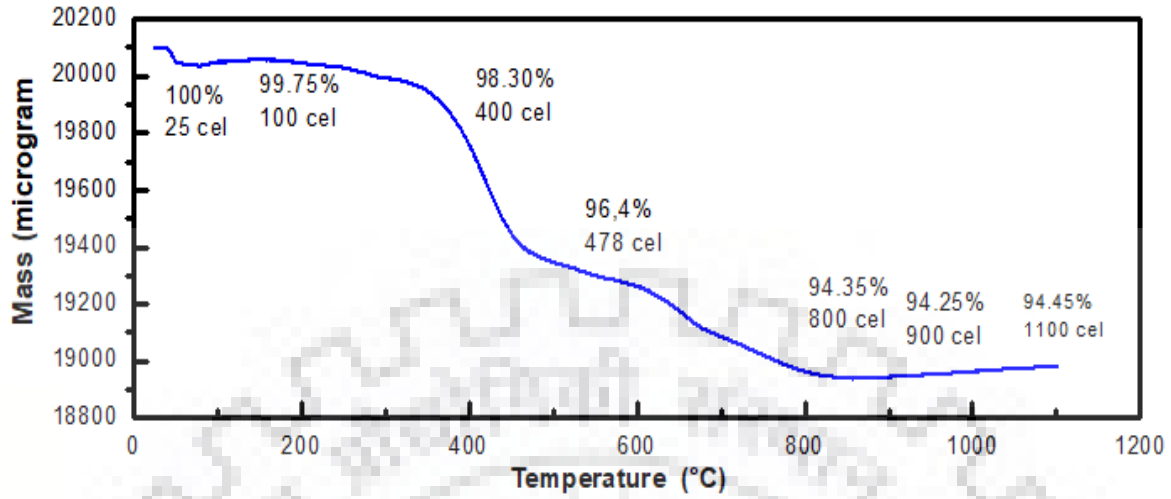

Figure 3.19 TGA of Fe-doped LLZO:

The chemical reaction at different temperature is described as follows:

At 200-250 ^{0}C

$Li_{6.46}H_{0.14}Fe_{0.2}La_3Zr_2O_{12}.(0.2H_2O) \longrightarrow Li_{6.46}H_{0.14}Fe_{0.2}La_3Zr_2O_{12} + 0.2H_2O$

At 400-450 ^{0}C

$Li_{6.46}H_{0.14}Fe_{0.2}La_3Zr_2O_{12} \longrightarrow Li_{6.86}H_{0.14}Fe_{0.2}La_3Zr_2O_{11.93} + 0.07H_2O$

At 650-700 ^{0}C

$Li_{6.46}H_{0.14}Fe_{0.2}La_3Zr_2O_{11.96} + Li_2CO_3 \longrightarrow Li_{6.6}Fe_{0.2}La_3Zr_2O_{12} + 0.07\ CO_2$

900-1000^{0}C

Mass gain may take place due to minor oxidation of sample.

DTA and DSC of Fe-doped LLZO:

Again DTA data of Fe-doped LLZO fig 3.20 confirms the at the high temperature there is no phase transformation in Fe-LLZO system. And DTG shows there in no sharp change mass during high temperature.

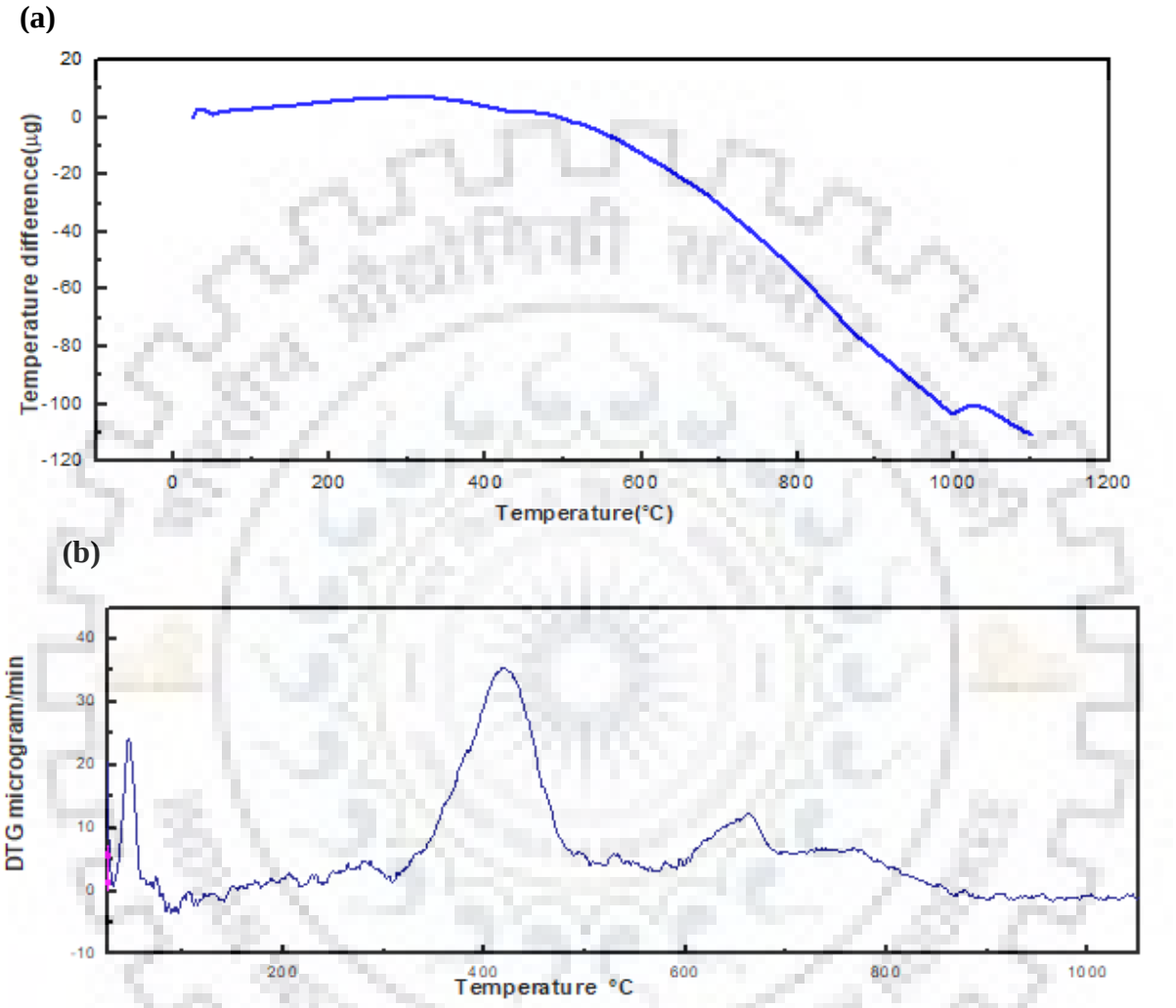

Fig3.20 (a) DTA and (b) DTG of Fe-doped LLZO

3.4.6 Fourier Transform Infrared (FTIR) Spectroscopy:

The sample of LLZO was investigated and characterized by using Fourier transform infrared (FTIR) spectroscopy. The FTIR analysis has been done for both the sample Fe-doped and t-LLZO. For both the system so significant changes is observed, nearly same result is shown by FTIR spectrum which is shown in Figure3.21. The FTIR spectrum shown in fig 3.21indicates the absorbance peak at 3300-3500 cm^{-1} region corresponds to OH^- vibration

which is also having good resemblance with TGA results. The absorbance band in this region is due to the reaction of LLZO with moisture from atmosphere by which substitution of proton with Li-ion take place to form O-H bond and LiOH forms upon further exposure of moisture. The peak obtained in range of 1000-1650 cm^{-1} assigned to absorbance of carbonate from the atmosphere and confirms the presence of Li_2CO_3. The peak indicates at 866.27cm^{-1} attributed to characteristics of Zr-O-Zr vibration[17] and band at 523.56 cm^{-1} may correspond to La-O vibrations.

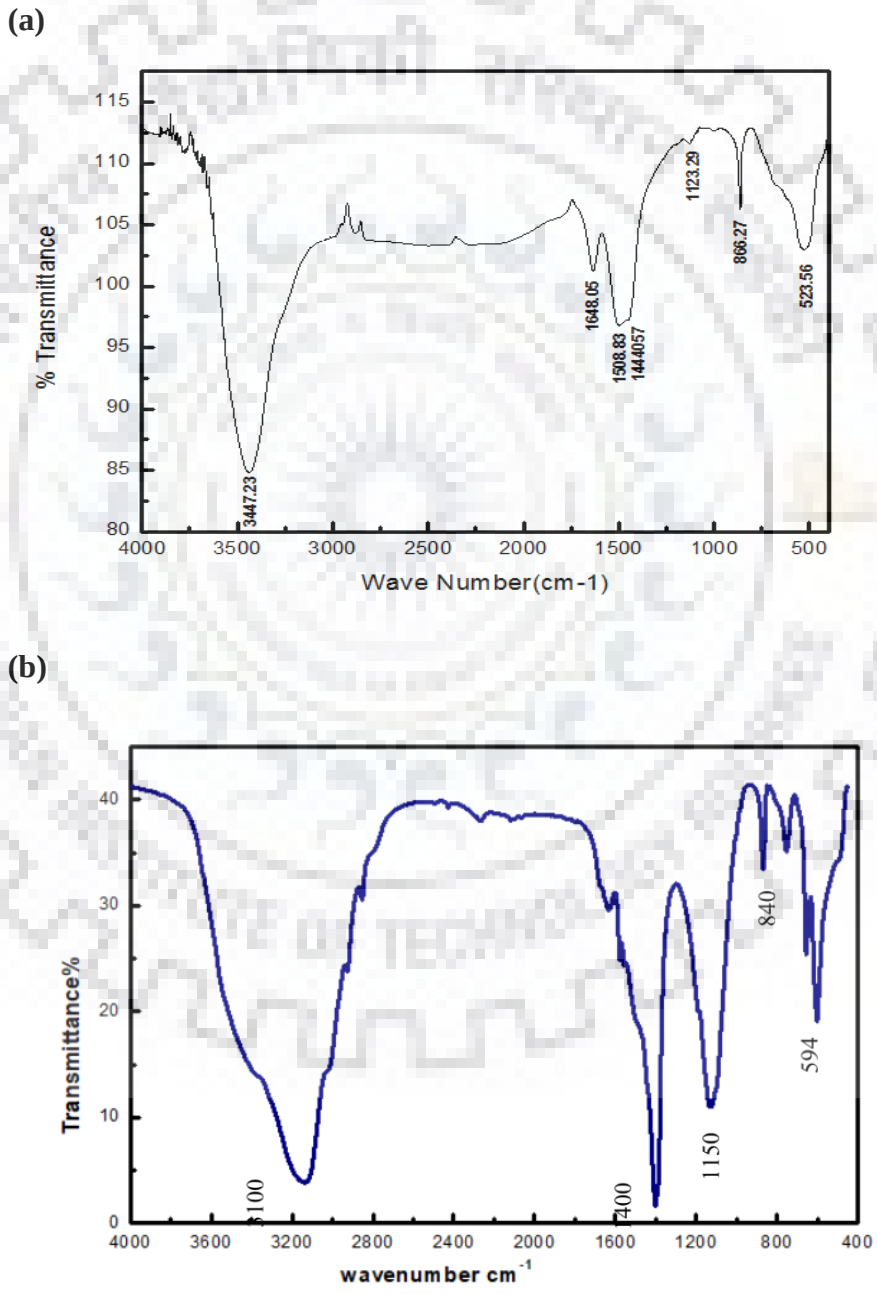

Fig3.21 Absorbance spectra (a) t-LLZO and (b)Fe-doped LLZO

3.5 Magnetic Property (VSM):

On doping participation of ferromagnetic material Fe_2O_3 in LLZO then synthesised Fe-doped LLZO exihibit magnetic property and governed by M-H. curve. Magnetism property is very poor in LLZO does not affects the ionic conduction throgh electrolye.

Further magnetism property in LLZO is the part of next upcoming Li-ion battery.

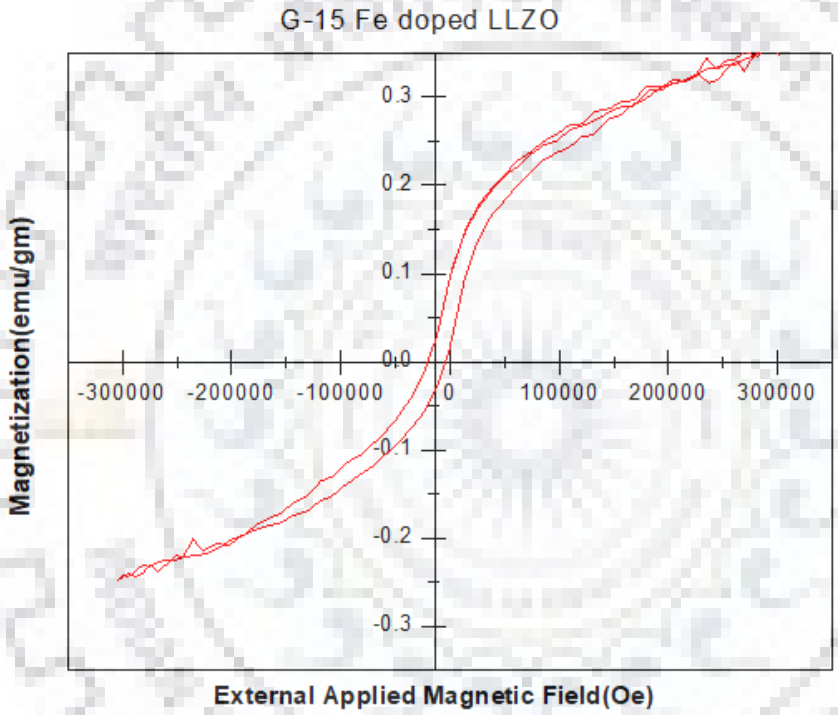

Figure 3.22 M-H loop of Fe-doped LLZO

3.6 Electrical Properties:

3.6.1 Electronic Conductivity Measurement (I-V Measurement):

Electronic conductivity has been done by DC conductivity measurement and the I-V characteristics shown in Figure 3.15. This measurement is done by two probe method in which current vs. voltage profile is recorded. The pellet of t-LLZO of diameter (d) 10.9.57 mm and thickness (t) 1.09 mm and Fe-doped LLZO of diameter (d) 7.9 mm and thickness (t) 1.80 mm is coated by silver on both the flat surfaces and dried at 100 ^{0}C for 1 hour. Then we applied DC potential and measure the value of current. The measured current at various voltages provides

estimation of resistivity or electronic conductivity of solid electrolyte LLZO by using the formula$\sigma_{dc} = \frac{1}{\rho} = \frac{1}{R}\left(\frac{t}{A}\right)$, where $A = \frac{\pi d^2}{4}$ area of flat surface.

The measured electronic conductivity (σ_{dc}) of t-LLZO and Fe-doped c-LLZO is order of 0.209x10^{-7} S/cm and 2.67x10^{-8} S/cm, which shows both system is electronically insulator and have good agreement with reported data.

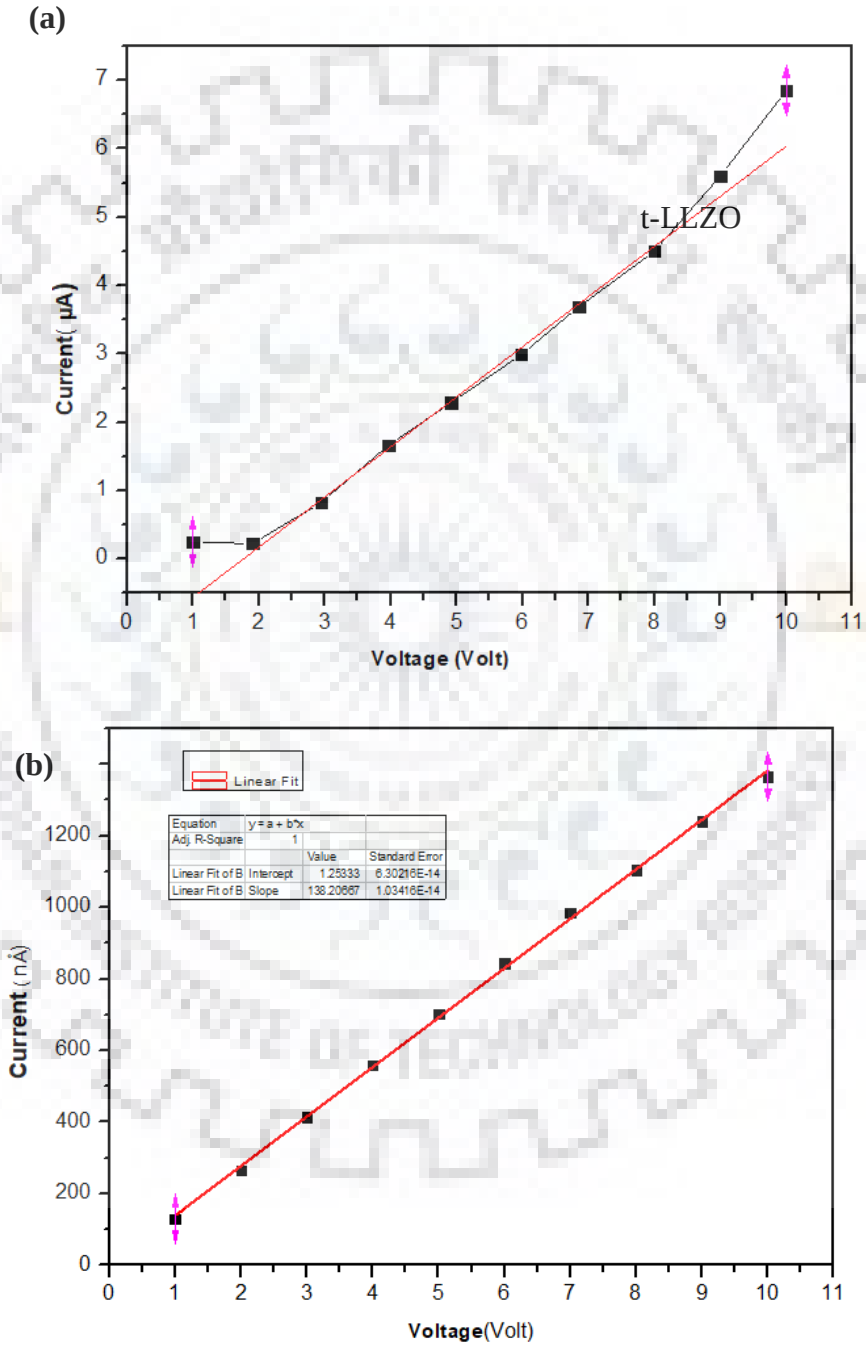

Fig3.23 I-V characteristics of (a) t-LLZO and (b) Fe-LLZO(lower)

3.6.2 AC Impedance Spectroscopy Measurement:

The bulk ionic conductivity and grain boundary resistance of synthesized Fe-doped LLZO were studied by using impedance spectroscopy. The spectra were recorded in range of 1 Hz to 1MHz. A typical Nyquist Impedance pattern of Fe-LLZO is shown in Figure3.25.

The plot is characterized by semicircle in high frequency region, another semicircle in intermediate frequency region and a spike in low frequency range. Further This impedance data can be fitted by using conventional circuit that employs a constant phase element (CPE) in parallel to resistance element (R) to represent a semicircle ([RQ]) and constant phase element to represent the low frequency spike ([Q]).The capacitance (C) may calculated from the equivalent fitting parameter by using formula $C=R^{1-n}Q^{1/n}$, the estimated value of capacitance of high frequency and intermediate frequency semicircle are $6x10^{-11}$ and $1x10^{-8}$ F respectively. The capacitance in intermediate frequency semi-circle is too high because of conventional grain boundary contribution in the system.

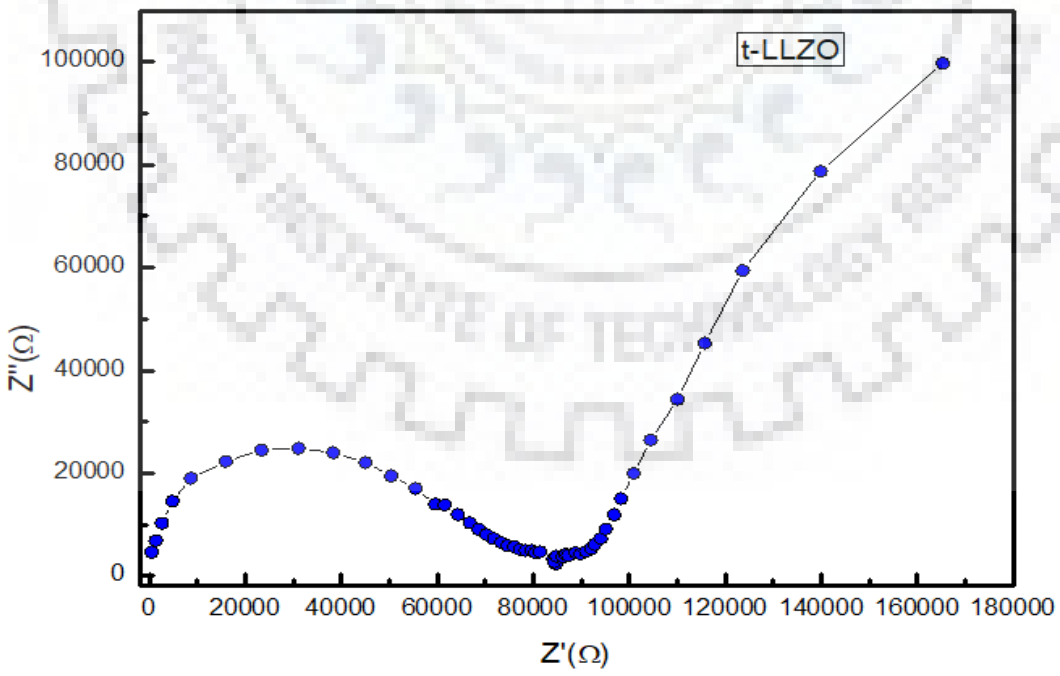

Fig3.24 Nyquist plot of t-LLZO

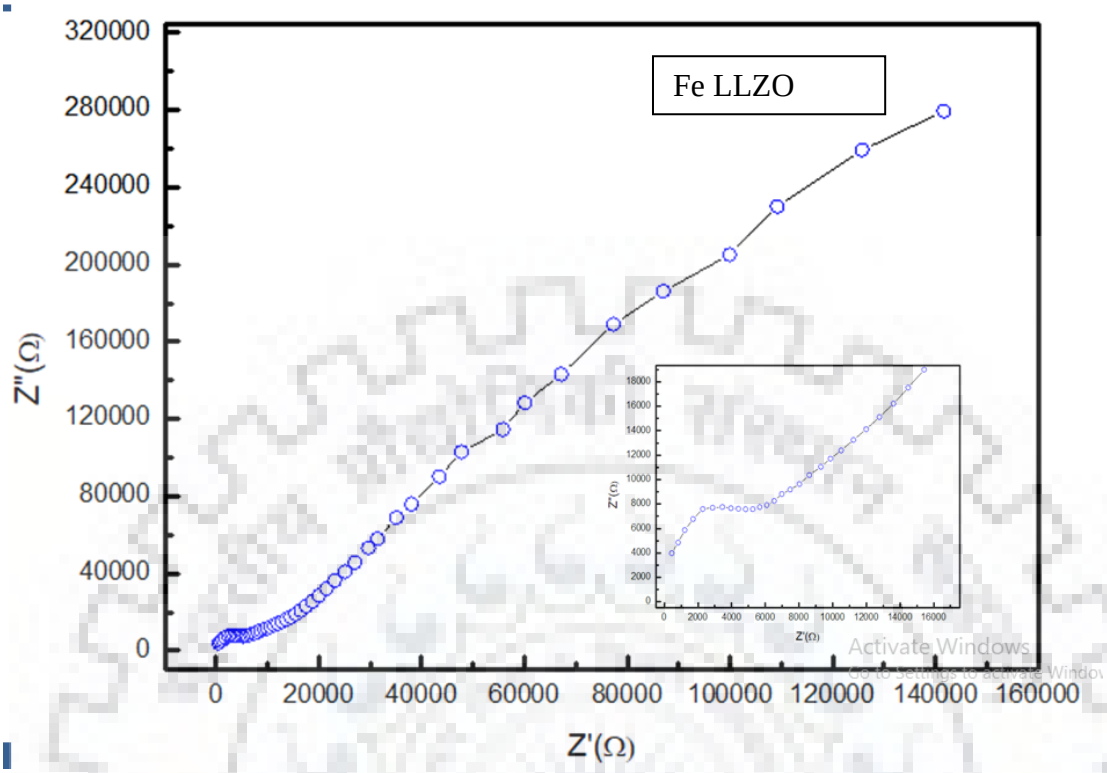

Fig 3.25 Nyquist plot of Fe-LLZO

The high frequency semicircle suggests the resistance of 2600 Ω which has intercept at high frequency side on real Z axis at 1150 Ω and capacitance $6x10^{-11}$ F lies in the range of intermediate frequency region. From these results the bulk resistance is only half of the grain boundary resistance. The observed results suggest that the total conductivity of t-LLZO $0.25\times10\text{-}^{5}$ and Fe-doped LLZO at room bulk conductivity is $0.72x10^{-4}$ S/cm.

CHAPTER 4

SYNERGISTIC MULTI-DOPING EFFECTS ON THE SYNTHESISED $Li_{7-3x-3y}Fe_xAl_yLa_3Zr_2O_{12}$

4.1 Introduction:

In the previous chapter 3, Fe-doped LLZO exhibit more ionic conductivity as compared to bare pure phase of LLZO. So it has been investigated that doping is novel method to enhance the ionic conductivity of LLZO. In Fe-LLZO the role of Fe is making the stabilize the cubic phase and stopping the internal loss of Li-ions through the interstitial sites. Because of Fe was doped at 24d tetrahedral sites in Fe-LLZO. The next investigation has been done for multidoped LLZO. So in this chapter, Al and Fe both are doped on same 24d tetrahedral sites and check the synergetic multi-doping effects. And again experimental methods and characterization techniques like **XRD, TGA/DTA, FESEM, EDX, ICP-OES TEM, VSM, FTIR, I-V** and **EIS** of nanostructured LLZO has been discussed. The conventional Solid state method is preferred due to getting the fruitful results from it like, good thermal stability, morphology and other also cannot be ignored less impure phase as compared to another synthesis methods like sol-gel, combustion etc. The doping is essential part of synthesis to stabilizing of cubic phase at high temperature 1050^oC.

4.2 Experimental Method:

In Solid state method all precursors Li_2CO_3, La_2O_3, ZrO_2 and0.1mole of $Fe_2O_3$and 0.1 mole Al_2O_3 are taken in stoichiometry ratio with 10% excess of Li_2CO_3 to compensate the Li loss during high temperature[18]. These precursors are mixed by ball milling for 15hours. The mixed powder was kept in furnace at 900^oC for 6 hours. Again powder was mixed at room temperature for entirely phase mixing and increase surface area. The prepared powder was pressed at 750M Pascale and this pellet reheated at 1050^oC for 15 hours for densification and sintering. Check the impure phase and then again pellet kept at 1000^oC to remove out undesired phase which are coming due to atmosphere content. This pellet finally crushed and XRD of prepared sample was done.

Experimental are taken in this manner shown in flow chart figure 4.1

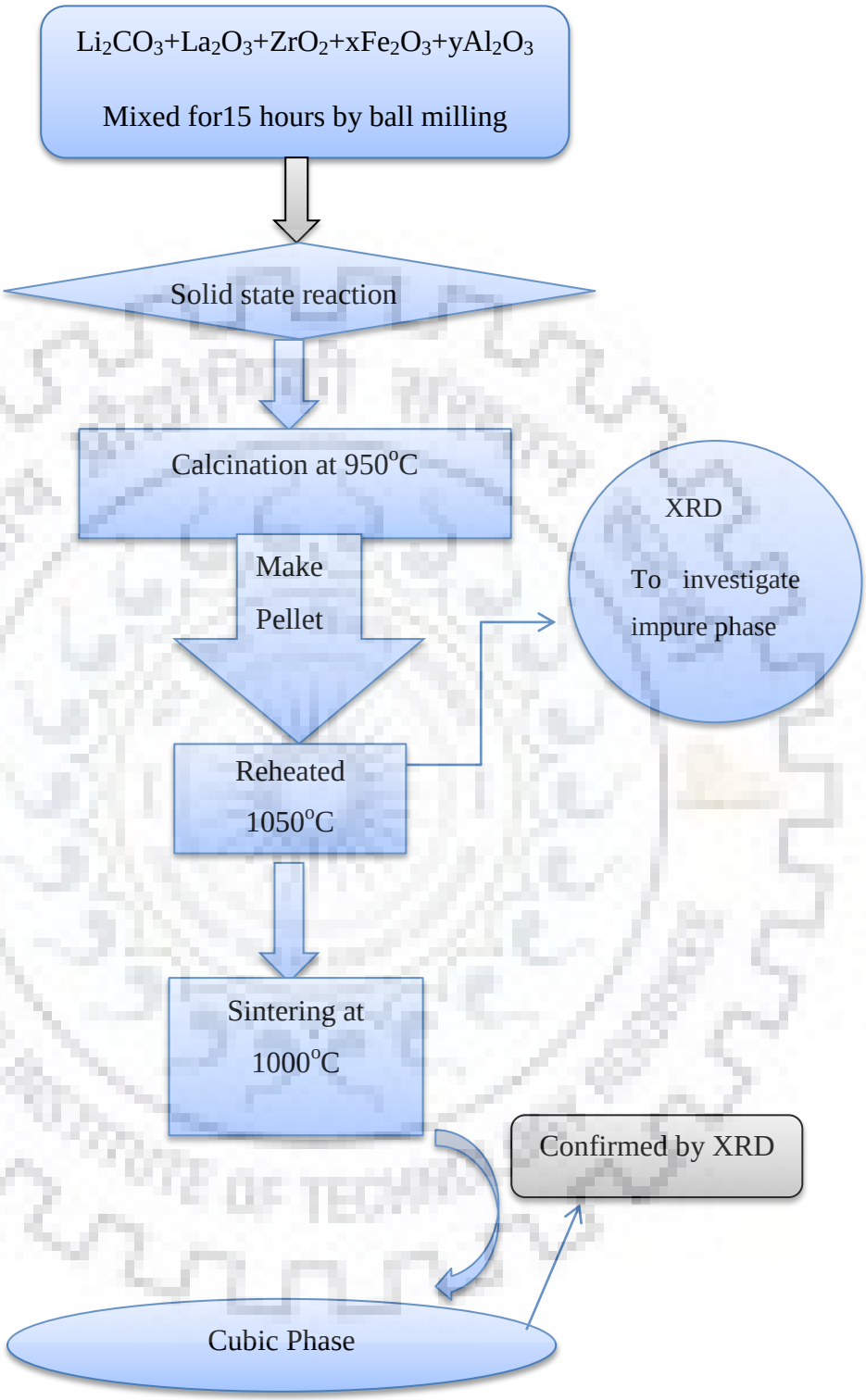

Figure 4.1: Flow chart of synthesis of Fe-Al LLZO

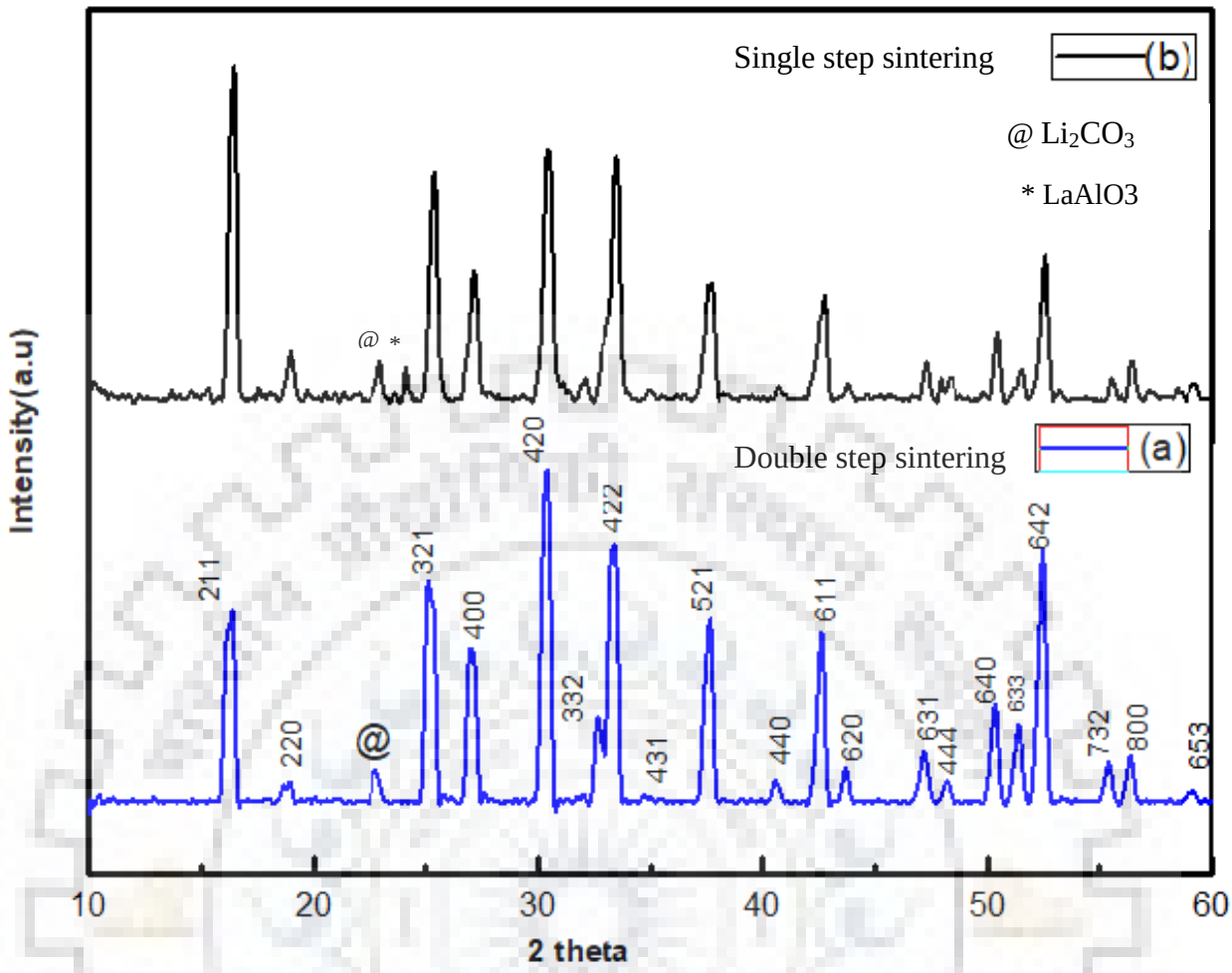

Figure 4.2: X-ray diffraction pattern of Fe-Al LLZO

4.3 Results and Discussion:

4.3.1 X-ray Diffraction (XRD):

The Cubic phase stabilized by doping of Fe at Li sites at temperature 1050 ^{o}C for 26 hours with double heating treatment which confirmed by XRD shown in fig 4.2(a) and single step heating treatment is shown in figure4.2(a). The loss of Li at high temperature and improper phase formation also can be seen from XRD. The tetragonal phase formation without any sintering aid could possible only due to proper step heating treatment in appropriate temperature range and trade of mixing and grinding time during synthesis. In the case of doping of both Fe on and Al on Li sites, the cubic phase formation of LLZO at lower temperature due to Li distribution in Li(1) and Li(2) sites which confirmed by Rietveld

refinement (PDXL-2) having Ia3-d space group. The densification of sample by making pellet is also helpful for formation of less impure phase.

4.3.2 Morphology Analysis:

The morphology of multi-doped LLZO with Fe and Al on same tetrahedral Li sites. Doped c-LLZO is shown in fig 4.3. Here in the homogeneous particle size of order of 20-50 nm which has good agreement with XRD results (Scherer's formula).. The size of particle plays a critical role in material sintering. In general smaller size corresponds to greater incentive for sintering due to higher surface area. At same time reduction in particle size leads to poor necking which create problems to make full densification.

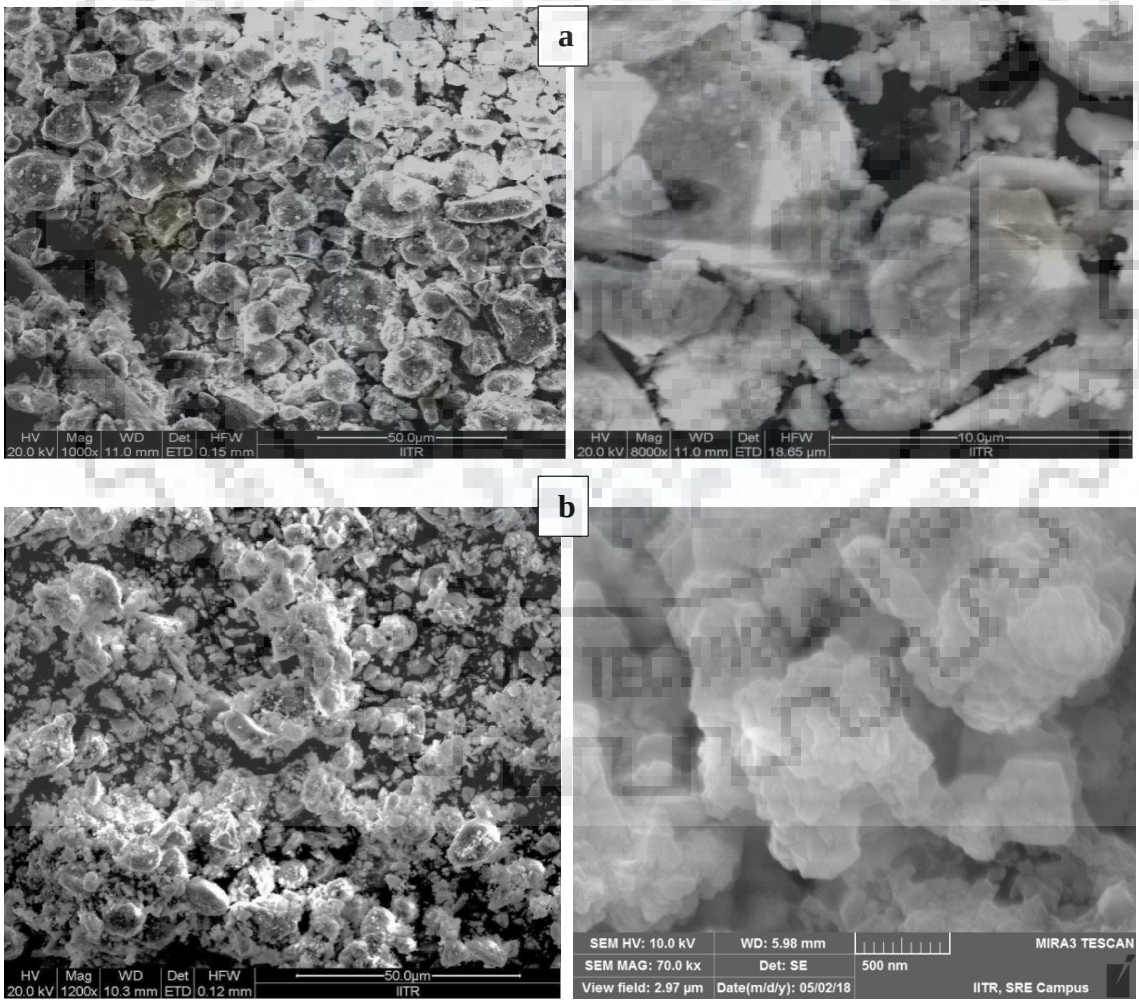

Figure 4.3: FESEM image of Fe-Al LLO (a) at 900^{o}C and (b)1050^{o}C respectively.

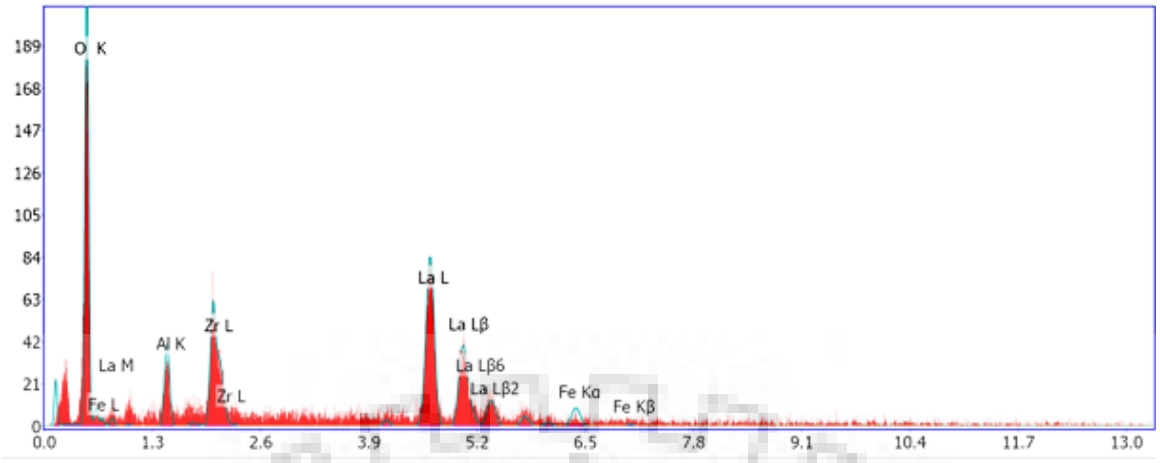

Element	Weight %	Atomic %	Net Int.	Error %
O K	34.01	74.7	80.31	9.43
AlK	5.21	6.78	20.18	11.61
ZrL	12.34	4.75	33.31	6.13
LaL	44.41	11.23	68.93	3.21
FeK	4.03	2.54	8.73	8.25

Figure 4.4 Elemental analysis of Fe-Al-LLZO

4.3.3 Transmission Electron Microscope(TEM):

The TEM results are shown in fig 4.5as below, which have similar conclusion to XRD. The SAED pattern shows good crystallinity of Fe:Al-doped(c-LLZO) system with large grains and as comparison to t-LLZO interplaner separation is order of 6-6.4Å.

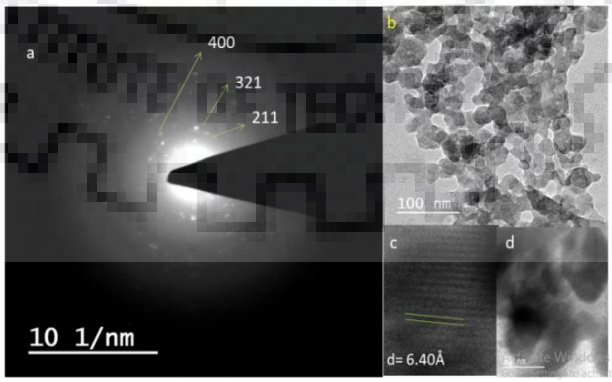

Figure 4.5 TEM image (a) SAED pattern of Fe:Al-LLZO (b,d) high resolution TEM image (c) Interlayer spacing and grains (inset).

4.3.4 Inductively Coupled Plasma-Optical Emission Spectrometry (ICP-OES):

Because Li cannot be detected by EDX spectrum due to its low atomic number (Z=3). When LLZO is synthesized most probably chances remain of Li loss and undesired phase formation through the air atmosphere like Li_2O, $L_{i2}CO_3$ etc.

Li is detected by ICP-OES technique successfully with its concentration in ppb.

ICP-OES of Fe:Al-LLZO is done by following steps is shown as figure 4.6.

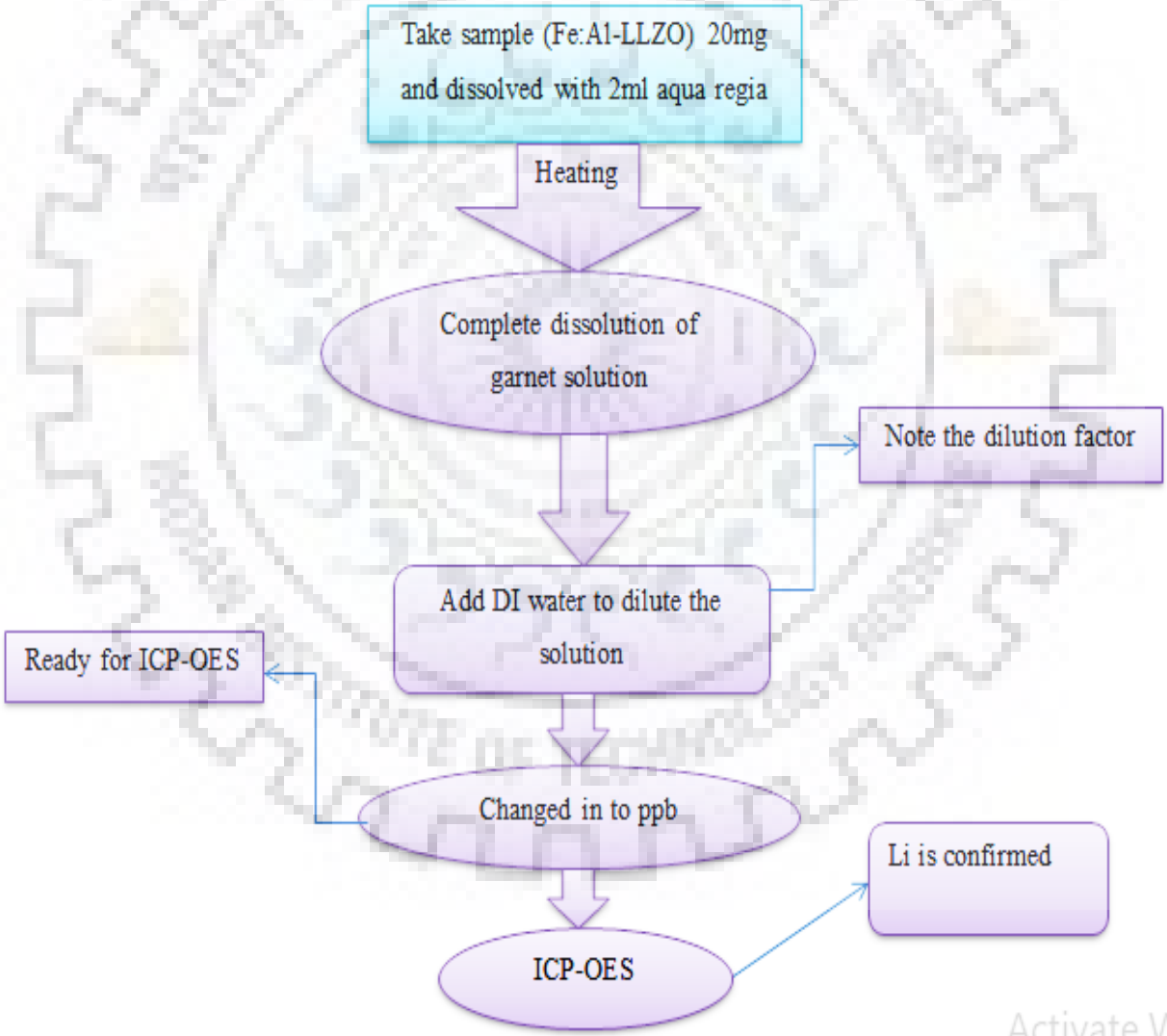

Figure 4.6 Flow chart for ICP-OES process of Fe:Al-doped LLZO

ICP-OES Result is shown as

Analyte	Mass	Conc. Mean (ppb)
Li	7	515.886

ICP-OES result confirmed the Li in multidoped Fe:Al-LLZO. In the previous chapter, Li in Fe-doped LLZO has been also confirmed by ICP-OES, but Fe-LLZO has slightly more Li concentration as comparison to multidoped Fe:Al-LLZO. The reason behind this, Fe-doped LLZO and Fe:Al-LLZO both are synthesised by solid state route but Fe:Al-LLZO is prepared by multistep sintering (2 step) to remove and optimize the impure phase. Due the high temperature 1050^{o}C minor Li loss in the Fe:Al-doped LLZO could be occurred.

4.3.5 Thermal Stability TGA-DTA:

The TGA curves reveals the different steps during formation of LLZO as shown in Figure4.7, which is result of different weight loss during heat treatment of sample in particular temperature range. There are various steps in which the weight loss may occur, first step is about 50-80 ^{0}C, step 2 in the range of 200-300 ^{0}C in which weight loss mainly due to evaporation of moisture and water molecule present in LLZO. Then in step 3 at temperature range of 400-450 ^{0}C weight loss due to H_2O and CO_2 release from sample and after temperature 600 ^{0}C material is stable up to 900^{0}C. Similar result is obtained for Fe-doped c-LLZO which shown in fig 4.7. The DTG and DTA results also give the similar reflection of TGA pattern.

The chemical reaction at different temperature is described as follows:

At 200-250 ^{0}C

$$Li_{6.46}H_{0.14}Fe_{0.1}Al_{0.1}La_3Zr_2O_{12}.(0.2H_2O) \longrightarrow Li_{6.46}H_{0.14}Fe_{0.1}Al_{0.1}La_3Zr_2O_{12} + 0.2H_2O$$

At 400-450 ^{0}C

$$Li_{6.46}H_{0.14}Fe_{0.1}Al_{0.1}La_3Zr_2O_{12} \longrightarrow Li_{6.86}H_{0.14}La_3Zr_2O_{11.93} + 0.07H_2O$$

At 650-700 ^{0}C

$$Li_{6.46}H_{0.14}Fe_{0.1}Al_{0.1}La_3Zr_2O_{11.96} + Li_2CO_3 \longrightarrow Li_7La_3Zr_2O_{12} + 0.07\ CO_2$$

(a)

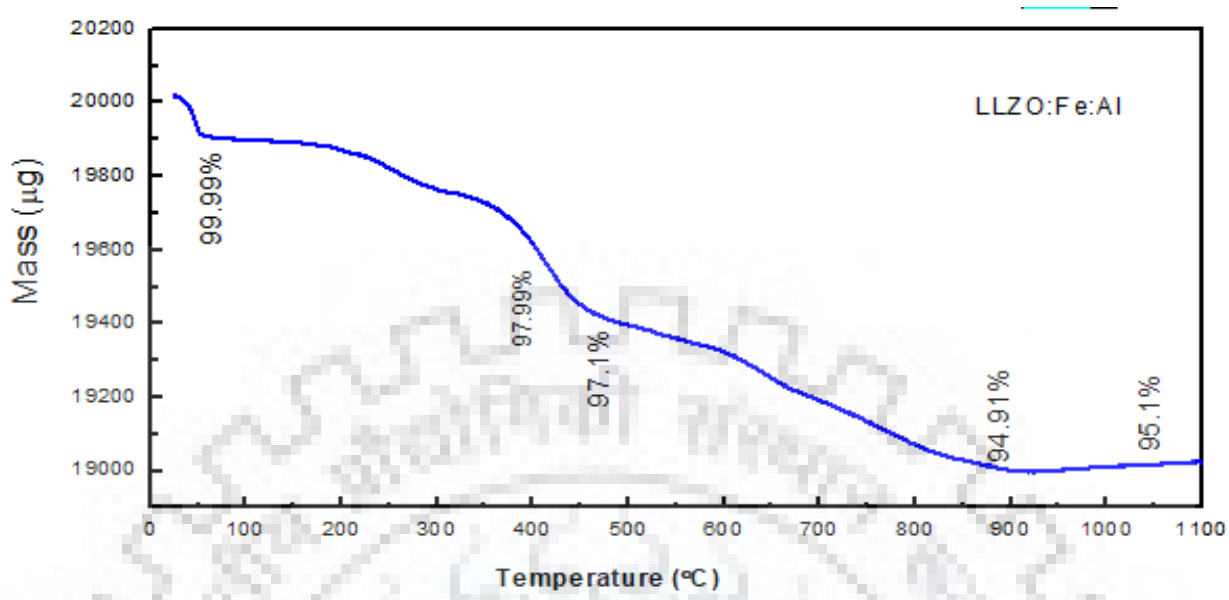

(b)

DTA:

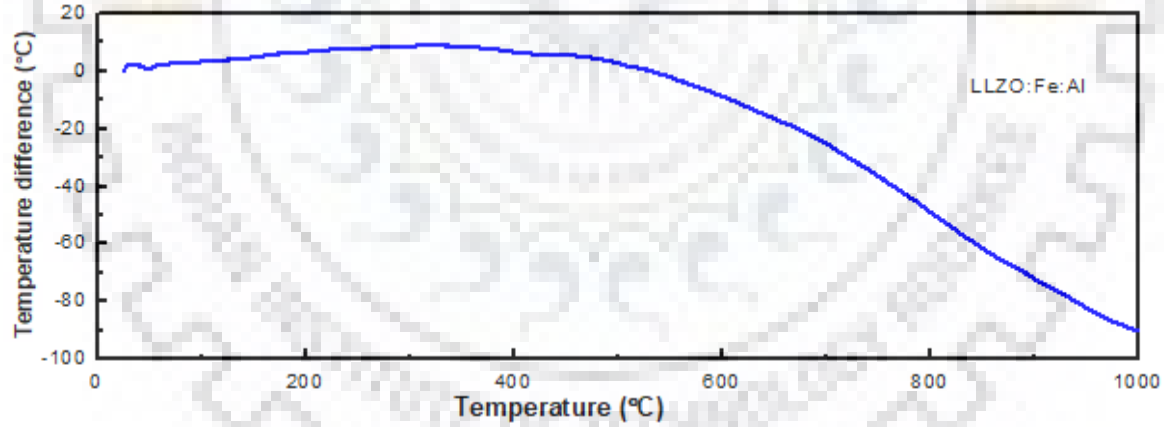

Figure 4.7 (a) TGA and (b) DTA analysis of Fe:Al doped LLZO

4.3.6 Fourier Transform Infrared (FTIR) Spectroscopy:

The sample of LLZO was investigated and characterized by using Fourier transform infrared (FTIR) spectroscopy. The FTIR analysis has been done for multidoped Fe:Al-LLZO. The FTIR spectrum shown in fig 4.8 indicates the absorbance peak at 2800-3200 cm^{-1} region corresponds to OH^- vibration which is also having good resemblance with TGA results. The

absorbance band in this region is due to the reaction of LLZO with moisture from atmosphere by which substitution of proton with Li-ion take place to form O-H bond and LiOH forms upon further exposure of moisture. The peak obtained in range of 1000-1450 cm^{-1} assigned to absorbance of carbonate from the atmosphere and confirms the presence of Li_2CO_3. The peak indicates at 866.27cm^{-1} attributed to characteristics of Zr-O-Zr vibration and band at 523.56 cm^{-1} may correspond to La-O vibrations.

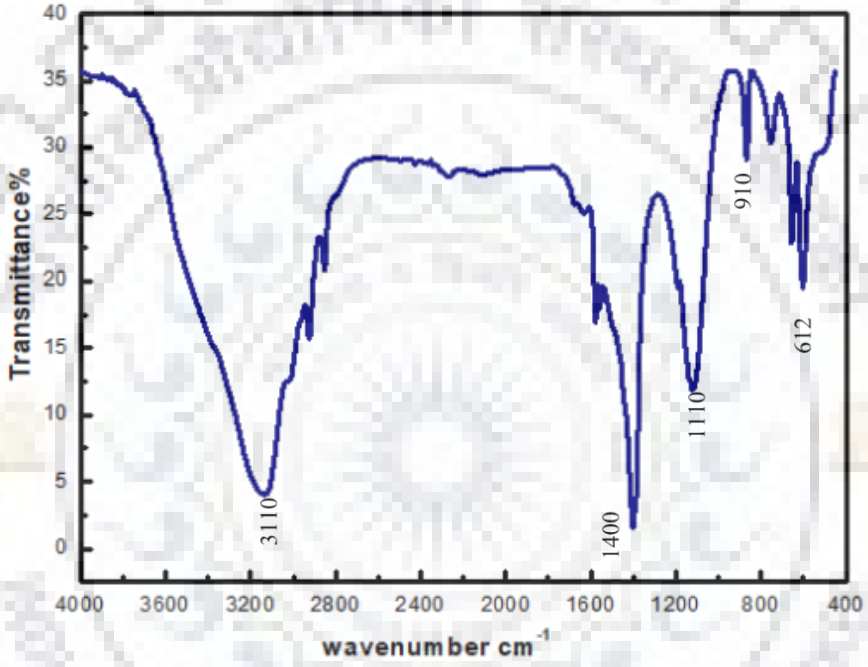

Figure 4.8 FTIR of Fe:Al-LLZO

4.4 Magnetic Property (VSM):

On doping participation of ferromagnetic material Fe_2O_3 in LLZO then synthesised Multi doped LLZO exihibit magnetic property and governed by M-H. curve. But magnetism property is very poor in LLZO does not affects the ionic conduction throgh electrolye.

And further study on magnetism property in LLZO is the part of next upcoming Li-ion battery.

Some organizaions are doing research on magnetism effects in the Li-ion battery. Massachusetts Institute of Technology is one of them.

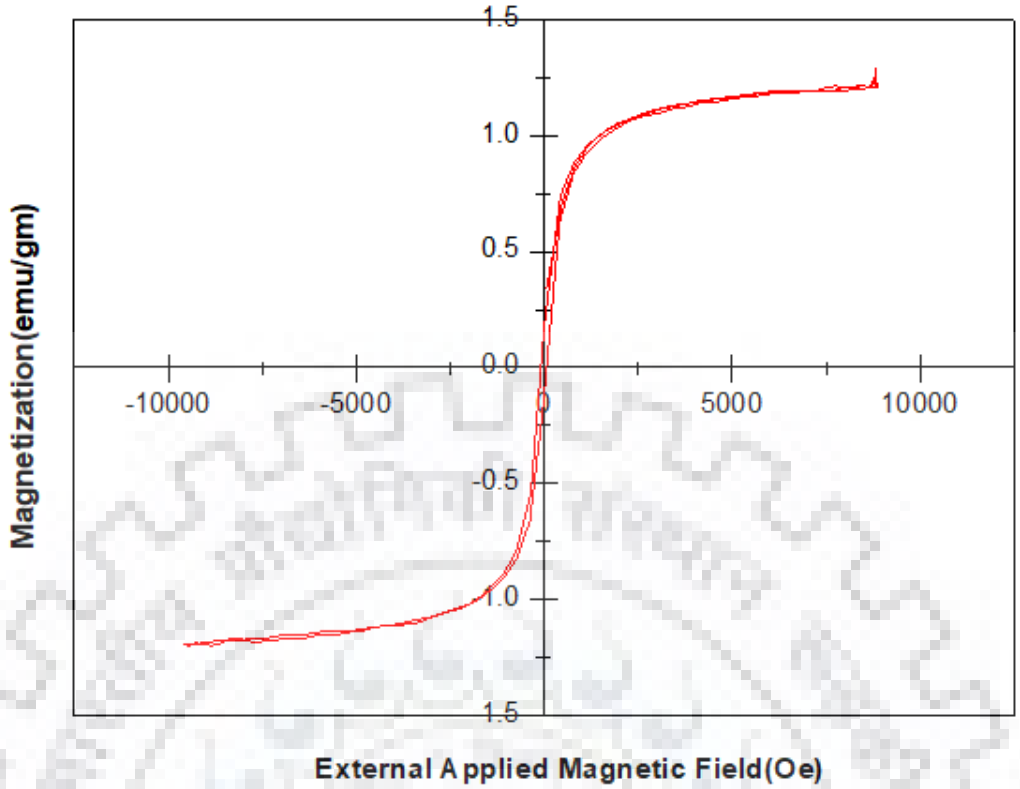

Figure 4.9 M-H loop for Fe:Al doped-LLZO

4.5 Electrical Measurments:

4.5.1 I-V Measurment:

Electronic conductivity has been done by DC conductivity measurement and the I-V characteristics shown in Figure 4.10. This measurement is done by two probe method in which current vs. voltage profile is recorded. The pellet of diameter (d) 9.25 mm and thickness (t) 1.055 mm is coated by silver on both the flat surfaces and dried at 100 ^{0}C for 1 hour. Then we applied DC potential and measure the value of current. The measured current at various voltages provides estimation of resistivity or electronic conductivity of solid electrolyte LLZO by using the formula$\sigma_{dc} = \frac{1}{\rho} = \frac{1}{R}\left(\frac{t}{A}\right)$, where $A = \frac{\pi d^2}{4}$ area of flat surface.

The measured electronic conductivity (σ_{dc}) of t-LLZO and Fe-doped c-LLZO is order of 10^{-7} S/cm, in previous chapter which shows both system is electronically insulator and have good agreement with reported data. Electronic conductivity (σ_{dc}) of Fe:Al doped LLZO is $7.5x10^{-7}$ S/cm,

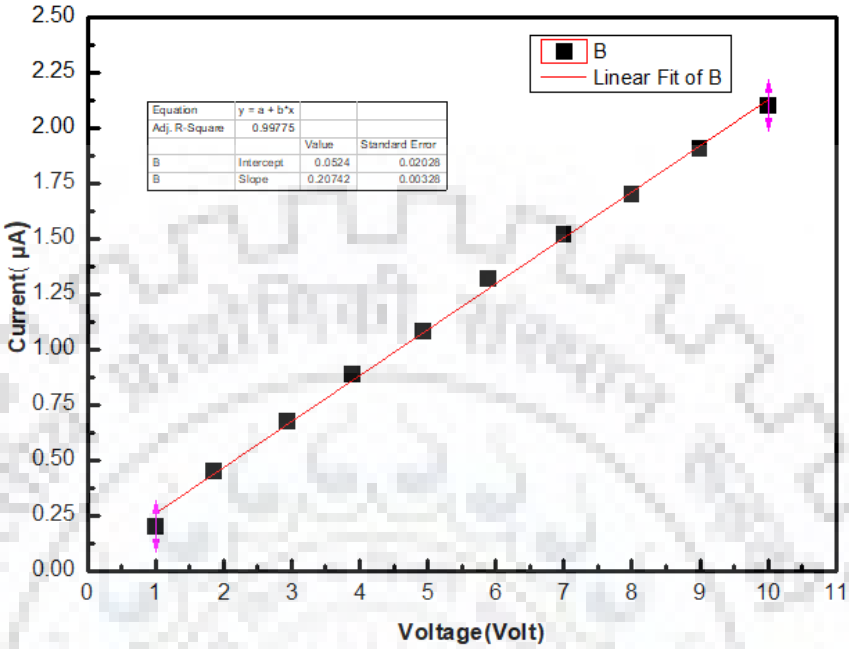

Figure 4.10 I-V characteristics of Fe:Al-doped LLZO

4.5.2 AC Impedance Spectroscopy Measurement:

The Li–ion transport property of synthesized Fe:Al-doped LLZO were studied by using impedance spectroscopy. The spectra were recorded by sintering of pellet at 1050 ^{0}C in order to estimate the impedance of the Fe:Al-LLZO. A typical Nyquist Impedance pattern of Fe:Al-LLZO is shown in Figure. 4.11.

The plot is characterized by semicircle in high frequency region, another semicircle in intermediate frequency region and a spike in low frequency range[15].

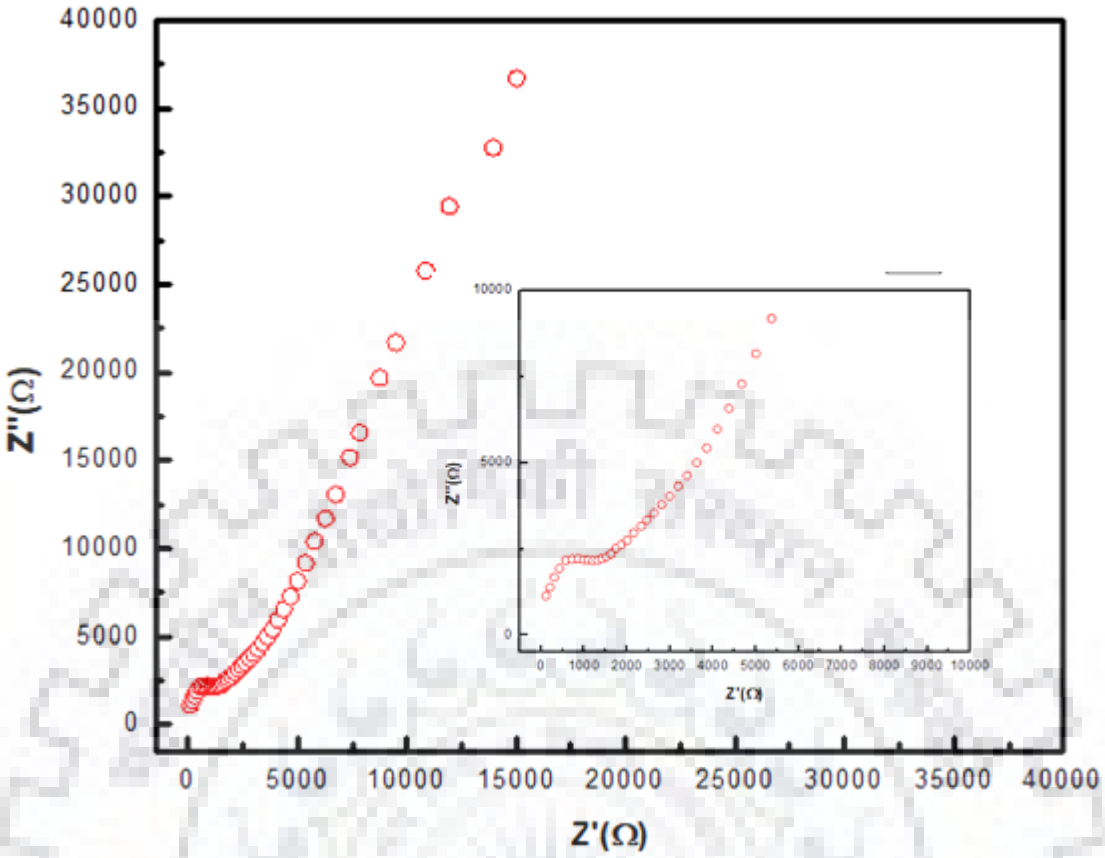

Figure 4.11 Nyquist plot of Fe:Al-LLZO

The total conductivity is found 0.9236×10^{-7} S/cm which is good as compared to Fe-doped LLZO.

CHAPTER 5
CONCLUSION AND FUTURE WORK

5.1 Conclusion on Structural and Transport Property of (Fe-LLZO):

The tetragonal phase of LLZO (bare LLZO) is obtained at lower temperature which is highly crystalline in nature and has particle size in order of 50-100 nm range which is confirmed by both XRD and FESEM. The crystal parameter of t-LLZO is obtained from Rietveld refinement is 12.99Å and 13.02Å. On doping of Fe at Li sites cubic LLZO is formed and lattice parameter decreases up to 12.94Å and particle densification also decreases as compared to t-LLZO. Doping of foreign element Fe and Al changes the sintering temperature up to 100^0C as well as morphology which play an important role to enhance the conductivity and stability of LLZO. Thermal analysis has been done for t-LLZO and Fe-doped LLZO which reveals this system is highly thermodynamically stable. If we compare solid state route and sol-gel then more impure phase is obtained in case of sol-gel method. Hence high temperature solid state synthesis is more prominent for LLZO.

The electronic conductivity of t-LLZO and Fe-doped LLZO at room temperature is order of 10^{-7} to 10^{-8} S/cm which confirms that system is electronically insulator. If we use this system as solid electrolyte in Li-ion battery there is no requirement of separator which prevent electron transfer through it. Since the tetragonal phase have low ionic conductivity due to Li distribution in ordered state while in cubic phase structure partial accommodation and disordered distribution of Li leads to high ionic conductivity. The EIS results have good resemblance with above theoretical prediction, bulk conductivity of t-LLZO is 0.2523×10^{-5} S/cm, and total conductivity of Fe-LLZO is 0.72×10^{-4} S/cm. In Fe-LLZO system, Fe ion takes Li sites and creates more Li vacancies inside the system; hence, the trade of occupied Li sites and vacant sites is mainly cause of enhancement in the conductivity. The effect of multi elemental doping on Li sites (Fe and Al) is also investigated which has similar structural and morphological properties[11]. The ionic conductivity of Fe-Al-LLZO system is 0.9236×10^{-4} S/cm.

Hence, the partial doping on Fe and Al at Li sites helps to stabilize the nanostructured system in cubic phase at lower temperature with high thermal stability and high ionic conductivity which can be used as solid ion conductor for Li-ion battery. My this small but

significant work put one more step forward in direction of enhancement of battery performance which will provide alternate prospective to develop new Solid state electrolyte with promising Li-ion conductivity for all Solid Sate Battery fabrication.

5.2 Proposed Future Work:

There is still much scope to develop the understanding of structure and ion migration mechanism inside the garnet system to achieve the ultimate goal. This system has high contact resistance at electrode interface which is still problematic for this system. What is effect of magnetism and how ionic transportation in magnetic domain is remain untouched for LLZO system. By making the nanofiber[19] and composite with some ionic conducting polymer network we can reach the highest conductivity comparable with liquid electrolyte and decrease the interfacial resistance at electrode. From DFT analysis[20], the Femi energy could be calculated which helps to resolve the problems on the electrode electrolytes interfaces.

Finally, the next phase of garnet oxides research should focus on the engineering at interface and to develop understanding of ion migration in LLZO system, and magnetism effects on Li-ion battery .this approach leads to reach at maturity for all solid Li-ion batteries.

References

[1] X. Luo, J. Wang, M. Dooner, and J. Clarke, "Overview of current development in electrical energy storage technologies and the application potential in power system operation," *Appl. Energy*, vol. 137, pp. 511–536, 2015.

[2] E. M. Erickson *et al.*, "Review — Development of Advanced Rechargeable Batteries : A Continuous Challenge in the Choice of Suitable Electrolyte Solutions," vol. 162, no. 14, pp. 2424–2439, 2015.

[3] N. Nitta, F. Wu, J. T. Lee, and G. Yushin, "Li-ion battery materials : present and future," *Biochem. Pharmacol.*, vol. 18, no. 5, pp. 252–264, 2015.

[4] J. B. Goodenough and K. Park, "The Li-Ion Rechargeable Battery : A Perspective," 2013.

[5] B. Zhang *et al.*, "Mechanisms and properties of ion-transport in inorganic solid electrolytes," *Energy Storage Mater.*, vol. 10, no. August 2017, pp. 139–159, 2018.

[6] J. K. Maranas, "Solid Polymer Electrolytes," 2012.

[7] C. Ma and M. Chi, "Novel Solid Electrolytes for Li-Ion Batteries: A Perspective from Electron Microscopy Studies," vol. 4, no. June, pp. 1–6, 2016.

[8] P. I. J. B. Goodenough, "SOLID ELECTROLYTES FOR NEXT GENERATION BATTERIES," pp. 1–18, 2012.

[9] A. Chagnes and J. Swiatowsk, "Electrolyte and Solid-Electrolyte Interphase Layer in Lithium-Ion Batteries," *Lithium Ion Batter. - New Dev.*, no. Umr 7575, 2012.

[10] S. Ramakumar, C. Deviannapoorani, L. Dhivya, L. S. Shankar, and R. Murugan, "Lithium garnets: Synthesis, structure, Li-ionconductivity, Li-iondynamics and applications," *Prog. Mater. Sci.*, vol. 88, pp. 325–411, 2017.

[11] D. O. Shin *et al.*, "Synergistic multi-doping effects on the Li7La3Zr2O12 solid electrolyte for fast lithium ion conduction," *Sci. Rep.*, vol. 5, pp. 1–9, 2015.

[12] A. Freeman, "Experimental Technique," *Methods*.

[13] L. L. N. O, K. L. L. N. O, V. T. Ã, and W. Weppner, “Effect of sintering on the ionic conductivity of garnet-related structure,” vol. 179, pp. 974–984, 2006.

[14] I. Kokal, M. Somer, P. H. L. Notten, and H. T. Hintzen, “Sol – gel synthesis and lithium ion conductivity of Li 7La 3Zr 2O 12 with garnet-related type structure,” *Solid State Ionics*, vol. 185, no. 1, pp. 42–46, 2015.

[15] E. Yi, W. Wang, J. Kieffer, and R. M. Laine, “Key parameters governing the densification of cubic-Li7La3Zr2O12Li-ionconductors,” *J. Power Sources*, vol. 352, pp. 156–164, 2017.

[16] G. Hongxia, C. Kai, Y. Di, M. Ao, and H. Mian, “Formation Mechanism of Garnet-Like Li 7 La 3 Zr 2 O 12 Powder Prepared by Solid State Reaction,” vol. 45, no. 3, pp. 612–616, 2016.

[17] P. J. Kumar *et al.*, “A novel low-temperature solid-state route for nanostructured cubic garnet Li $_7$ La $_3$ Zr $_2$ O $_{12}$ and its application to Li-ion battery,” *RSC Adv.*, vol. 6, no. 67, pp. 62656–62667, 2016.

[18] Z. Pengcheng *et al.*, “Effect of extra Li content on the property of tetragonal Li 7 La 3 Zr 2 O 12 solid electrolyte prepared by auto-consolidation method,” vol. 126, no. Icmmct, pp. 237–242, 2017.

[19] K. Kelvin *et al.*, “garnet nanofiber networks for lithium batteries,” pp. 1–6, 2016.

[20] Z. Huang, Y. Zhang, M. Kotaki, and S. Ramakrishna, “A review on polymer nanofibers by electrospinning and their applications in nanocomposites,” vol. 63, pp. 2223–2253, 2003.

[20] P. Knauth. Inorganic solid Li-ion conductors: An overview. Solid State Ionics, 180(14–16): 911–916, 2009.

[21]X. Yu, J. Bates, G. Jellison, and F. Hart. A Stable Thin-Film Lithium Electrolyte: Lithium Phosphorus Oxynitride. Journal of The Electrochemical Society, 144(2): 524–532, 1997.

[22] Y. Hamon, A. Douard, F. Sabary, and C. Marcel. Influence of sputtering conditions on ionic conductivity of LiPON thin films. Solid State Ionics, 177(3–4): 257–261, 2006.

[23] A.Levasseur, J. Brethous, J. Reau, P. Hagenmuller, and M. Couzi. Synthesis and characterization of new solid electrolyte conductors of lithium ions. Solid State Ionics, 1(3–4): 177–186, 1980.

[24] Levasseur, J. Brethous, J. Reau, P. Hagen Muller, and M. Couzi. Synthesis and characterization of new solid electrolyte conductors of lithium ions. Solid State Ionics, 1(3–4): 177–186, 1980

[25] Hong HYP. Crystal structure and ionic conductivity of Lil4Zn(GeO4)4 and other new Li-ion superionic conductors. Mater Res Bull 1978;13:117–24.

[26] Murayama M, Kanno R, Irie M, Ito S, Hata T, Sonoyama N, et al. Synthesis of new lithium ionic conductor thio-LISICON-lithium silicon sulphides system. J Solid State Chem 2002;168:140–8.

[27] Bruce PG, West AR. Phase diagram of the LISICON, solid electrolyte system Li4GeO4-Zn2GeO4. Mat Res Bull 1980;15:379–85.

[28] Plattner E, Vollenkle H. Die kristallstruktur der verbindung Li3Zn0.5GeO4. Monat Chem 1979;110:693–8.

[29] Abrahams I, Bruce PG, David WIF, West AR. A re-examination of the lisicon structure using high-resolution powder neutron diffraction: evidence for defect clustering. Acta Crystallogr 1989;B45:457–62.

[30] Saiful Islam M. Recent atomistic modelling studies of energy materials: batteries included. Phil Trans R Soc A 2010;368:3255–67.

[31] Holzwarth NAW, Du YA. Li-ion diffusion mechanisms in the crystalline electrolyte c
[32] Li3PO4 batteries and energy storage. J Electrochem Soc 2007;154:A999–A1004.

[33] H. Aono, E. Sugimoto, Y. Sadaoka, N. Imanaka, and G. Adachi. Ionic Conductivity of Solid Electrolytes Based on Lithium Titanium Phosphate. *Journal of The Electrochemical Society*, 137(4): 1023–1027, 1990.

[34] H. Aono, E. Sugimoto, Y. Sadaoka, N. Imanaka, and G. Adachi. Ionic Conductivity of the Lithium Titanium Phosphate ($Li_{1+X}M_XTi_{2-X}(PO_4)_3$, M = Al , Sc , Y , and La) Systems. *Journal of The Electrochemical Society*, 136(2): 590–591, 1989.